

# **RCA REVIEW**

*a technical journal*

**RADIO AND ELECTRONICS  
RESEARCH • ENGINEERING**

**VOLUME XX**

**SEPTEMBER 1959**

**NO. 3**

RADIO CORPORATION OF AMERICA

DAVID SARNOFF, *Chairman of the Board*

FRANK M. FOLSOM, *Chairman of the Executive Committee*

JOHN L. BURNS, *President*

E. W. ENGSTROM, *Senior Executive Vice-President*

DOUGLAS H. EWING, *Vice-President, Research and Engineering*

JOHN Q. CANNON, *Secretary*

ERNEST B. GORIN, *Vice-President and Treasurer*

---

RCA LABORATORIES

J. HILLIER, *Vice-President*

---

RCA REVIEW

C. C. FOSTER, *Manager*

R. F. CIAFONE, *Administrator*

PRINTED IN U.S.A.

RCA REVIEW, published quarterly in March, June, September, and December by RCA Laboratories, Radio Corporation of America, Princeton, New Jersey. Entered as second class matter July 3, 1950 under the act of March 3, 1879. Second-class postage paid at Princeton, New Jersey, and at additional mailing offices. Subscription price in the United States and Canada; one year \$2.00, two years \$3.50, three years \$4.50; in other countries: one year \$2.40, two years \$4.30, three years \$5.70. Single copies in the United States, \$.75; in other countries, \$.85.

# RCA REVIEW

*a technical journal*

RADIO AND ELECTRONICS  
RESEARCH • ENGINEERING

*Published quarterly by*

RCA LABORATORIES

*in cooperation with all subsidiaries and divisions of*  
RADIO CORPORATION OF AMERICA

---

---

VOLUME XX

SEPTEMBER 1959

NUMBER 3

---

---

## CONTENTS

	PAGE
The Photovoltaic Effect and Its Utilization .....	373
P. RAPPAPORT	
Pattern Synthesis—Simplified Methods of Array Design to Obtain a Desired Directive Pattern .....	398
G. H. BROWN	
Production of Fine Patterns by Evaporation .....	413
S. GRAY AND P. K. WEIMER	
Medium-Power L- and S-Band Electrostatically Focused Traveling- Wave Tubes .....	426
D. J. BLATTNER, F. E. VACCARO, C. L. CUCCIA, AND W. C. JOHNSON	
An Analysis of Parametric Amplification in Periodically Loaded Transmission Lines .....	442
G. H. HEILMEIER	
Transient Cross Modulation in the Detection of Asymmetric-Sideband Signals .....	455
T. MURAKAMI AND R. W. SONNENFELDT	
Voltage Sensitivity of Local Oscillators .....	473
W. Y. PAN	
Determination of Lead-Wire Inductances in Miniature Tubes .....	485
W. A. HARRIS AND R. N. PETERSON	
Spectrum-Selection Automatic Frequency Control for Ultra-Short- Pulse Signaling Systems .....	499
H. KILIN AND R. J. KLENSCH	
RCA TECHNICAL PAPERS .....	518
AUTHORS .....	522

---

© 1959 by Radio Corporation of America  
All rights reserved

---

RCA REVIEW is regularly abstracted and indexed by *Industrial Arts Index*, *Science Abstracts* (I.E.E.-Brit.), *Electronic Engineering Master Index*, *Chemical Abstracts*, *Proc I.R.E.*, and *Electronic & Radio Engineer*.

# RCA REVIEW

## BOARD OF EDITORS

*Chairman*

R. S. HOLMES  
*RCA Laboratories*

E. I. ANDERSON  
*RCA Victor Home Instruments*

A. A. BARCO  
*RCA Laboratories*

G. L. BEERS  
*Radio Corporation of America*

G. H. BROWN  
*Radio Corporation of America*

I. F. BYRNES  
*Industrial Electronic Products*

D. D. COLE  
*RCA Victor Home Instruments*

O. E. DUNLAP, JR.  
*Radio Corporation of America*

E. W. ENGSTROM  
*Radio Corporation of America*

D. H. EWING  
*Radio Corporation of America*

A. N. GOLDSMITH  
*Consulting Engineer, RCA*

A. L. HAMMERSCHMIDT  
*National Broadcasting Company, Inc.*

J. HILLIER  
*RCA Laboratories*

D. D. HOLMES  
*RCA Laboratories*

C. B. JOLLIFFE  
*Defense Electronic Products*

E. A. LAPORT  
*Radio Corporation of America*

H. W. LEVERENZ  
*RCA Laboratories*

G. F. MAEDEL  
*RCA Institutes, Inc.*

H. F. OLSON  
*RCA Laboratories*

R. W. PETER  
*RCA Laboratories*

D. S. RAU  
*RCA Communications, Inc.*

D. F. SCHMIT  
*Radio Corporation of America*

G. R. SHAW  
*Electron Tube Division*

L. A. SHOTLIFF  
*RCA International Division*

S. STERNBERG  
*Astro-Electronic Products Division*

W. M. WEBSTER  
*RCA Laboratories*

I. WOLFF  
*RCA Laboratories*

*Secretary*

C. C. FOSTER  
*RCA Laboratories*

## REPLICATION AND TRANSLATION

Original papers published herein may be referenced or abstracted without further authorization provided proper notation concerning authors and source is included. All rights of republication, including translation into foreign languages, are reserved by RCA Review. Requests for republication and translation privileges should be addressed to *The Manager*.

# THE PHOTOVOLTAIC EFFECT AND ITS UTILIZATION\*†

BY

PAUL RAPPAPORT

RCA Laboratories,  
Princeton, N. J.

*Summary*—The development of the photovoltaic effect from an interesting scientific phenomenon into one of the most efficient methods yet devised for converting solar energy directly into electrical energy is described. Attention is given to considerations of the optimum semiconductor material for solar energy conversion and how it changes with operating temperature. Experimental results are presented which show operating characteristics and conversion efficiencies of a number of materials including silicon, gallium arsenide, indium phosphide, cadmium sulfide, and others. The high-voltage (~100-volt) photovoltaic effect obtained with evaporated CdTe films is described. A discussion of the major problems still to be solved is included.

## INTRODUCTION

THIS PAPER presents a review of the theory and application of the photovoltaic effect with special emphasis on solar energy conversion. A testimonial to the importance of this field today is the Vanguard Earth Satellite which has been sending signals powered by photovoltaic cells back to Earth for a year and a half. As the need for power becomes greater and conventional energy sources such as fossil fuel and fissionable materials are used up, the direct conversion of solar energy striking the waste lands of the world could become an important source of power.

A major step towards the solution of this difficult problem has been achieved by the solar converter or photovoltaic cell. These devices are sometimes called solar batteries, but the term battery is incorrect, strictly speaking, since the primary energy source is not self-contained. Cells have already been made that can convert the sun's radiated energy directly into electrical energy with an efficiency of up to 14 per cent, the best experimental over-all efficiency reported to date<sup>1</sup> for any artificial conversion method.

---

\* Much of the work discussed in this paper was supported by the United States Army Signal Research and Development Laboratories.

† Manuscript received July 13, 1959.

<sup>1</sup> M. B. Prince and M. Wolf, "New Developments in Silicon Photovoltaic Devices." *Jour. Bri. I.R.E.*, Vol. 18, p. 583, October, 1958.

## HISTORY

It has been over 100 years since Becquerel in 1839 first discovered that a photovoltage was developed when light was directed on to one of the electrodes in an electrolyte solution.<sup>2</sup> Adams and Day<sup>3</sup> were the first to observe the effect in a solid (selenium) about forty years later. A number of other early solid-state workers including Lange,<sup>4</sup> Grondahl,<sup>5</sup> and Schottky<sup>6</sup> did pioneering work on selenium and cuprous-oxide photovoltaic cells. This work eventually resulted in the photoelectric exposure meter that has become so important in photography. It was not until 1954, however, that papers describing work directed towards energy sources utilizing the photovoltaic effect appeared in the literature. In that year, an RCA group<sup>7</sup> demonstrated that practical efficiencies could be achieved in converting radioactive radiation into electrical energy using a silicon p-n junction photovoltaic cell. Using a similar method, Chapin, Fuller, and Pearson<sup>8</sup> reported a solar-conversion efficiency of about 6 per cent. A third paper appeared in 1954 by Reynolds, Leies, Antes, and Marburger<sup>9</sup> who reported about 6 per cent solar-conversion efficiency in cadmium sulfide p-n junctions. Since 1954, work on silicon and CdS has been pursued with vigor; other important materials and techniques have also been developed.

## DESCRIPTION OF THE PHOTOVOLTAIC EFFECT

The photovoltaic effect can be defined as the generation of a potential when radiation ionizes the region in or near the built-in potential barrier of a semiconductor. It is characterized by a self-generated emf

<sup>2</sup> E. Becquerel, "On Electric Effects Under the Influence of Solar Radiation," *Compt. Rend.*, Vol. 9, p. 561, 1839.

<sup>3</sup> W. G. Adams and R. E. Day, "The Action of Light on Selenium," *Proc. Roy. Soc.*, Vol. A25, p. 113, 1877.

<sup>4</sup> B. Lange, "New Photoelectric Cell," *Zeit. Phys.*, Vol. 31, p. 139, February, 1930.

<sup>5</sup> L. O. Grondahl, "The Copper-Cuprous-Oxide Rectifier and Photoelectric Cell," *Rev. Mod. Phys.*, Vol. 5, p. 141, April, 1933.

<sup>6</sup> W. Schottky, "Cuprous Oxide Photoelectric Cells," *Zeit. Phys.*, Vol. 31, p. 913, November, 1930.

<sup>7</sup> P. Rappaport, "The Electron-Voltaic Effect in p-n Junctions Induced by Beta-Particle Bombardment," *Phys. Rev.*, Vol. 93, p. 246, January, 1954; P. Rappaport, J. J. Loferski, and E. G. Linder, "The Electron-Voltaic Effect in Germanium and Silicon p-n Junctions," *RCA Review*, Vol. XVII, p. 100, March, 1956.

<sup>8</sup> D. M. Chapin, C. S. Fuller, and G. L. Pearson, "A New Silicon p-n Junction Photocell for Converting Solar Radiation into Electrical Power," *Jour. Appl. Phys.*, Vol. 25, p. 676, May, 1954. See also M. B. Prince, "Silicon Solar Energy Converters," *Jour. Appl. Phys.*, p. 534, Vol. 26, 1955.

<sup>9</sup> D. C. Reynolds, G. Leies, L. L. Antes, and R. E. Marburger, "Photovoltaic Effect in Cadmium Sulfide," *Phys. Rev.*, Vol. 96, p. 533, October, 1954.

and the ability to deliver power to a load, the primary power coming from the ionizing radiation. A potential barrier can be formed in a semiconductor by several means. The two techniques of most interest in photovoltaic cells are (1) the metal-semiconductor barrier formed by deposition of a suitable transparent metallic film by evaporation or sputtering onto a semiconductor as in the selenium cell and (2) the p-n junction formed by introduction of a suitable type impurity into the opposite impurity type semiconductor.

The photovoltaic potential developed when light strikes a semiconductor p-n junction can be explained with the help of Figure 1. The left side of Figure 1 shows how carriers are generated when light photons enter a semiconductor crystal. The circles represent atoms in this two-dimensional crystal lattice and the double lines represent the two electrons in the covalent bonds, as in the case of silicon. Photons

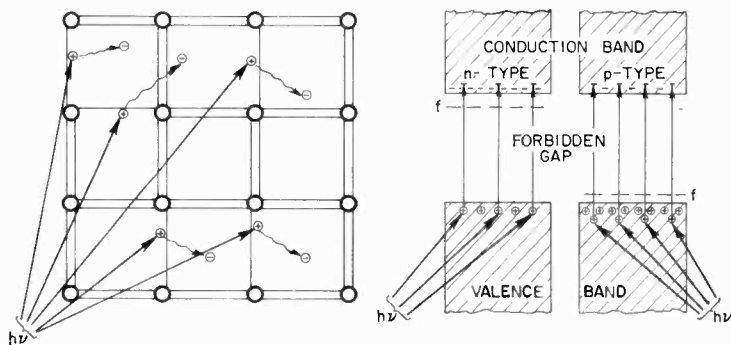
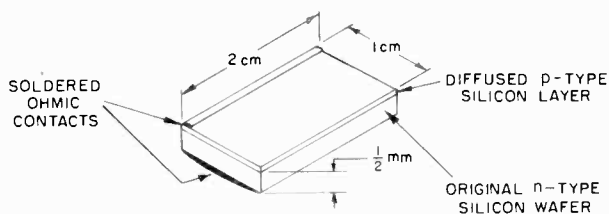


Fig. 1—Electron-hole production by photons.

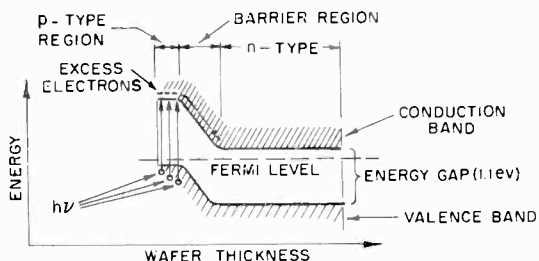
with energy above that required to break these bonds (1.1 eV for silicon) will create electron-hole pairs on a unit quantum efficiency basis as shown on the diagram. The right side of the figure shows the same process using the energy-band model for a semiconductor. Both an n- and p-type semiconductor are shown. In one case, a column V element contributes extra electrons, and in the other case a column III element *does not* contribute enough electrons, and so contributes holes.

The Fermi level (denoted by  $f$  in Figure 1) of the n-type material is near the top of the forbidden gap with many electrons,  $n$ , in the conduction band and few holes,  $p$ , in the valence band. The opposite is true in the p-type material. At a given temperature, the product  $np$  is a constant ( $np \sim 10^{21}$  for silicon at room temperature). For n-type highly conducting silicon,  $n$  can be  $10^{17}/\text{cm}^3$  and  $p$  would there-

fore be  $10^{17}/\text{cm}^3$ . Thus, the concept of majority and minority carriers (electrons and holes, respectively, in the cited case) is developed. When sunlight strikes this semiconductor, those photons having energy greater than the forbidden gap energy produce both type carriers in equal numbers. The net effect is that an intense light source can increase the minority-carrier density by many orders of magnitude while the effect on majority-carrier density is negligible. These photo-induced carriers are in excess of the thermal equilibrium number and they will diffuse randomly about the semiconductor and recombine in times of the order of tenths of microseconds.



(a) SILICON SOLAR CELL



(b) ENERGY LEVEL DIAGRAM OF CELL

Fig. 2—(a) Silicon solar cell; (b) Energy-level diagram of cell.

If the n- and p-type semiconductors are brought together, a p-n junction having a potential barrier is formed, because thermodynamics requires that the average energy of the carriers (the Fermi level) be the same in the two materials. Now, excess carriers that are within a diffusion length (the average distance minority carriers diffuse before they recombine) of the potential barrier will be "trapped" by the barrier and caused to flow across it in an attempt to reduce their energy. This is shown by the energy-level diagram of a p-n junction at the bottom of Figure 2. The excess electrons flow to the right and excess holes to the left. This flow constitutes an electric current, and when suitable electrical connections are made such a device converts

radiation into electricity. The current produced is proportional to the number of photons absorbed, and the voltage depends on the height of the barrier, which is always less than the width of the energy gap in the semiconductor depending on how heavily the p and n regions are doped.

A typical commercially available silicon solar cell is shown at the top of Figure 2. Boron is diffused into an n-type wafer at about 1100°C for 20 minutes, causing a p-type skin a few microns thick to form on all exposed surfaces. All surfaces are etched or lapped down to the n region except the top face. Ohmic contact is made to the top and bottom by first nickel plating the surface and then soldering. Leads are connected to the load from the ohmic contacts, and when light strikes the top face a current is delivered to the load.

To achieve high conversion efficiency it is desirable to produce an electron-hole pair within a diffusion length of the junction for each photon absorbed. For short-diffusion-length material (which is the usual case after the high-temperature firing required to form the p-n junction) it is, therefore, desirable to absorb most of the photons in the region where the field exists. To some extent, the field can be tailored to match the absorption of the light by varying the time and temperature of the boron diffusion process; because of the variation of absorption coefficient with  $\lambda$ , however, a compromise must be accepted. Figure 3 shows how the generation of carriers varies with wavelength within the cell. The shorter wavelengths create carriers in the p region, and the longer wavelengths create carriers in the n region. Since quite a large number of carriers are created in the n region, the diffusion length must be between  $10^{-3}$  and  $10^{-2}$  centimeter for good efficiency.

#### ELECTRICAL CHARACTERISTICS

The electrical characteristic of a photovoltaic cell can be understood from Figure 4. The simplified equivalent circuit consists of a constant-current generator, a nonlinear junction impedance, and a load. The shunting capacitance and resistance and the series resistance are neglected. Light causes a current,  $I$ , to flow in the load; the magnitude of this current is the difference between the generated short-circuit current,  $I_0$ , and the current flowing in the nonlinear junction,  $I_j$ ,

$I_j$ , the usual junction current, is given by

$$I_j = I_0 (e^{\lambda V} - 1), \quad (1)$$

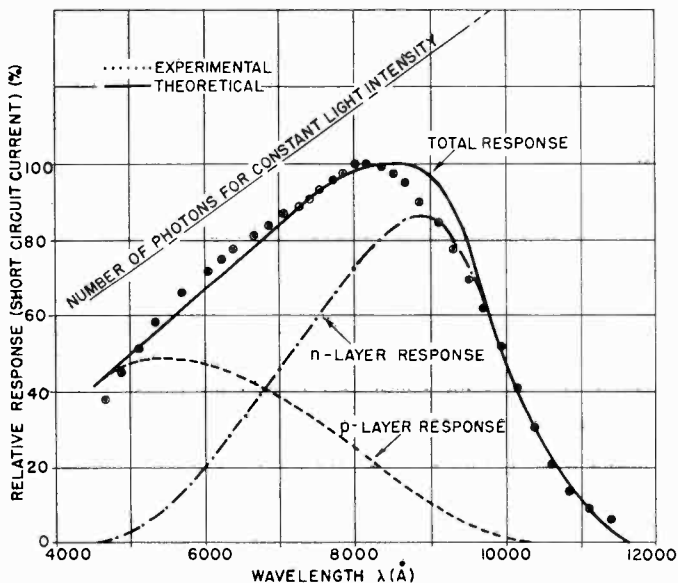


Fig. 3—Carrier creation within a solar cell.  
(Figure supplied by M. B. Prince from Reference (1)).

where  $I_0$  is the dark or reverse saturation current,<sup>10</sup>  $V$  is the voltage applied to the junction, and  $\lambda \equiv e/kT$ ,  $k$  being the Boltzmann constant and  $T$  the absolute temperature. Since

$$I_j + I = I_s, \quad (2)$$

$$I = I_s - I_0 (e^{\lambda V} - 1). \quad (3)$$

The maximum voltage,  $V_{\max}$ , occurs when  $I = 0$ . From Equation (3), therefore,

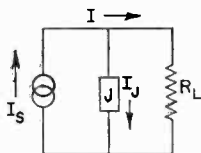


Fig. 4—Simplified equivalent circuit of illuminated cell.

<sup>10</sup> W. Shockley, *Electrons and Holes in Semiconductors*, D. Van Nostrand Co., Princeton, N. J., 1950, p. 314.

$$V_{\max} = \frac{1}{\lambda} \ln \left( \frac{I_s}{I_0} + 1 \right). \quad (4)$$

Figure 5 shows how the current-voltage characteristic of a solar cell develops. The dark-current characteristic is given by Equation (1). The lower curve shows the performance when the cell is exposed to light; this curve is given by Equation (3). Note that  $I_s$  can be many times the dark-junction reverse current. The portion of the curve in the fourth quadrant is the region of power generation. The maximum power delivered,  $P_{\max}$ , is represented by the largest rectangle that can be fitted into this area. Therefore, the squarer the current-voltage characteristic, the higher the efficiency. Under conditions of maximum output, a photovoltaic generator can deliver almost 90 per cent of the generated power to a load, whereas in normal type batteries, only 50 per cent of the generated power reaches the load. This was first

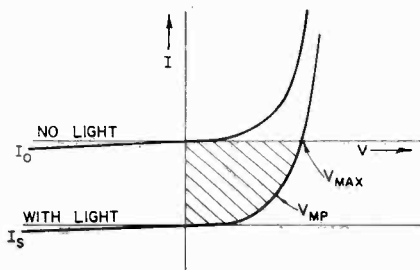


Fig. 5—Effect of light on current-voltage junction characteristic.

pointed out by Lehocve in 1948.<sup>11</sup> It is interesting to note that in a photovoltaic junction, the current flows in the reverse direction and the voltage is in the forward direction. Under conditions of low light level where  $I_s/I_0 < 10$ , or where the series resistance becomes appreciable, the current-voltage characteristic can become linear. Examples of this are given later.

Figure 6 shows how the voltage and current vary as functions of the flux density in silicon cells. The current is directly proportional to the flux, while the voltage is proportional to the log of the flux according to Equation (4). The voltage characteristic shows a saturation value at high flux densities, which is quite convenient for charging storage batteries. Since the voltage is insensitive to the light level, charging can be maintained even though the light fluctuates considerably.

<sup>11</sup> K. Lehocve, "The Photo-Voltaic Effect," *Phys. Rev.*, Vol. 74, p. 463, August, 1948.

## THEORETICAL CONSIDERATIONS

The expression for the maximum solar conversion efficiency of a solar photovoltaic cell is<sup>12</sup>

$$\eta_{\max} = K \left( \frac{\lambda V_{mp}}{1 + \lambda V_{mp}} \right) \frac{n_{ph}(E_G) V_{mp}}{N_{ph} E_{av}}, \quad (5)$$

where  $K$  is a constant depending on the reflection and transmission coefficients and the collection efficiency,  $V_{mp}$  is the voltage delivered at maximum power,  $n_{ph}(E_G)$  is the number of photons that generate electron-hole pairs in the semiconductor of energy gap  $E_G$ , and  $N_{ph} E_{av}$  is the input power where  $N_{ph}$  is the number of incident photons and  $E_{av}$  is their average energy in electron volts.

A number of interesting facts can be obtained from Equation (5).

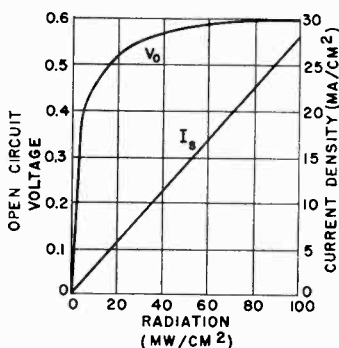


Fig. 6— $V_{\max}$  and  $I_s$  as a function of light intensity.

Since  $\lambda V_{mp}$  is usually much greater than unity, and  $K \sim 1$ , the Equation can be written,

$$\eta_{\max} \approx \frac{n_{ph}(E_G) V_{mp}}{N_{ph} E_{av}}. \quad (6)$$

An estimate of the maximum theoretical efficiency for silicon can be obtained directly, since  $n_{ph}$  is about  $\frac{2}{3} N_{ph}$  and  $V_{mp}$  is about  $\frac{1}{3} E_{av}$  yielding about 22 per cent. Where monochromatic light is used with energy equal to the band gap, the efficiency can be well over 75 per cent, since then  $n_{ph} = N_{ph}$  and  $V_{mp} \sim .75 E_{av}$ . Also, since  $V_{mp} \propto V_{\max} \propto \ln I_s$ ,

$$\eta_{\max} \propto \ln I_s. \quad (7)$$

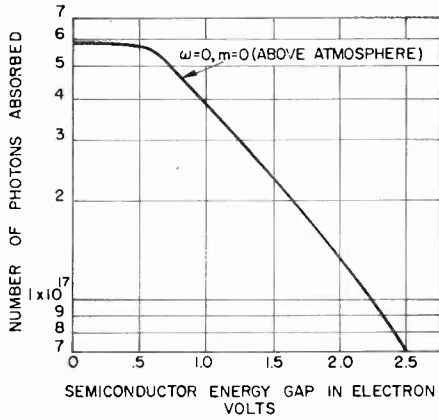


Fig. 7—Absorption of solar photons as a function of energy gap.

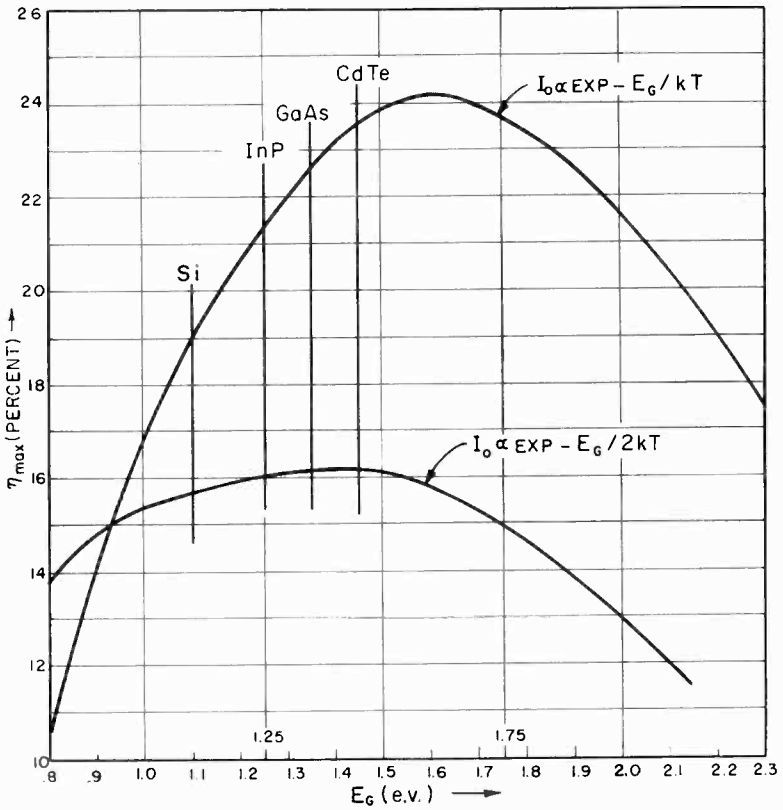


Fig. 8—Theoretical efficiency versus semiconductor band gap.

Therefore, the maximum efficiency should increase at higher light intensities.

Equation (6) also shows how  $\eta_{\max}$  changes as the semiconductor energy gap is varied. Two effects take place. First, the number of photons absorbed,  $n_{ph}(E_G)$ , decreases as the band gap is increased. This is seen in Figure 7 where the number of photons absorbed is plotted against the semiconductor energy gap. Second, the voltage increases as the band gap increases due to the reduction in  $I_0$ , the dark current.<sup>10</sup> Figure 8 shows how  $\eta_{\max}$  varies with  $E_G$ .<sup>12</sup> The upper curve is calculated using standard p-n junction theory; the lower curve shows the result when the junction reverse saturation departs from its theoretically predicted dependence on  $E_G$ . Note that these curves are for the solar spectrum that exists above the atmosphere. The optimum band gap is 1.6 eV; at that point  $\eta_{\max}$  is 20 per cent higher than that of silicon. Note that in the lower curve there is little difference among the various materials.

#### CALIBRATION AND EFFICIENCY MEASUREMENTS

Figure 9 shows the current-voltage characteristic for a silicon photovoltaic cell. For convenience, the first quadrant is used for this plot instead of the fourth. This cell has an efficiency of 7.8 per cent, as measured in sunlight with a  $V_{\max}$  of 0.52 volt and an  $I_s$  of 12 milliamperes. Note the rectangular characteristic of this curve. A comparison of the cell's operation in sunlight and in artificial light is also shown. This comparison is given to show how efficiency is measured with an artificial light source. The major problem here is that one cannot easily duplicate the solar spectrum with an artificial light source; the efficiency of a solar cell depends on the spectrum used. However, if the same number of carriers or short-circuit current is produced in a solar cell by an artificial light source as would be produced by sunlight, then the effective intensity of the artificial source is said to be the same as the intensity of the sun as given by an absolute-power measuring device such as a pyrliometer. For the curves given in Figure 9, the sunlight intensity was measured by the pyrliometer to be 72.6 milliwatts. The artificial light source was then adjusted to produce the same short-circuit current, and, as can be seen from the figure, the current-voltage characteristic obtained with sunlight was duplicated within a few per cent. Small deviations

---

<sup>12</sup> J. J. Loferski, "Theoretical Considerations Governing the Choice of the Optimum Semiconductor for Photovoltaic Solar Energy Conversion," *Jour. Appl. Phys.*, Vol. 27, p. 777, July, 1956.

might be expected from cell to cell if the diffusion length varies by very much. This serves as a convenient laboratory method of measuring efficiency. The same technique can be used for other semiconductors; however, a separate light calibration is required for each material.

Presently available silicon solar energy converters have yielded efficiencies as high as 14 per cent; in production quantities, however, efficiencies run between 7 and 10 per cent. Such cells can be connected in series or parallel to increase the voltage or current. These cells are the easiest of all semiconductor devices to make, the major cost being that of producing the single-crystal silicon wafers. Assuming 10 per

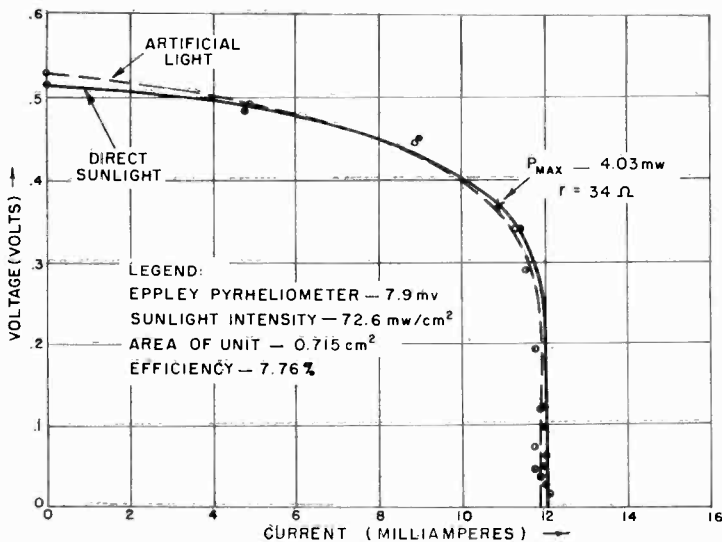


Fig. 9—Comparison of silicon current-voltage characteristics in sunlight and in artificial light.

cent efficiency and a solar-radiation flux of  $100 \text{ mw/cm}^2$  (the average sunlight intensity in the northeastern part of the United States during the summer), a one-kilowatt solar power supply would be ten square meters in area, cost \$200,000 and weight 20 pounds.

#### EXPERIMENTAL RESULTS WITH GaAs, InP AND CdTe

Figure 8 shows three semiconductors which, because of their availability and stability, were selected for experimental verification of the theory. These materials are the III-V compound semiconductors GaAs and InP, and the II-VI compound CdTe.

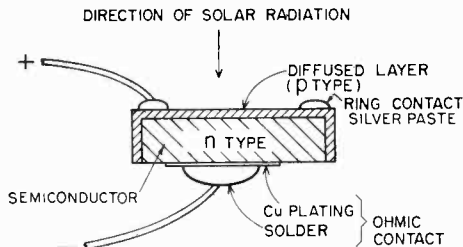


Fig. 10—Experimental photovoltaic cell.

Two techniques were used to make p-n junctions on these new materials, namely, the diffusion process and the alloy process. These techniques are similar to those employed with germanium and silicon, but the scheme for doping the materials is somewhat different. In general, a column II element in the periodic table converts GaAs or InP into a p-type semiconductor, while a column VI element converts it to n type. For CdTe a column I or VI element yields p type and a column VII or II element yields n type. Figure 10 shows the construction of a typical diffusion cell.

The major problems encountered in making efficient solar converters from these new materials were:

- (1) Making suitable ohmic contact to the n and p regions. Rectifying or high-resistance contacts lower the output voltage and current appreciably. In general, metallic plating and soldering, or an indium alloy dot solves the problem. Figure 11 shows

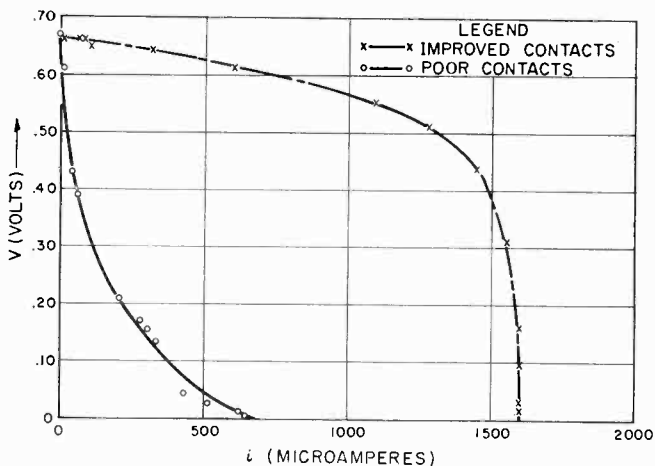


Fig. 11—Effect of contacts on current-voltage characteristics of GaAs solar cell.

the difference in current-voltage characteristics caused by poor contacts in GaAs.

(2) The need for low resistivity in the p- and n-type regions. This is required to obtain the maximum voltage per junction and a low series resistance. This problem is solved by using highly doped original material and by controlling the alloy or diffusion process to get a maximum impurity concentration.

(3) The fact that the p-n junctions do not behave according to theory. This can be caused by crystal imperfections, current leakage across the junction, or poor ohmic contact. The solution

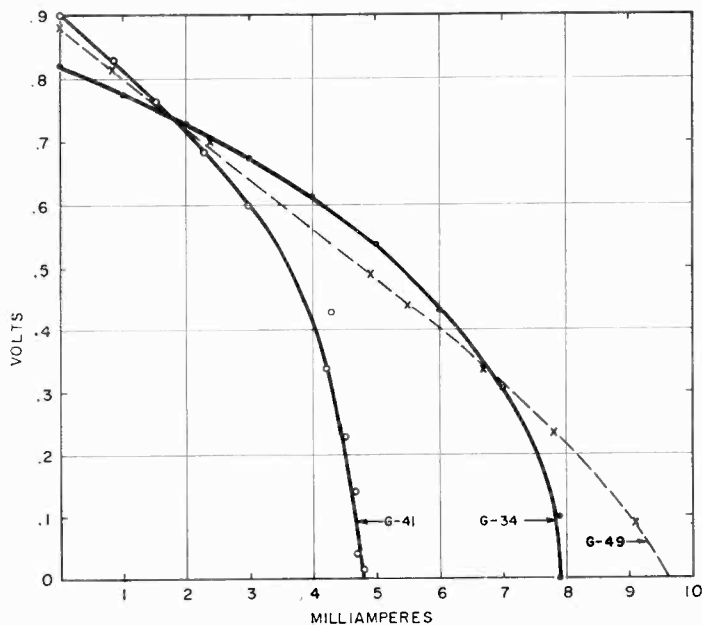


Fig. 12—Current-voltage characteristics of GaAs diffusion cells.

to this problem lies in better material, proper etching, lower diffusion temperature, and improved ohmic contacts.

Solar cells were successfully made with GaAs, InP, and CdTe. Figure 12 shows typical current-voltage plots for GaAs cells in an artificial light equivalent to sunlight of about  $100 \text{ mw/cm}^2$ . The curves were obtained by varying the load resistance and measuring the voltage and current while the units were illuminated. The units were made by baking n-type GaAs in cadmium vapor for four hours (G34 and G41) and 40 hours (G49). Note that the open-circuit voltage is as

high as 0.9 volt. This is a consequence of the large energy gap of GaAs and should be compared to a maximum voltage of .55 volt in silicon. The impedance of these units at maximum power is about 100 ohms. The best efficiency yet obtained is 6.5 per cent in GaAs in small areas.<sup>13</sup> For cells about one square centimeter in area, efficiencies of 5 per cent have been obtained.

Figure 13 shows the results obtained with InP. The units were made by the alloy process where a zinc indium dot was fired onto the InP at 500° C for 10 minutes. The zinc converts the n-type InP to p-type where it recrystallizes after alloying. The ohmic contact was

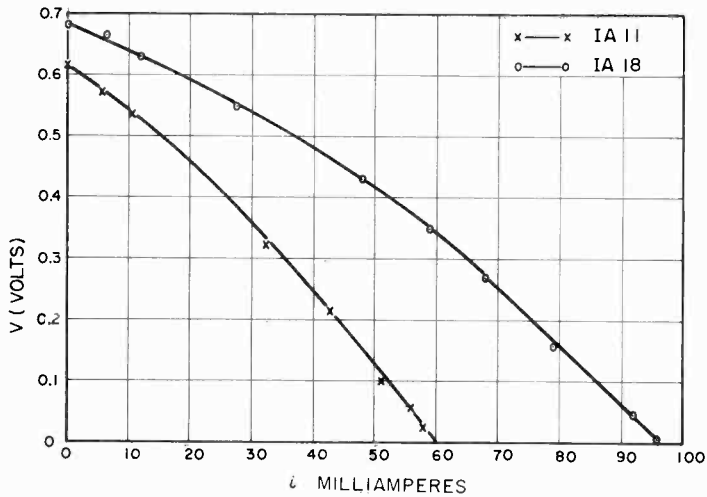


Fig. 13—Current-voltage characteristics of InP alloy junctions.

alloyed indium. Because of the presence of the dot, the exposed face was masked so that the effective area was about 0.1 square centimeter. The maximum efficiency of IA-18 was 2 per cent. Note that the curves are nearly linear. This implies the existence of a large internal resistance, about 1200 ohms for IA-11 and 700 ohms for IA-18. This is probably due to poor ohmic contact as supported by the low short-circuit current which is about 1 milliampere compared to about 10 milliamperes for the GaAs.

The results for CdTe are shown in Figures 14 and 15. In general, the technology of CdTe is behind that for GaAs and InP, and the use

<sup>13</sup> D. A. Jenny, J. J. Loferski, and P. Rappaport, "Photovoltaic Effect in GaAs p-n Junctions and Solar Energy Conversion," *Phys. Rev.*, Vol. 101, p. 1208, February, 1956.

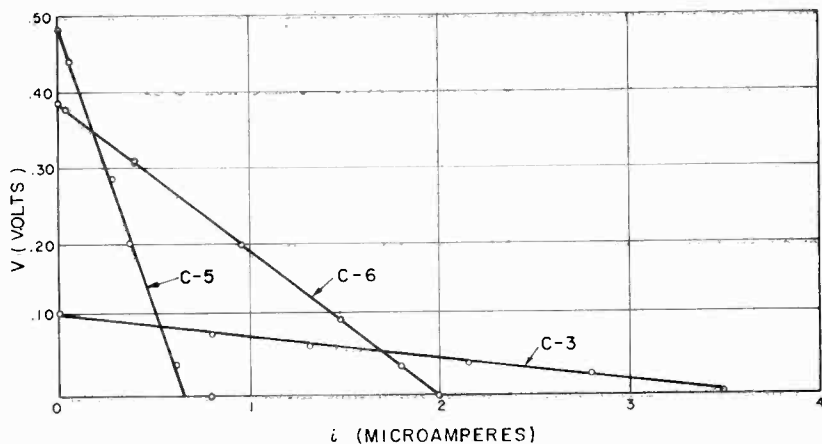


Fig. 14—Current-voltage characteristics of CdTe diffusion cells.

of this material is hampered by the lack of low-resistivity crystals. Figure 14 shows three current-voltage curves for diffusion-type junctions in CdTe. C-5 and C-6 were baked in iodine vapor at 800° C for 4 hours and C-3 in sodium vapor at 800° C for 4 hours. Indium was used as the ohmic contact to the n-type base wafer and silver paste to the diffused region. The output voltage is rather low considering the large band gap (1.45 ev), and the short-circuit current is about 1/1000 of that in the other materials, thus reflecting a very high series resist-

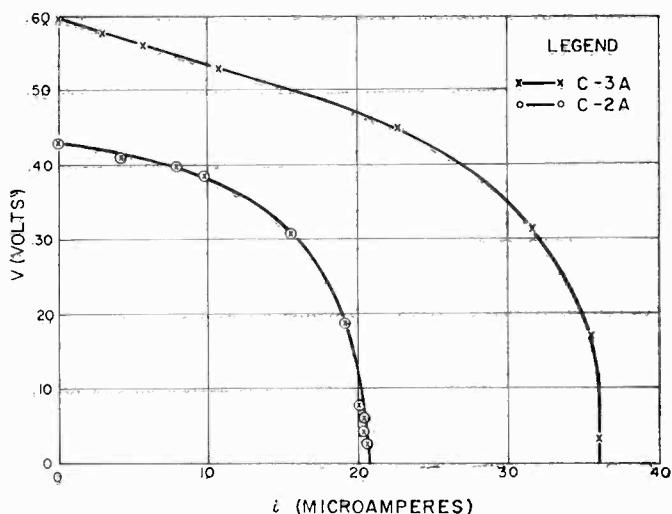


Fig. 15—Current-voltage characteristics of two CdTe alloy junctions.

ance. This is also evident from the straight-line characteristic of the curves. The resistance given by the slopes of these lines is  $10^6$  ohms for C-5,  $2 \times 10^7$  ohms for C-6, and  $3 \times 10^4$  ohms for C-3.

Figure 15 shows the results on the alloy-type CdTe units. The junction was prepared by alloying indium into p-type CdTe at  $600^\circ$  C for 10 minutes. Here the curves are rectangular, thus indicating considerably lower series resistance. The maximum conversion efficiency in CdTe has been achieved with the alloy-type junction and is 2.1 per cent.

#### WORK ON CdS

Some interesting results were obtained with CdS solar cells by a group at the Wright Air Development Center under the general direction of D. C. Reynolds.<sup>14</sup> According to theory, CdS should be low on the efficiency scale. Because of its large band gap, 2.4 ev, only about  $\frac{1}{5}$  of the solar photons should be absorbed. Spectral-response measurements show, however, that a large absorption takes place in the region considerably beyond the cutoff at .8 ev where the crystal should be transparent. This accounts for the high efficiencies which Reynolds reports to be as much as 7.5 per cent.<sup>15</sup> This material does not obey the usual theory and is not understood. It may be possible that some ternary compound which has a considerably smaller band gap than CdS, is formed near one of the contacts, thus accounting for the response at lower energy. Reynolds finds extremely long "diffusion lengths" in CdS. He finds the optimum thickness of a cell is about 0.9 millimeter and suggests this is due to exciton migration or a luminescence effect. A third explanation may be in the possibility of the formation of impurity bands in the heavily doped CdS.

A description of the cells is of interest. CdS crystals were grown by the vapor-phase method and made n-type by indium doping to about  $10^{-2}$  cm. They were cut to about  $1 \times 1 \times .09$  centimeter. The surfaces were roughened and copper was plated onto one face and diffused into the interior at  $460^\circ$  C for less than one minute making a p-type layer between 1 and 10 microns thick. Contact to this layer was made with a mercury-loaded epoxy resin. Contact to the n-region was made by soldering after zinc and copper plating. This resulted in a back-wall type cell as contrasted to the front-wall cells made of silicon and GaAs where the barrier is at the front surface.

<sup>14</sup> D. C. Reynolds, "The Photovoltaic Effect in Cadmium Sulfide Crystals," *Trans. Conf. on the Use of Solar Energy*, University of Arizona Press, Vol. 5, p. 102, 1955.

<sup>15</sup> D. C. Reynolds, private communication.

Figure 16 shows a series of current-voltage curves as a function of temperature on a CdS cell obtained from Reynolds. This cell had an over-all  $\eta_{\max}$  of 4 per cent as measured in sunlight. Note the excellent square shape of the current-voltage curve. The  $V_{\max}$  is 490 millivolts and  $I_s$  is 4.5 milliamperes. It could be expected that  $V_{\max}$  should be well over 1 volt in a 5 per cent efficient CdS cell according to the usual theory. One disappointing characteristic here is the rapid fall-off of  $I_s$  with temperature compared to the almost constant  $I_s$  of GaAs and silicon. Because of this and the usual decrease in  $V_{\max}$  of about 2 mv/°C, the CdS  $\eta_{\max}$  falls faster with temperature than either silicon or GaAs. In fact, it appears that CdS behaves like a material with a band gap of 0.8 to 1.0 ev rather than 2.4 ev. At present there

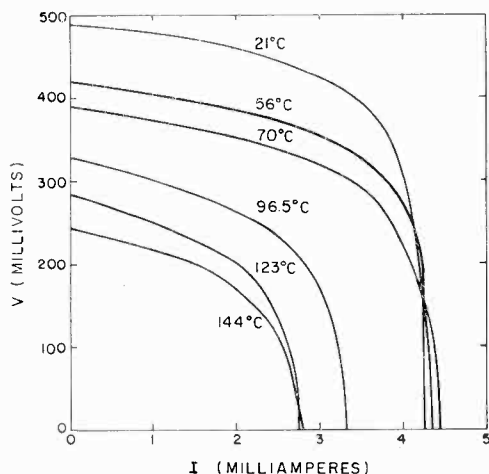


Fig. 16—Current-voltage curves for CdS at various temperatures.

does not seem to be any high-temperature advantage in using currently available CdS cells.

#### EFFECT OF INCREASED TEMPERATURE

One expects any device utilizing semiconductors to be sensitive to temperature change, and photovoltaic cells are no exception. Calculations were made to see how the maximum efficiency as a function of band gap varies with temperature. It was assumed that the short-circuit current was relatively independent of temperature, an assumption generally borne out experimentally, and that the main variation that one observes is due to the fact that  $V_{\max}$  is a function of  $I_0$ , a quantity quite sensitive to temperature.

Figure 17 shows the results of these calculations.<sup>16</sup> Here, the efficiency is plotted as a function of the energy gap with the temperature as the parameter. There are two main points: First, the optimum semiconductor energy gap increases as the temperature increases; thus at room temperature cadmium telluride is the optimum material, while at 300° C, the optimum is material "Z" with an energy gap of 1.8 ev. The materials of "Y" and "Z" may be ternary compounds—combinations of GaAs and GaP, for example. Second, the relative efficiency increases at higher temperatures when a higher

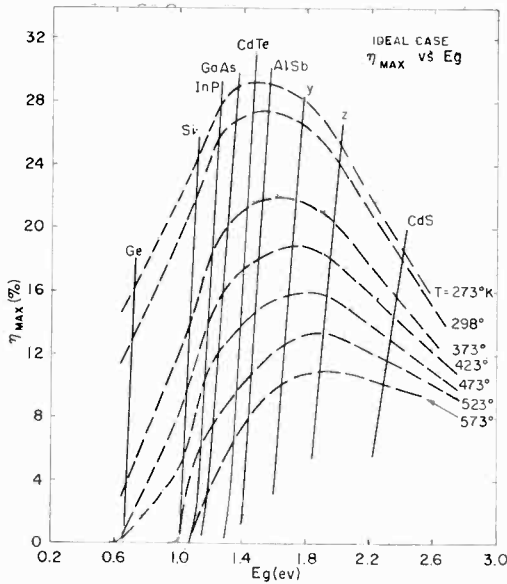


Fig. 17—Efficiency versus energy gap for various temperatures.

band-gap material is compared to silicon. For example, a comparison between silicon and GaAs at 150° C shows that GaAs would be almost twice as efficient a converter as silicon. At room temperature, however, GaAs is not quite 20 per cent better than silicon. On these curves, CdS, although somewhat better than silicon at 150° C, is still not as good as GaAs would be. As a result of these calculations, GaAs is considered the most promising material for use as a high-temperature (~200° C) solar converter.

Figure 18 shows some specific temperature measurements on silicon.

<sup>16</sup> J. J. Wysocki and P. Rappaport, "The Effect of Temperature on Photovoltaic Solar Energy Conversion," to be published.

This is an early silicon device having a somewhat lower efficiency than those made today, but the temperature results are typical of all silicon devices. Note that the maximum voltage decreases with temperature at the rate of  $2 \text{ mv}/^\circ \text{C}$ . As shown by the middle curve, the short-circuit current remains relatively constant with temperature. The bottom curve, showing the decrease in maximum power with temperature, has a slope of approximately  $.02 \text{ mw}/^\circ \text{C}$ .

Figure 19 shows similar results for a GaAs cell. These curves are

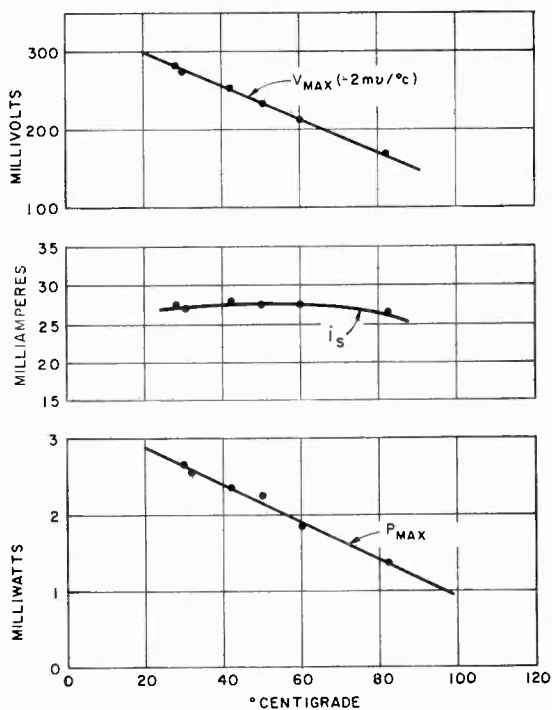


Fig. 18—Variation of silicon-solar-cell parameters with temperature.

for one of the better cells made of this material. Many other GaAs cells have shown quite varied characteristics, many of which were poorer than the one shown. As shown in the figure, the voltage decreases at the rate of  $1.7 \text{ mv}/^\circ \text{C}$ , the current is reasonably constant, and the power decrease is somewhat less than that of a silicon unit.

#### A HIGH-VOLTAGE PHOTOVOLTAIC CONVERTER

Since the major expense in making silicon solar converters is in

the production of the single crystal, possibilities of preparing cells by deposition methods such as evaporation and sputtering were studied. During this work, a very interesting effect was discovered by Pensak and later worked on by Goldstein.<sup>17</sup> They evaporated cadmium telluride at an oblique angle onto a Pyrex® substrate which was heated to a temperature between 100° and 200° C. With a film thickness of about one micron, they found that the films could produce a potential of as much as 1500 volts per centimeter under bright illumination.

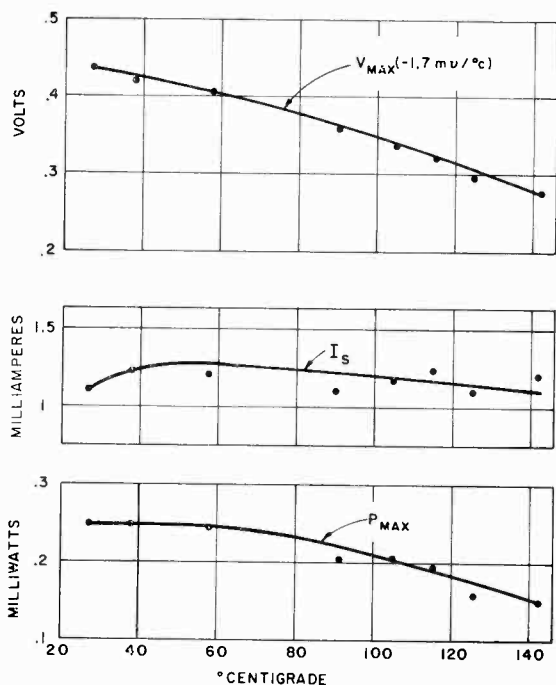


Fig. 19—Variation of GaAs alloy-junction-solar-cell parameters with temperature.

Figure 20 shows the current-voltage characteristic of the CdTe evaporated films. Note the high impedance and high voltages. Decreasing the temperature increases the voltage, until about 300 volts is achieved at liquid nitrogen temperatures. Such films exhibit resistance on the order of  $10^{13}$  ohms per square centimeter in the dark,

<sup>17</sup> B. Goldstein and L. Pensak, "High-Voltage Photovoltaic Effect," *Jour. Appl. Phys.*, Vol. 30, p. 155, February, 1959.

\* Registered trade mark.

and, as a result, the currents produced by such cells are quite low. As a matter of fact, these cells have energy-conversion efficiencies of only about  $10^{-4}$  per cent at present. However, this is a breakthrough into a new and interesting type of photovoltaic converter which warrants further research.

Figure 21 shows schematically the structure of these films. The film on glass is shown at the top. Contacts are made by using a transparent conducting coating and silver paste. To explain the extremely high voltages, one must assume the existence of many p-n semiconductor barriers, possibly grain boundaries, that are somehow connected

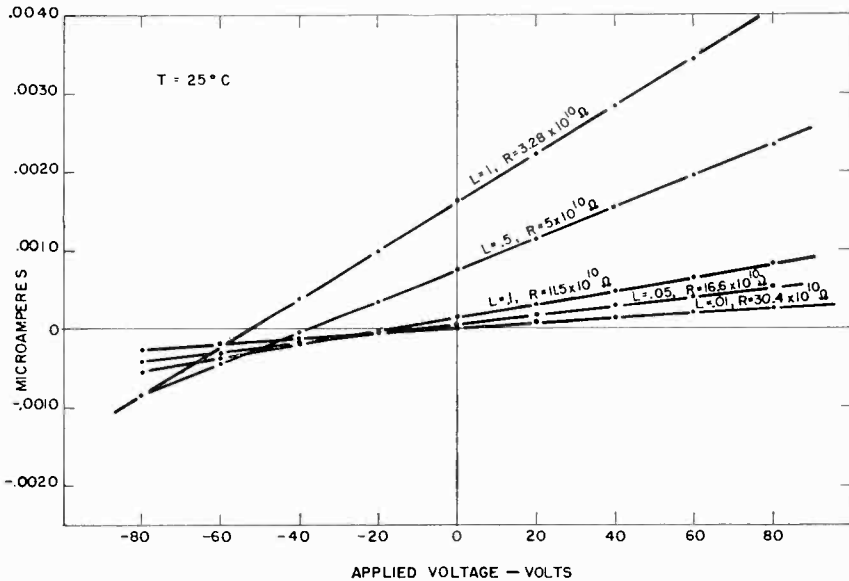
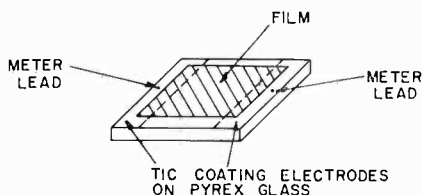


Fig. 20—Current-voltage characteristics for CdTe films at varying light intensities.

in a series chain. This in itself, however, is not sufficient to explain the results, since such a series connection would result in a voltage typical of just one barrier. The remaining barriers would cancel one another. Therefore it must be assumed that the barriers are asymmetric. Such an arrangement is shown schematically at the bottom of Figure 21, where a steep junction is shown between the n-p transition and a rather broad junction between the p-n transition. With light shining normally on such a configuration and assuming a short lifetime, it can be seen that carriers may be collected in the n-p region but not from the p-n region, because those carriers generated in the

p-n region would very easily recombine before being collected. These asymmetries may also be caused by impurity gradients, lifetime inhomogeneities, or stacking faults which are hexagon-to-cubic crystal-structure transitions. Such stacking faults have been observed in II-VI compounds. Work in  $\text{ZnS}^{18}$  has shown correlations between a high-voltage photovoltaic effect (produced by ultraviolet radiation) and stacking-fault structures. Voltages of 50 to 100 volts have been observed at room temperature and of 350 to 400 volts at liquid-nitrogen temperatures.



TYPICAL PHOTOVOLTAIC CELL

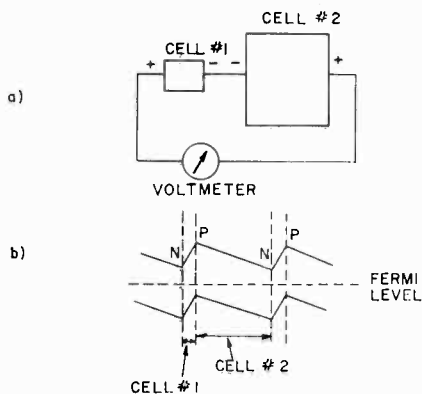


Fig. 21—Representations of series-connected cells.

#### IMPROVEMENT OF EFFICIENCY

There are five areas for improvement in the efficiency of single-crystal-type solar converters. Not all of the areas can be optimized independently of the others; a good compromise must be sought.

#### *Spectrum Matching*

Here the problem is one of utilizing the maximum energy of the

<sup>18</sup> S. G. Ellis, F. Herman, E. E. Loebner, W. J. Merz, C. W. Struck, and J. G. White, "Photovoltages Larger Than Band Gap in ZnS Crystals," *Phys. Rev.*, Vol. 109, p. 1860, March, 1958.

photons absorbed. Only for photons of band-edge energy is this realized. At higher photon energies, the excess energy beyond the band gap is imparted to the electron-hole pairs and is eventually dissipated as heat. A considerable improvement in efficiency could be realized if this problem were solved. Jackson has suggested<sup>19</sup> the possibility of using sandwich structures of differing-band-gap semiconductors. Sunlight first strikes the widest-gap material, which absorbs part of the spectrum and transmits the rest to the next-widest-gap semiconductor. This material absorbs part of the spectrum and transmits the rest in turn to the next material, and so on. Jackson calculates that for three semiconductors of 0.94-, 1.34-, and 1.91-eV band gap respectively, a solar conversion efficiency of 69 per cent is possible, and, where ten different materials are used, 86 per cent efficiency is theoretically possible.

Such devices would be difficult to construct mechanically, and each semiconductor would require a separate electrical connection. Series or parallel connection of the different semiconductors would degrade the individual  $V_{\max}$ 's or  $I_s$ 's. Connecting the layers in series would be feasible if the generated current in each layer were equal. The optical reflection from each interface would have to be reduced by special interference films. Such cells would be very expensive; it would be much more economical to use more area and lower efficiency for most applications.

#### *Reflection and Surface Recombination*

These two problems are grouped together, since it appears that the optimum condition exists when a compromise between the two is made. A surface having low optical reflection shows high surface recombination (loss of generated carriers by recombination at the surface) and vice versa. Prince has measured a 4 per cent reflection on 10 per cent efficient silicon solar cells, whereas normal clean silicon surfaces have a 30 per cent reflection coefficient.<sup>1</sup> If a steep doping gradient or band-gap gradient (such as GaP on GaAs) is built in very close to the surface, even high surface recombination or a high absorption coefficient does little harm, since the carriers are accelerated inward towards the junction before recombination can take place.

#### *Bulk Recombination*

Here, the problem is to place the junction at the optimum depth

<sup>19</sup> E. D. Jackson, "Areas for Improvement of the Semiconductor Solar Energy Converter," *Trans. Conf. on the Use of Solar Energy*, University of Arizona Press, Vol. 5, p. 122, 1955.

below the surface so that the greatest number of generated pairs are collected by the junction. A large diffusion length of about  $10^{-2}$  centimeter is required to collect carriers generated by near-band-gap radiation. Such diffusion lengths are difficult to obtain where a semiconductor is highly doped, and where it has first to be subjected to high temperatures in the fabrication procedure. In general, where a junction is shallow (limited by high series resistance) the carriers produced by high-energy photons that do not get trapped by the surface are collected, while the ones generated by longer wavelengths are lost due to bulk recombination. The opposite becomes true as the junction is made deeper.

#### *V<sub>max</sub> Limited to Less Than the Band Gap*

The  $V_{\max}$  for good silicon cells is about  $\frac{1}{2}$  the value theoretically possible for a junction formed by highly doped n- and p-type regions. In GaAs, this voltage has been as high as  $\frac{2}{3}$  of the gap. While it is not possible to realize the complete band-gap voltage, higher doping should yield higher efficiencies.

#### *Series and Shunt Resistance*

These parameters can reduce efficiency seriously; however, in practice it is not difficult to eliminate them entirely. Once the proper doping has been achieved, optimum contact arrangement can be employed to negate these two parameters. A shallow junction will add to series resistance, and here again junction depth must be optimized.

### CONCLUSIONS

The advantages of present solar cells as energy conversion devices are,

(1) Photovoltaic cells have given the highest over-all conversion efficiency from sunlight to electricity yet measured. The best value reported is 14 per cent.

(2) Such cells are easy to fabricate, being one of the simplest of semiconductor devices.

(3) They have unlimited life.

(4) They have high power-to-weight ratio for satellite applications. Cells having an efficiency of 10 per cent yield 50 watts per pound on the ground in sunlight of  $100 \text{ mw/cm}^2$ , and about 12.5 watts per pound on a satellite in sunlight of  $135 \text{ mw/cm}^2$  where tumbling, rotation, cell matching, higher temperature, light losses in cover, and other factors are taken into account. A cell 15 mils thick with contacts is considered in the above.

(5) Photovoltaic cells are area devices that don't require high temperatures for high efficiencies, thus eliminating lenses and concentrators in all but very special applications.

(6) In large-scale application, the problems of power distribution by wires could be eliminated by the use of solar cells at the site where the power is required.

The two main disadvantages to date are the high cost and the need for a storage device.

In the near future, silicon solar cells should be available with efficiencies in the 15 per cent range. Cells using other materials or combination of materials should be capable of 20 per cent conversion efficiency, and large-area polycrystalline films in the square-foot range might yield 5 per cent efficiency. Such devices will represent very strong competition in the solar-energy-conversion field for the new thermoelectric or thermionic devices which are showing promise.

#### ACKNOWLEDGMENT

It is a pleasure to thank Mr. William Cherry of USARDL for his enthusiastic support of the work at the RCA Laboratories during the past four years. Dr. J. J. Loferski of RCA Laboratories has been a major contributor to much of the work discussed. Messrs. L. Pensak and J. J. Wysocki and Dr. B. Goldstein of RCA Laboratories have also contributed to the material used. Figure 3 is reproduced here through the courtesy of Dr. M. B. Prince of Hoffman Semiconductor Division. Thanks are also due to Mr. D. C. Reynolds for the use of CdS cells from the Wright Air Development Center.

# PATTERN SYNTHESIS — SIMPLIFIED METHODS OF ARRAY DESIGN TO OBTAIN A DESIRED DIRECTIVE PATTERN\*

BY

GEORGE H. BROWN

Radio Corporation of America,  
Princeton, N. J.

*Summary*—Mathematical methods of determining the magnitude and phase of the current distribution over an extended linear antenna aperture in order to obtain a desired directive radiation pattern are described. It is shown that the radiation pattern and the current distribution form a set of Fourier transforms, thus yielding a ready solution to the problem. By adding a pattern in an imaginary zone to the desired real pattern, many current distributions or array configurations are found, all of which give the same desired pattern in the real zone.

## INTRODUCTION

**D**URING World War II, the writer and his colleagues were many times confronted with the task of designing large-aperture antennas to produce critically shaped beams with minimum side lobes and with specific rates of change of the main beam. The work of Wolff<sup>1</sup> in applying Fourier series to relate the radiation pattern to a linear array of point sources of radiation led us to the infinite Fourier integral and to a ready solution to many problems by forming a set of Fourier transforms to relate the desired directive pattern and the necessary current distribution.

P. M. Woodward<sup>2</sup> has published a powerful method of dealing with the problem in which he combines graphical and analytical methods. Careful reading of his paper reveals that he was fully aware of the Fourier-integral relationship and that he realized the value of sometimes proceeding into the imaginary angular domain. It is felt that this paper may supplement his exposition and assist in clarifying some of the obscure points.

---

\* Manuscript received March 16, 1959.

<sup>1</sup> Irving Wolff, "Determination of the Radiating System Which Will Produce a Specified Directional Characteristic," *Proc. I.R.E.*, Vol. 25, p. 630, May, 1937.

<sup>2</sup> P. M. Woodward, "A Method of Calculating the Field Over a Plane Aperture Required to Produce a Given Polar Diagram," *Jour. Inst. Elec. Eng.*, Vol. 93, Part IIIA, p. 1554, March-May, 1946.

FIELD INTENSITY WHEN CURRENT DISTRIBUTION IS AN  
EVEN FUNCTION

When the currents in an array are specified as to magnitude and phase angle, the calculation of the resulting radiation pattern is not usually a very complicated operation. The converse operation, that of specifying the field pattern and then determining the current distribution, is quite another problem.

In Figure 1, we have a sheet of current with the current distributed symmetrically about the center as an even function; that is,  $i(z) = i(-z)$ . The field due to the two small current elements shown in Figure 1 is

$$dE = 2Ki(z) \cos\left(\frac{2\pi z}{\lambda} \sin \theta\right) dz, \quad (1)$$

where  $i(z)$  is the current per unit width. The current at all points in the sheet is of constant phase.

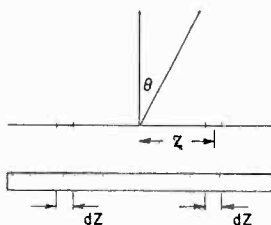


Fig. 1—A radiating current sheet.

The total field due to the entire sheet is

$$E(\theta) = 2K \int_{z=0}^{z=W/2} i(z) \cos\left(\frac{2\pi z}{\lambda} \sin \theta\right) dz, \quad (2)$$

where the sheet is of width  $W$ . Equation (2) may be written as

$$E(\theta) = 2K \int_{z=0}^{z=\infty} i(z) \cos\left(\frac{2\pi z}{\lambda} \sin \theta\right) dz, \quad (3)$$

with the understanding that  $i(z)$  in the integral is zero when  $z$  has a value greater than half the width of the sheet.

We are in general interested in the field variation over a range of angles from  $\theta = -90^\circ$  to  $\theta = 90^\circ$ . Thus if we substitute  $x = \sin \theta$ ,

we will be interested in the field in the interval between  $x = -1$  and  $x = 1$ . Then (3) becomes

$$E(x) = 2K \int_{z=0}^{z=-\infty} i(z) \cos\left(\frac{2\pi z}{\lambda} x\right) dz. \quad (4)$$

Now in Equation (4) let us substitute a new variable,  $v = 2\pi z/\lambda$ .

$$E(x) = \frac{\lambda}{\pi} K \int_{v=0}^{v=\infty} \cos(vx) dv \times i(v). \quad (5)$$

It is readily seen that in this case where we have chosen  $i(v)$  to be an even function of  $v$ ,  $E(x)$  is constrained to be an even function of  $x$ .

#### FIELD INTENSITY WHEN CURRENT DISTRIBUTION IS AN ODD FUNCTION

Let us now consider an arrangement where we have negative symmetry in the current distribution. Then the current distribution is an odd function of  $z$  and  $i(z) = -i(-z)$ . In addition,  $i(z)$  is constant in phase for all values of  $z$ . The field intensity distribution is then

$$E(x) = j \frac{\lambda}{\pi} K \int_{v=0}^{v=\infty} \sin(vx) dv \times i(v). \quad (6)$$

It is seen that  $E(x)$  is an odd function of  $x$ . In addition,  $E(x)$  leads the current distribution,  $i(v)$ , by  $90^\circ$ .

#### THE FOURIER-INTEGRAL RELATIONSHIP

A single-valued continuous function,  $E(x)$ , that exists in the interval from  $x = -\infty$  to  $x = +\infty$  may be expressed in terms of the infinite Fourier integral,

$$\begin{aligned} E(x) &= \frac{1}{2\pi} \int_{\beta=-\infty}^{\beta=\infty} E(\beta) d\beta \int_{v=-\infty}^{v=\infty} \cos v(\beta - x) dv \\ &= \frac{1}{2\pi} \int_{\beta=-\infty}^{\beta=\infty} E(\beta) d\beta \left[ \int_{v=-\infty}^{v=\infty} \cos(v\beta) \cos(vx) dv \right. \\ &\quad \left. + \int_{v=-\infty}^{v=\infty} \sin(v\beta) \sin(vx) dv \right] \end{aligned} \quad (7)$$

If  $E(x)$  is an even function, that is,  $E(x) = E(-x)$ , the last term in Equation (7) disappears and  $E(x)$  is given by

$$\begin{aligned} E(x) &= \frac{2}{\pi} \int_{\beta=0}^{\beta=\infty} E(\beta) d\beta \int_{v=0}^{v=\infty} \cos(v\beta) \cos(vx) dv \\ &= \frac{2}{\pi} \int_{v=0}^{v=\infty} \cos(vx) dv \int_{\beta=0}^{\beta=\infty} E(\beta) \cos(v\beta) d\beta. \end{aligned} \quad (8)$$

Then equating Equations (5) and (8),

$$\frac{\lambda}{2} Ki(v) = \int_{\beta=0}^{\beta=\infty} E(\beta) \cos(v\beta) d\beta. \quad (9)$$

Thus, if  $E(x)$  is an *even* function, Equation (9) gives the necessary current distribution to produce the desired field distribution.

When  $E(x)$  is an odd function, that is,  $E(x) = -E(-x)$ , the first term in Equation (7) vanishes and

$$E(x) = \frac{2}{\pi} \int_{v=0}^{v=\infty} \sin(vx) dv \int_{\beta=0}^{\beta=\infty} E(\beta) \sin(v\beta) d\beta. \quad (10)$$

Equating Equations (6) and (8),

$$j \frac{\lambda}{2} Ki(v) = \int_{\beta=0}^{\beta=\infty} E(\beta) \sin(v\beta) d\beta. \quad (11)$$

So, if  $E(x)$  is an *odd* function, Equation (11) gives the necessary current distribution to produce the desired field distribution.

Equations (9) and (11) show an integration on  $\beta$  from zero to infinity. Since  $x$  or  $\beta$  lies between  $-1$  and  $1$  for real values of the angle  $\theta$ , we can say that for all values of  $x$  outside of this interval, the field shall be considered to be zero. This, however, is not a necessary restriction. It will be seen later that it may indeed be desirable to specify  $E(x)$  in this imaginary domain.

If the desired field pattern is neither even nor odd (Figure 2a), an even function to be used in Equation (9) may be obtained by the method shown in Figure 2b. Similarly, an odd function to be used in Equation (11) may be obtained as shown in Figure 2c.

for all values of  $x$ , out to infinity, Equation (9) would yield a current distribution such that

$$i\left(\frac{2\pi z}{\lambda}\right) = 1 \quad \text{when } -B < \frac{2\pi z}{\lambda} < B,$$

and

$$i\left(\frac{2\pi z}{\lambda}\right) = 0 \quad \text{when } \frac{2\pi z}{\lambda} < -B \text{ or } \frac{2\pi z}{\lambda} > B.$$

If, however, we desire this same field intensity distribution in the region of real angles ( $-1 < x < 1$ ) and assume that  $E(x)$  is zero for all values of  $x$  greater than unity or less than minus one, Equation (9) becomes the sum of two sine-integral functions,

$$\frac{\lambda}{2} Ki(v) = \frac{1}{2B} [\text{Si}(B+v) + \text{Si}(B-v)], \quad (14)$$

a solution which differs materially from the constant current over a finite aperture which results when the field pattern is considered to exist in both the real and imaginary regions.

#### AN EXPONENTIAL FIELD DISTRIBUTION

As another example, we shall examine the case of an even distribution of field where the field drops off on either side as

$$E(\theta) = \mathcal{E}^{-a \sin \theta},$$

or

$$E(x) = \mathcal{E}^{-ax}.$$

Figure 4 shows this field intensity distribution for a specific value of  $a$  equal to 0.5 and the field distribution extends to values of  $x$  greater than unity. At some value of  $x = x_1$ , the field drops to zero and remains at zero for all values of  $x$  greater than  $x_1$ . Then Equation (9) yields

$$\frac{\lambda}{2} Ki(v) = \frac{a [1 - \mathcal{E}^{-ax_1} \cos(vx_1)] + v \mathcal{E}^{-ax_1} \sin(vx_1)}{a^2 + v^2}. \quad (15)$$

Figure 5 shows three current distributions with  $a = 0.5$  and  $x_1 = 1$ ,  $x_1 = 2$ , and  $x_1 = \infty$ . Here are three separate current distributions all of which yield the same field intensity distribution in the real region.

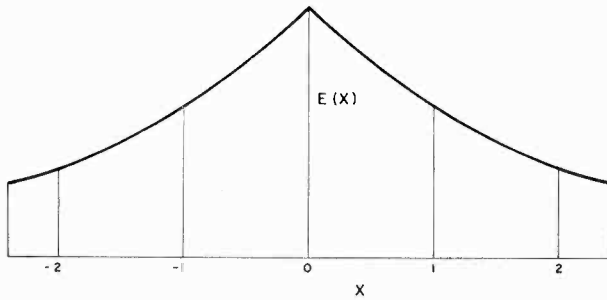


Fig. 4—An even function of field intensity distributed exponentially ( $a = 0.5$ ).

It is evident that the case where  $x_1$  is infinite yields the most conservative current distribution.

A TILTED-BEAM PATTERN WITHOUT SIDE LOBES

Equations (9) and (11) have been very useful in developing large antennas with narrow single beams and for lobe-switching antenna systems. This has been done by contriving even and odd functions of field intensity which are readily integrable and which fit each other.

A useful even-function field distribution is

$$E(x) = \cos^2\left(\frac{\pi x}{4 x_1}\right) = \frac{1 + \cos\left(\frac{\pi x}{2 x_1}\right)}{2} \tag{16}$$

from  $x = -2x_1$  to  $x = +2x_1$  with  $E(x)$  equal to zero for all other

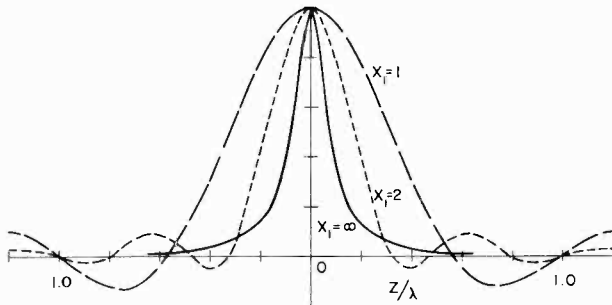


Fig. 5—Three current distributions which yield the field distribution of Figure 4.

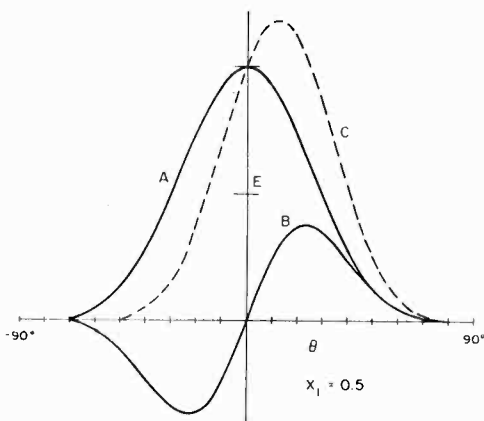


Fig. 6—A distribution of field useful in lobe-switching antenna systems, plotted as a function of  $\theta$ . Curve A is the even function of field, Curve B is the odd function, while Curve C is the composite field ( $x_1 = 0.5$ ).

values. When  $x = x_1$ , the field intensity is one-half of the maximum value. A corresponding odd function is

$$E(x) = \cos^2\left(\frac{\pi x}{4 x_1}\right) \sin\left(\frac{\pi x}{4 x_1}\right) \quad (17)$$

between  $x = -2x_1$  and  $x = 2x_1$  with  $E(x)$  equal to zero for all other values.

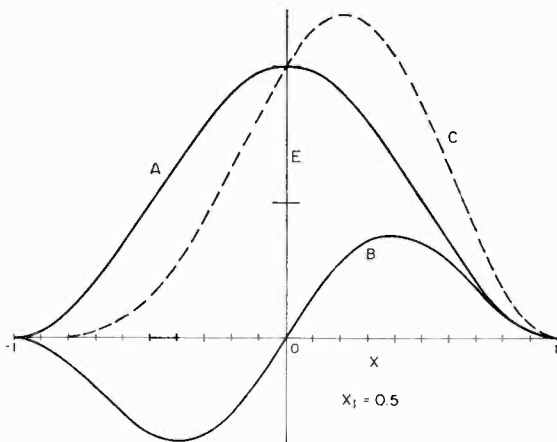


Fig. 7—The field distributions of Figure 6 replotted as a function of  $x$  ( $x = \sin \theta$ ).

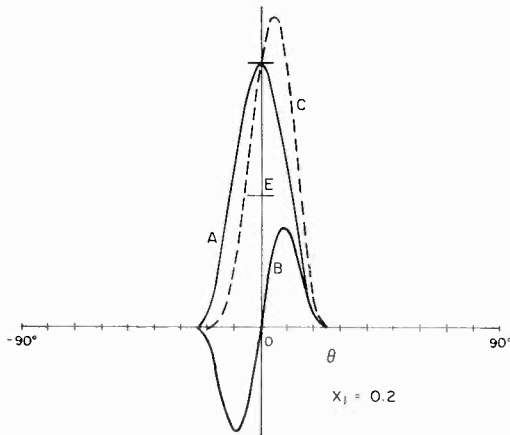


Fig. 8—Lobe-switching antenna patterns similar to Figure 6 ( $x_1 = 0.2$ ).

Curve A of Figure 6 shows the even function of Equation (16) plotted as a function of the angle,  $\theta$ , while Curve B shows the odd function of Equation (17), where  $x_1 = 0.5$ . Curve C is the sum of the two field patterns. The same set of curves have been replotted as a function of  $x$  in Figure 7.

Figures 8 and 9 show the corresponding family of curves where  $x_1 = 0.2$ . Successful lobe-switching antennas have been designed where the current distribution yielding Curve B has been rapidly reversed in phase.

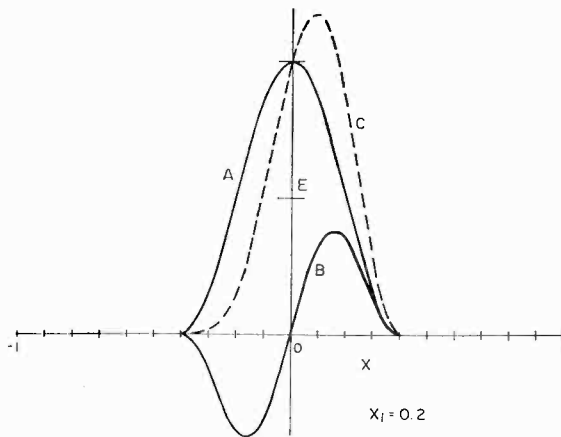


Fig. 9—A replot of Figure 8 as a function of  $x$ .

Figure 10 shows the total field distribution for a very narrow beam, where  $x_1 = 0.04$ .

When Equation (16) is substituted into Equation (9), we find

$$\begin{aligned} \frac{\lambda}{2} Ki(v) &= \int_{\beta=0}^{\beta=2x_1} \cos^2\left(\frac{\pi \beta}{4 x_1}\right) \cos(v\beta) d\beta \\ &= \frac{\sin\left(\frac{4\pi z}{\lambda} x_1\right)}{\frac{4\pi z}{\lambda}} \left[ \frac{1}{1 - \left(\frac{4zx_1}{\lambda}\right)^2} \right]. \end{aligned} \quad (18)$$

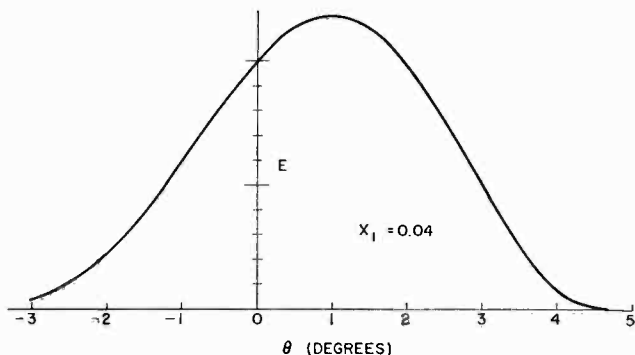


Fig. 10—A very narrow tilted beam ( $x_1 = 0.04$ ).

At the center of the array,  $z = 0$ , the current density is

$$\frac{\lambda}{2} Ki(0) = x_1 \quad (19)$$

so the current density distribution is obtained by dividing Equation (19) into Equation (18).

$$\frac{i(v)}{i(0)} = \frac{\sin\left(\frac{4\pi z x_1}{\lambda}\right)}{\frac{4\pi z x_1}{\lambda}} \left[ \frac{1}{1 - \left(\frac{4zx_1}{\lambda}\right)^2} \right]. \quad (20)$$

This function is plotted in Figure 11 as  $i_s$  and is equally applicable to the field distribution of Figures 7 or 9.

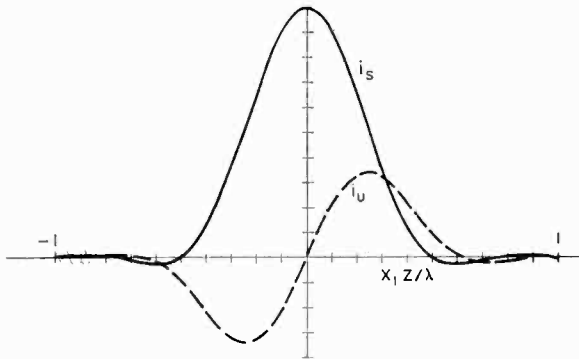


Fig. 11—The odd and even functions of current distributions to obtain the field intensities of Figures 6-10.

When the odd function of Equation (17) is substituted into Equation (11),

$$j \frac{\lambda}{2} Ki(v) = \frac{x_1}{2\pi} \left( \frac{4zx_1}{\lambda} \right) \cos \left( \frac{4\pi zx_1}{\lambda} \right) \left[ \frac{1}{\left( \frac{1}{2} \right)^2 - \left( \frac{4zx_1}{\lambda} \right)^2} - \frac{1}{\left( \frac{3}{2} \right)^2 - \left( \frac{4zx_1}{\lambda} \right)^2} \right]. \quad (21)$$

To normalize this odd function of current density, we divide Equation (21) by the current density of the even function at  $z = 0$  and obtain

$$j \frac{i(v)}{i(0)_s} = \frac{1}{2\pi} \left( \frac{4zx_1}{\lambda} \right) \cos \left( \frac{4\pi zx_1}{\lambda} \right) \left[ \frac{1}{\left( \frac{1}{2} \right)^2 - \left( \frac{4zx_1}{\lambda} \right)^2} - \frac{1}{\left( \frac{3}{2} \right)^2 - \left( \frac{4zx_1}{\lambda} \right)^2} \right]. \quad (22)$$

The odd-function current-density distribution of Equation (22) is plotted as the unsymmetrical distribution labelled  $i_u$  in Figure 11.

It should be noted that the current distribution of Equation (22)

lags that of Equation (18) by  $90^\circ$ . Then the total current distribution and the corresponding phase angle to obtain the pattern C of Figures 7 and 9 are given in Figure 12.

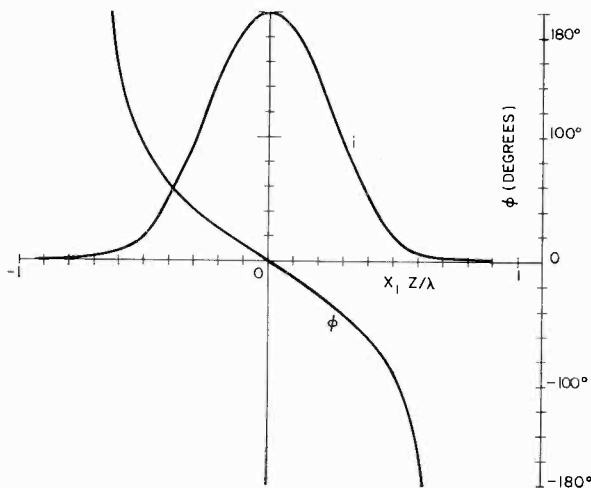


Fig. 12—The current distribution of Figure 11, shown in terms of total current magnitude and phase angle.

#### A BEAM-TILTED COSECANT-THETA PATTERN

A tilted beam with a cosecant distribution over most of the positive real angle has been of some interest. The total field distribution is shown in Figure 13a.

$$\begin{aligned}
 E(x) &= 0 && \text{when } x < 0, \\
 E(x) &= x/x_1 && \text{when } 0 < x < x_1, \\
 E(x) &= x_1/x && \text{when } x_1 < x < 1.
 \end{aligned}$$

To find the even and odd distributions to use in the Fourier integrals, we follow the procedure demonstrated in Figure 2. Then for the even function, shown in Figure 13b, we obtain

$$\begin{aligned}
 E(x) &= \frac{x}{2x_1} && \text{when } 0 < x < x_1, \\
 E(x) &= \frac{x_1}{2x} && \text{when } x_1 < x < 1,
 \end{aligned}$$

and the even-function distribution of current density is

$$\frac{\lambda}{2} Ki(v) = \frac{1}{2x_1} \int_{\beta=0}^{\beta=x_1} \beta \cos(v\beta) d\beta + \frac{x_1}{2} \int_{\beta=x_1}^{\beta=1} \frac{\cos(v\beta)}{\beta} d\beta$$

$$= \frac{x_1}{2} \left[ \frac{(vx_1) \sin(vx_1) + \cos(vx_1) - 1}{(vx_1)^2} + Ci(v) - Ci(vx_1) \right]. \quad (23)$$

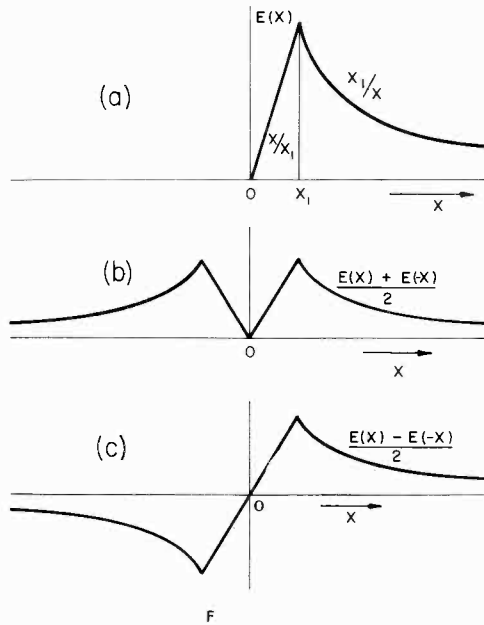


Fig. 13—(a) A cosecant field distribution; (b) The even-function component; (c) The odd-function component.

The odd-function distribution of field is

$$E(x) = \frac{x}{2x_1} \quad \text{when } 0 < x < x_1,$$

$$E(x) = \frac{x_1}{2x} \quad \text{when } x_1 < x < 1,$$

while the odd-function distribution of current density is

$$\begin{aligned}
 j \frac{\lambda}{2} Ki(v) &= \frac{1}{2x_1} \int_{\beta=0}^{\beta=x_1} \beta \sin(v\beta) d\beta + \frac{x_1}{2} \int_{\beta=x_1}^{\beta=1} \frac{\sin(v\beta)}{\beta} d\beta \\
 &= \frac{x_1}{2} \left[ \frac{\sin(vx_1) - (vx_1) \cos(vx_1)}{(vx_1)^2} + \text{Si}(v) - \text{Si}(vx_1) \right]. \quad (24)
 \end{aligned}$$

#### CONCLUSION

While it has been shown that the current distribution over an extended linear antenna aperture and the resulting radiation pattern form a unique set of Fourier transforms, the addition of a pattern in an imaginary zone to the real pattern produces many array configurations all of which give the same desired radiation pattern in the real zone.

# PRODUCTION OF FINE PATTERNS BY EVAPORATION\*†

BY

S. GRAY AND P. K. WEIMER

RCA Laboratories,  
Princeton, N. J.

*Summary*—In producing fine complicated patterns of conductors and insulators by evaporation through masks in vacuum, scattering of material from the masks and migration in the formed films can interfere with desired electrical, optical, and mechanical properties. Methods of measurement of scattering are presented. Scattering itself may be reduced by adjusting the properties of the mask and evaporation conditions. The effects of scattering can be reduced by treatment of the workpiece, as by heat treatment of a conducting pattern. Migration of silver can break down electrical insulation. Diffusion of aluminum into cryolite has been used to produce reverse patterns.

Many of these techniques have been applied to the construction of an experimental target for a tricolor pickup tube, which includes an array of interference filter strips registered with which are strips of semitransparent gold electrically connected in three groups. The width of the filter strips is .0007 inch. Each gold strip is .0005 inch wide and is insulated from its two neighbors across a gap of .0002 inch.

## THE FORMATION OF FINE PATTERNS

IN THE development of the tricolor Vidicon,<sup>1</sup> a television pickup tube designed to provide complete color video information from a single tube envelope, techniques were developed for the formation of fine complicated patterns by evaporation in vacuum. Red, green, and blue interference filter strips were produced in register with strips of semi-transparent conducting material. Each group of conducting strips belonging to a given primary color is electrically connected together to form a set, and each set is insulated from the other two. Figure 1 shows the type of pattern constructed with more than one thousand strips to the inch.

\* This paper was presented in part at The Fourth National Conference on Tube Techniques, New York, 1958.

† Manuscript received April 1, 1959.

<sup>1</sup> P. K. Weimer, S. Gray, H. Borkan, S. A. Ochs, and H. C. Thompson, "The Tricolor Vidicon—An Experimental Camera Tube for Color Television," *Proc. I.R.E.*, March 1955, pp. 370-371.

To form a pattern on a target by evaporation, the areas of the target on which a deposit is not required must be masked from the vapor stream. One method of providing such a mask is to deposit a photoresist pattern directly on the substrate prior to the condensation of a continuous sheet of material.\* Subsequent removal of the photoresist pattern carries away the layer formed by evaporation in the areas where it is not in direct contact with the substrate. This method

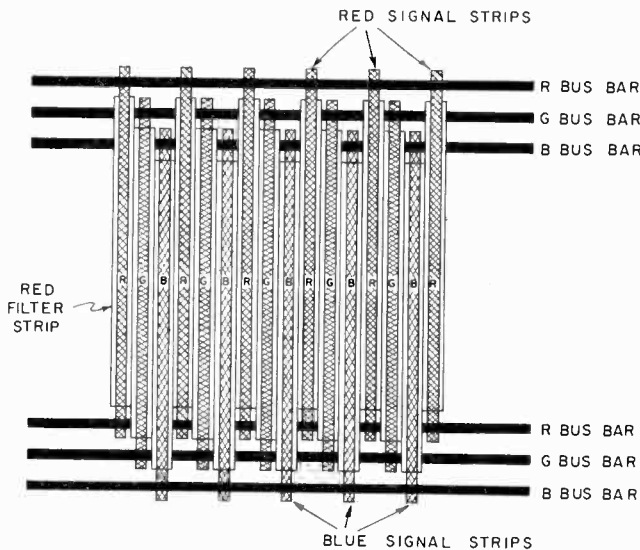


Fig. 1—Structure of an experimental tricolor Vidicon target. Red, green, and blue interference filter strips are cyclically arrayed. The filter strips, in crossing bus bars, insulate registered gold signal strips from the bus bars. The width of each signal strip is .0005 inch.

has the advantage of keeping the masked areas entirely clear of evaporated material but, when several different or overlapping patterns must be superimposed on the same target blank, it is inconvenient in many respects. For research purposes, this method does not allow as much freedom in the choice and thickness of materials to be evaporated as does the use of a separate close-spaced mechanical mask.

Mechanical masks permit a wide variety of patterns to be deposited in sequence by displacing the target relative to the mask between evaporations, without the danger of damaging the pattern as may

\* Fine patterns of dichroic filters have been made by this method by M. E. Widdop, formerly of the RCA Victor Division at Camden, N. J.

occur in removal of a photoresist. Metal masks produced by photoengraving techniques are suitable, or, as in the case of the tricolor Vidicon when strips are required, wire grills may be used.

Figure 2 is a cross section of a target receiving a deposit through a wire masking grill. Because of the width of the evaporation source, a penumbra is formed along the boundaries of the pattern. In order to reduce the penumbra, the evaporator should have the minimum practicable width and should be spaced as far as possible from the target, while the spacing of the mask from the target should be small. The target may also receive material in the mask shadow, since all the vapor incident on the mask may not condense there and may instead be scattered.

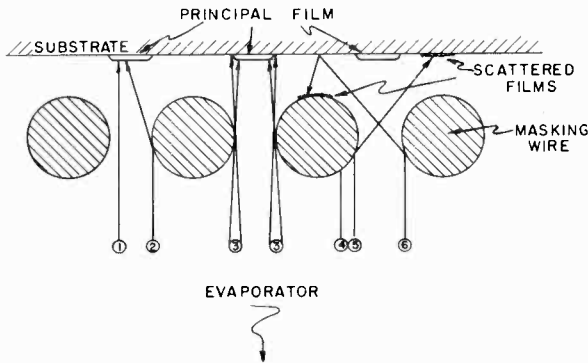


Fig. 2—Cross section of a target with a wire masking grill during evaporation: (1) Direct deposit; (2) Scattered material adding to principle film; (3) Penumbra deposits; (4) Deposit masked by the grill; (5) Scattered deposit terminating in shadow of the mask; (6) Scattered deposit terminating on grill.

In crowding a large number of successive deposits into fine dimensions, the scattering of material by the masks during deposit and the migration and diffusion in the films after formation introduce problems not encountered in general evaporation work. Optical, electrical, and mechanical properties of the patterns are affected. Methods have been found for minimizing some of the detrimental effects of scattering and for the use of mobility in the films to improve electrical properties.

#### SCATTERING FROM MASKS

Material may be scattered by the mask into both the exposed regions of the target and the shadow of the mask. In the shadow, material is deposited where none is desired. In the exposed areas, the addition of

scattered material produces films which differ physically from those formed entirely by direct deposit. The dependence of scattering on the material deposited, type of mask, and evaporation parameters has been investigated.

### *Effects of Scattering on Fine-Pattern Formation*

**Optical Effects**—Interference filters are produced by stacking layers of dielectric materials of different refractive indices or of partially transparent layers of metal and of dielectric, of prescribed optical thicknesses.<sup>2</sup> The optical transmission characteristics of the completed filter are determined by the complex refractive indices, thicknesses, and ordering of the component layers. The optical thickness of a layer is conveniently monitored during its formation by observing the transmission or reflection of monochromatic light by the filter. In an all-dielectric filter of the simplest design, in which all layers are an integral number of quarter-wavelengths in optical thickness at some specified wavelength, monitoring consists of observation of maxima and minima of transmission or reflection. Deposition of a layer is ended at a specified extremum.

Because of the addition to the growing film of material which has been scattered, the deposit in the pattern is thicker than a film formed simultaneously on an unmasked target at the same distance from the evaporator. The pattern itself should therefore be monitored by transmission through the evaporation mask (in this case, used as an optical mask).

The conventional high-refractive-index materials, zinc sulfide and zinc selenide, are most subject to scattering, as discussed later. A film formed from scattered material has lower refractive index than one formed by direct deposit. A composite film, formed of a mixture of material which has arrived by direct deposit and material which has been scattered from the mask, is not as dense as a film formed entirely by direct deposit. As a result, filter strips formed with zinc sulfide as the high-index component have a narrower reflection band and higher transmission in the reflection band than a filter formed in an extended sheet. Figure 3 shows a comparison of the spectral transmissions of sheet and strip filters constructed to the same design. Final adjustment of the spectral transmission of a filter must take into account the reduction in high index produced by scattering.

---

<sup>2</sup> K. M. Greenland, "Interference Filters in Optics," *Endeavour*, July 1952.

In the construction of a multiple filter pattern, a film of scattered material of lowered refractive index will be deposited on portions of the target which are later to support other filters, or will be added to filters which have ostensibly already been completed.

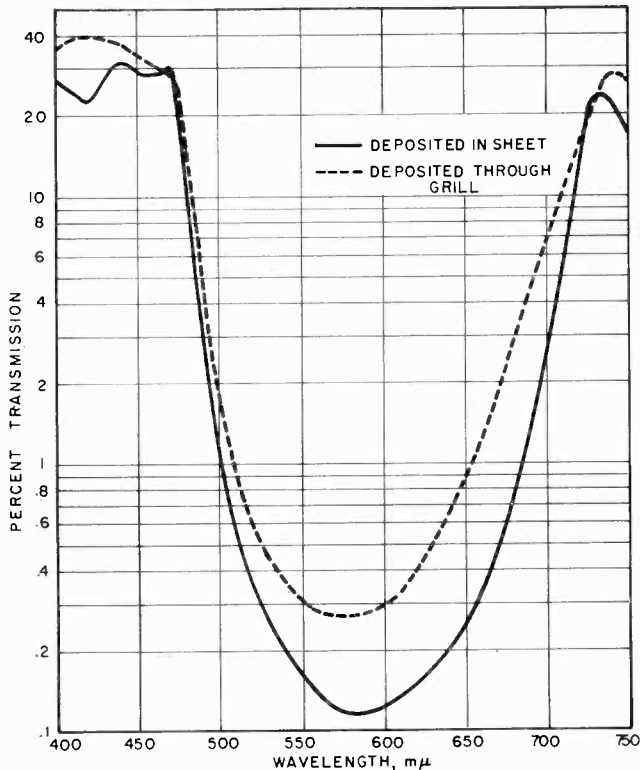


Fig. 3—Spectral transmissions of ZnS-CaF<sub>2</sub> interference filters constructed in a sheet and in strips to the same design. Strips are .0014 inch wide, 240 to the inch, and are covered with 50 per cent transmitting gold.

A pattern of Fabry-Perot filters,<sup>2</sup> which consist of a layer of dielectric sandwiched between layers of silver, may also be constructed by transmission monitoring through the masking grill. In this case, monitoring with monochromatic light at the wavelength of the peak filter transmission desired, one first deposits silver to a predetermined transmission. The dielectric is then deposited while transmission extrema are counted, and is terminated short of the required thickness of an integral number of half-waves in order to allow for the

phase-shift on reflection from the succeeding dielectric-metal interface. The final layer of silver is then deposited to a transmission maximum. The inclusion of scattered dielectric affects the thickness and refractive index of the formed dielectric film. This is not as serious as the inclusion of scattered silver for which the resulting films show higher absorption, so that the peak transmission of the produced filter for given pass-bandwidth and rejection efficiency is impaired.

**Electrical Effects**—Scattering will affect the electrical properties of a complicated fine pattern in two principle ways. When a conducting pattern is to be established in combination with films of dielectrics, insulating material scattered into regions in which electrical junctions are later to be formed will interfere with proper connection. In the formation of closely intermeshed conducting patterns, parts of which are to be electrically insulated from others, scattering from the mask may develop very thin shorting films.

**Mechanical Effects**—Turner<sup>3</sup> has shown how comparatively thick mechanically stable composite films may be deposited by evaporation if the stresses are balanced. For instance, a zinc sulfide layer is inherently under compression, while magnesium fluoride forms under tension. By selection of a ratio of thicknesses which corresponds to the ratio of stresses, a balance may be achieved. However, in designing optical filters, the primary requirements on layer thicknesses are determined by the optical properties desired. In practical construction of zinc sulfide-magnesium fluoride filters, some stress cancellation may be achieved, but total balance will rarely be attained.

A filter design which may be sufficiently compensated when constructed in a sheet so that adhesion to the substrate is enough to overcome residual stress, may peel from the substrate when it is constructed in strips. In the example just cited, this is a consequence of the incorporation of scattered zinc sulfide which produces a zinc sulfide layer under less compression. The uncompensated tensile forces in magnesium fluoride tear the filter away from its support.

#### *Measurement of Scattering*

**Dielectrics**—The scattering of dielectrics from masks may be detected and measured by a Fabry-Perot interference technique, as shown in Figure 4. A partially transparent sheet of silver is first deposited on glass. This is followed by a layer of the dielectric of interest, equivalently one-half wavelength thick. With the mask to be tested in place and with a section of the target completely shielded

<sup>3</sup>A. F. Turner and F. K. Truby, "Thin Films, Film Coated Articles and Methods of Making Same." U.S. Patent Number 2,858,240, Oct. 1958.

from the vapor stream, strips of dielectric are formed in a monitored thickness, which may be several half wavelengths. At this stage, dielectric material may be scattered from the mask, increasing the dielectric thickness in the gaps between the strips. The test sample is completed by the deposit of a second sheet of silver to peak the monochromatic transmission of the Fabry-Perot filter formed in the field where there are no strips.

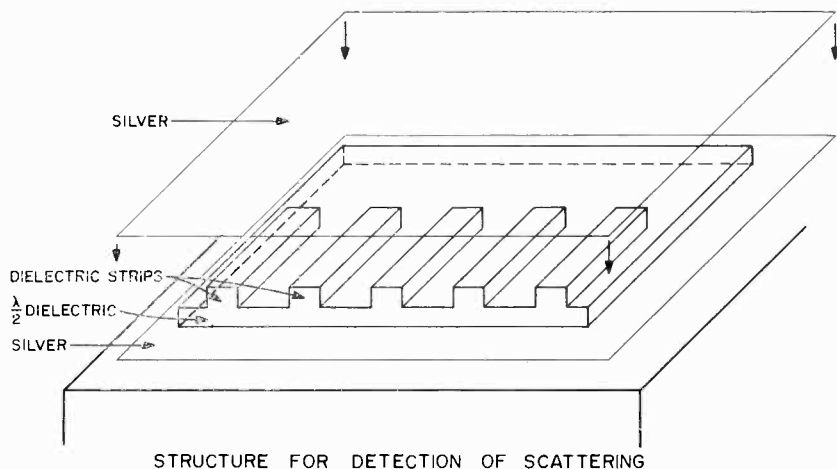


Fig. 4—Fabry-Perot experiment for detection of dielectric scattering.

If scattering has occurred in the masking operation, the peak transmission of the filter formed in the gap will occur at a longer wavelength than that for the field filter. A black and white print of a color photograph of a scattering pattern is shown in Figure 5. A shift in peak wavelength of 30 Å is measurable. This corresponds to measurement sensitivity of 15 Å in optical thickness of the dielectric layer in the first-order filter formed in the gaps. In Figure 5, the general scattering may be differentiated from the penumbra formed at the boundaries of strips by the width of the evaporator.

**Metals**—An indication of the scattering produced in deposit of a metal may be obtained by constructing interlocked patterns of strips and measuring the electrical conductance between the sets of strips. As is the case for gold, the conductivity of a very thin metallic layer is a function of the distance between electrodes because of the agglomerated nature of the deposit. The per-square conductivity is measured to be higher with more closely spaced electrodes. Nevertheless, with fixed pattern geometry and evaporation conditions, and a

given substrate, this conductance may be accepted as a valid measure of scattering.

### *Results of Scattering Measurements*

Scattering varies widely with the material, and with the mask and conditions of evaporation. A group of dielectrics conventionally used in making interference filters has been tested. This includes zinc sulfide, zinc selenide, magnesium fluoride, calcium fluoride and cryolite. Of the metals evaporated to form fine patterns, gold was most intensively investigated.

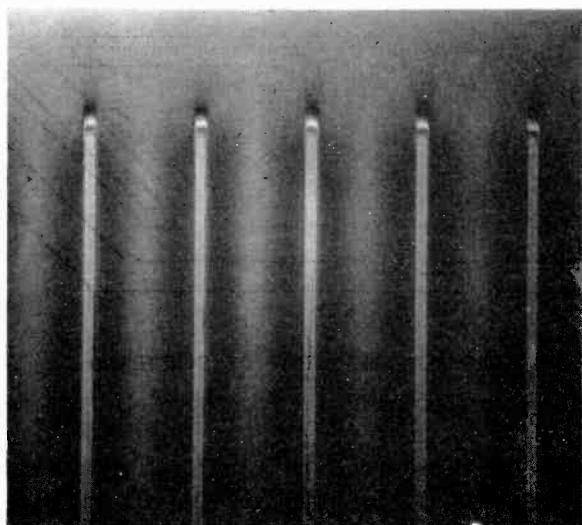


Fig. 5—Reproduction of a color microphotograph of a Fabry-Perot scattering test. Principle films, penumbras, and scattered films may be seen.

The data presented here were obtained with masking grills made of nichrome or magmo wire .003 inch in diameter wound 240 wires to the inch. These grills were stretched to reduce the wire diameter to the desired value. Spacing between the grill and the target for most of this work was .001 inch or less. The pressure in the system at the time of evaporation, as measured in a sidearm, was about  $1 \times 10^{-5}$  mm Hg. The evaporator was 10 inches below the mask.

Among the fluorides, scattering into the shadow of the wires was not detected; this means it was less than 0.25 per cent of the thickness of the material deposited in the strips. Zinc selenide, deposited at a rate which will give one quarter wavelength in optical thickness in two or three minutes, is two per cent scattered. Zinc sulfide is

most subject to scattering. The film in the shadow is 10 per cent the thickness of the direct deposit when the deposition rate is one quarter wavelength in five minutes.

The fractional scattering depends on the pressure in the system. Between  $8 \times 10^{-6}$  mm Hg and  $3 \times 10^{-5}$  mm Hg indicated pressure, scattering is roughly proportional to pressure. Consideration of the mean free paths of the evaporated particles in the residual gas and of the geometry of shadowing shows that the increase with pressure cannot be the result of additional collisions. Instead, a change in the surface condition of the mask dependent on the pressure is indicated, as will be discussed more fully later.

With slow deposition rates, scattering is increased. This effect has been detected with zinc selenide and is very marked for zinc sulfide. Fast rates are therefore preferred in constructing fine patterns of these materials. This is contrary to good procedure in forming dielectric layers in sheets, where slow rates produce films which are harder, denser, and less strained.

Speed of deposit and pressure in the system affect the scattering of gold in the same way as in the case of the zinc sulfide. However, for a metal which migrates on the substrate, as is the case with gold, there is no loss in quality of the film in using rapid evaporation rates, since the uniformity, the optical characteristics, and the conductivity all improve with faster deposition. Gold scattering has been shown to be dependent also on the nature of the surface of the mask. For instance, a freshly cleaned nichrome grill scatters much more heavily than does one which has been precoated with gold. A grill, precoated with gold, which has been left exposed to air loses its efficiency in reducing scattering.

Two inferences may be drawn regarding gold. Scattering is most heavy at the beginning of a deposit, as is also the case with zinc sulfide, and the accommodation coefficient of a mask for the evaporated material changes during a deposit, probably achieving equilibrium after some period. Considering these inferences and the observations of the effects of rate of deposition and pressure in the system, one can speculate that with a film of adsorbed gas on the mask, the accommodation coefficient is low and scattering is high. The mask surface reaches some equilibrium dependent on the rate of arrival of evaporated material and the rate of arrival of adsorbable residual gas.

Scattering also appears to depend on the method by which a masking grill has been manufactured. Masking grill of improved uniformity may be made by drawing the wire to size through a diamond die and winding it in the same operation onto a threaded mandrel which is

later split apart to form the grill.\* Such grills do not produce the general dielectric scattering observed with grills which have been stretched to size. Instead, highly localized scattering is produced from particular small sections of wire. What surface condition is responsible for this behavior, and how a surface condition can carry through an extended evaporation, are not known.

#### MIGRATION

No direct evidence for lateral migration of evaporated dielectric either during or subsequent to deposition has been observed. However, the lateral migration in metallic films, which is well known, affects the stability of conducting patterns. How control of migration may be used to improve the electrical and optical properties of such patterns is discussed later.

Silver exhibits unusual mobility, both transversely through sandwiches, and laterally. It is not feasible to construct an insulated cross-over between two metallic films when one of the metals is silver, since the silver diffuses into the fluorides, the sulfides, and the selenides, and the insulation is broken down. Silver in contact with gold will diffuse laterally along the gold. With a short bake at 200°C, it may diffuse 10 or 20 thousandths of an inch. The diffusion from a relatively heavy bar of silver along crossing gold strips is shown in Figure 6.

In a bake of 450°C, aluminum diffuses into a covering film of cryolite. Reverse patterns may be formed with the same mask. In one case, aluminum is deposited directly through the mask. For the reverse pattern, aluminum is deposited in a sheet, and is followed by a cryolite deposition through the mask. After baking, the regions in which cryolite has been deposited become both insulating and transparent. This is shown in Figure 7 for patterns produced with a photoengraved metal mask.†

#### REDUCTION OF THE EFFECTS OF SCATTERING

Through use of fast deposition rates and high vacuum and the selection and precoating of masks, scattering can be reduced. However, even in the presence of scattering, the electrical properties of complex fine patterns may be improved by treatment of the workpiece.

Electrical connection which might be disturbed by inclusion of a scattered dielectric film may be insured by incorporating silver into

---

\* This method was developed by C. W. Beadle at RCA Laboratories.

† The mask was obtained from Buckbee Mears Co., St. Paul, Minn.

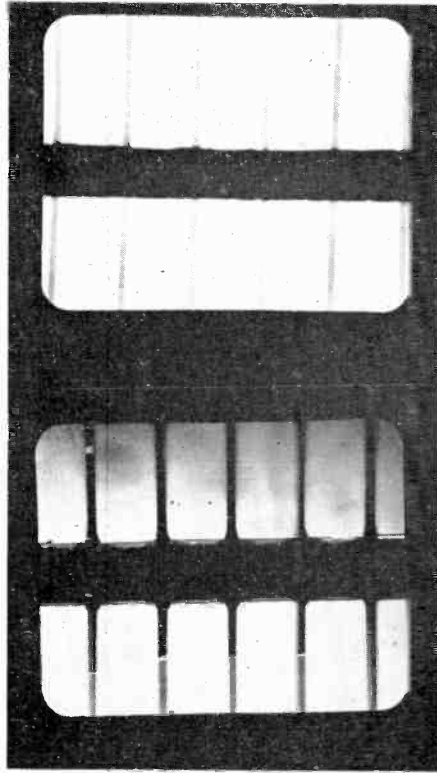


Fig. 6—Lateral diffusion of silver along gold. The heavy silver bars are .005 inch wide. The upper picture shows the pattern prior to baking. The lower picture shows the pattern after baking at 200°C. Silver has diffused along the semitransparent gold strips up to breaks in the strips.

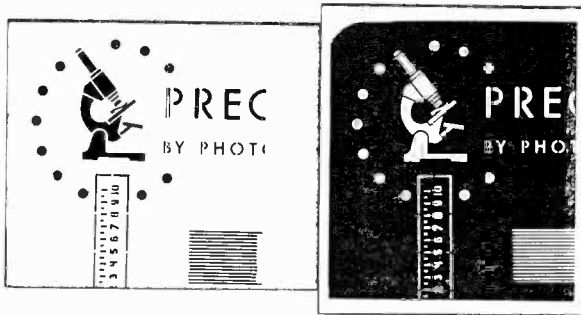


Fig. 7—Reverse patterns produced by evaporation. The pattern on the left is produced by evaporation of aluminum through a mask. The negative pattern is produced by depositing cryolite through the same mask onto a continuous sheet of aluminum, and subsequently baking the workpiece at 450°C.

the contact. The diffusion of silver may be relied upon to break down insulation where it is not desired.

Electrical properties are dependent on the substrate, especially in very thin metal films. This means a given amount of scattered metal deposited under set conditions will show different conductivity, depending on mobility on the substrate. The substrate may be selected so as to reduce interelement shorting. A film of aluminum oxide, made by forming a film of aluminum thin enough to be oxidized completely, is a particularly good substrate for a gold pattern, allowing good conductivity for the pattern elements themselves in conventional stable thicknesses, while restricting the conductivity between elements.

Mobility may be used to improve the properties of a conducting pattern. When a film of gold is baked, it improves in conductivity and optical transmission. As the baking temperature is increased, the film may continue to improve up to some temperature at which it shatters, breaks up into droplets, and becomes insulating. The break-up temperature is a function of the thickness of the film. A pattern which consists of desired conducting elements overlaid by a very thin but conducting film may be cleared by baking at a temperature between the two break-up temperatures. The thin scattered film is thereby made insulating, while the optical and electrical properties of the heavy elements are improved.

#### EXAMPLE OF A FINE PATTERN STRUCTURE: THE TRICOLOR VIDICON

Through use of fine pattern techniques described here, tricolor Vidicon targets were constructed as shown schematically in Figure 1. The bus bars are heavy strips of gold bonded to the glass with chromium, which provide common electrical connection for the conducting signal sets. The filter strips are all-dielectric interference filters, consisting of 10 or 12 layers. These strips are each .0007 inch wide, and are arranged to butt together.

Registered with the filter strips are the semitransparent gold signal strips, which have been included in the optical design of the filters. Each of the signal strips is .0005 inch wide. Each is insulated from its two neighbors by gaps of .0002 inch. The signal strips are connected at both ends to their corresponding bus bars, so that a single break in a signal strip does not seriously affect the operation of the target. Each target contains about 300 color triplets in an area of 0.27 square inch.

With gold bus bars and signal strips, interset insulation is satisfactorily provided at the crossovers by the filter strips. The resistance

between signal sets has been measured in many targets to be many megohms even when several volts is applied between sets. When higher conductivity between sets is observed, it is often due to local scattering of gold producing local shorts.

The resistivity of gold strips formed in this way is about the same as that of a continuous sheet, about 10 ohms per square for a fifty per cent transmitting film, provided the target includes only the conducting strip pattern. Measurement of the resistance of a signal set in a color target is not representative of the resistance of the strips themselves, since a scattered layer of dielectric only a few molecules thick between a signal strip and its bus bar presents a resistance much higher than that of the signal strip itself. Typically, the resistance of a signal set in the presence of random insulated connections is three times what is to be expected from the resistance of the strips.

A target is completed by the deposit by evaporation of a sheet of photoconductor. The tube of which the target becomes a part operates as a Vidicon as described in an earlier paper.<sup>1</sup>

# MEDIUM-POWER L- AND S-BAND ELECTROSTATICALLY FOCUSED TRAVELING-WAVE TUBES\*

By

D. J. BLATTNER,<sup>†</sup> F. E. VACCARO,<sup>‡</sup> C. L. CUCCIA,<sup>#</sup>  
AND W. C. JOHNSON<sup>#</sup>

*Summary*—Part I of this paper describes a developmental electrostatically focused traveling-wave tube. The tube employs a bifilar helix as both r-f circuit and electrostatic focusing structure, and can use either a parallel- or convergent-flow electron gun of conventional design. Outstanding advantages of this device are light weight, independence of environment, and freedom from ion oscillation.

Part II describes a product-development tube suitable for operation in both L and S bands at the five-watt level. The objectives for this tube included stable and long-life operation, rugged packaging with air-cooling of the collector, operability over a wide range of frequencies with a fixed set of helix voltages, and characteristics which were substantially reproducible from tube to tube. This tube is longer than the advanced-development tube described in Part I, operates at a higher gain and lower power level, and has lower beam current. New techniques and components developed for this tube are described; these include the technique for bonding the glass to the bifilar helices, and the capsule, helical couplers, attenuator, and electron-gun supports.

## PART I—ADVANCED DEVELOPMENT\*\*

### INTRODUCTION

TRAVELING-WAVE tubes usually employ a long, thin, cylindrical electron beam that must be confined continuously throughout its length by electric and/or magnetic forces. Although a somewhat similar beam is used in television picture tubes and image orthicons without confining forces, the density of the beam in these applications is several orders of magnitude smaller than that required in traveling-wave tubes. The common method of overcoming the diverging space-charge forces in a high-density stream of electrons

\* Manuscript received July 21, 1959.

<sup>†</sup> RCA Laboratories, Princeton, N. J.

<sup>‡</sup> RCA Electron Tube Division, Princeton, N. J.

<sup>#</sup> RCA Electron Tube Division, Harrison, N. J.

\*\* Part of this development was sponsored by the U. S. Air Force. Some of this material was presented at the 1958 I.R.E. National Convention: Blattner and Vaccaro, "The Estiatron — An Electrostatically Focused Medium-Power Traveling-Wave Tube," Convention Record, Pt. 3, pp. 101-105.

is to use an axial magnetic field, either uniform or periodic, along the axis of the beam. By use of a series of small ceramic permanent magnets to provide a periodic magnetic field on the axis of the beam, the weight and focusing power required can be reduced substantially

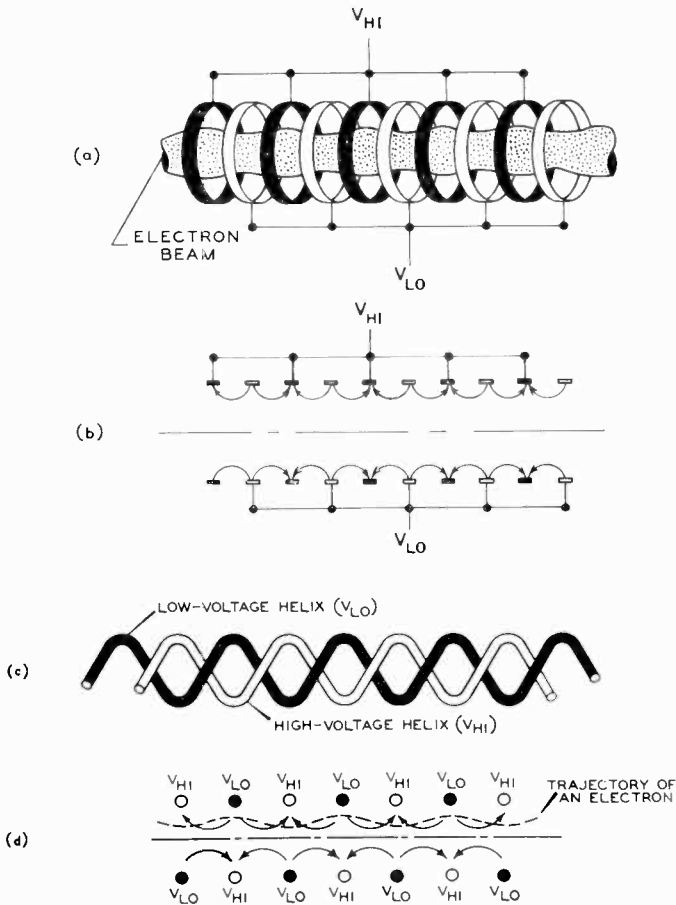


Fig. 1—Electrostatic focusing of an electron beam. (a) Electron beam flowing through a series of rings held at alternately high and low potentials. (b) The forces on an electron due to the electrostatic field. (c) Bifilar helix. (d) Electron flow through bifilar helix.

below that necessary for uniform magnetic fields. However, much of the bulk and weight in a packaged traveling-wave tube of this type is still due to the magnets. The use of electrostatic forces to focus the electron beam in a traveling-wave tube eliminates the need for a magnet structure, considerably reducing the weight of the packaged

tube and also eliminating the problem of alignment of the tube within the magnetic field.

### PERIODIC ELECTROSTATIC FOCUSING

A number of ways of accomplishing this type of focusing have been explored by several research laboratories. The simplest approach is to direct the electron beam through a succession of electrostatic lenses formed by a series of rings or disks held alternately at high and low potentials ( $V_{HI}$  and  $V_{LO}$ ) with respect to cathode. Such a structure is shown in Figure 1a. The electrostatic field resulting from the voltage between adjacent rings produces forces on an electron as shown by the arrows in Figure 1b. The electrons move slowly when they are in the vicinity of a low-voltage ring where the radial component of electrostatic force on them is directed inward, and faster when they are near the high-voltage rings where the electrostatic forces are directed radially outward. Because of this difference in velocity, the electrons spend more time in the neighborhood of the low-voltage ring. The over-all effect, therefore, is an inward focusing force on the electrons which tends to balance the space-charge repulsion in the beam.

Because the helix used in conventional traveling-wave tubes is a relatively simple structure that makes possible the transmission of r-f energy over extremely large bandwidths, it is apparent that an electrostatic focusing method that utilizes the helix structure is highly desirable. A convenient way of preserving the basic r-f properties of the helix and at the same time permitting electrostatic focusing is to interwind two helices in a bifilar manner, as shown in Figure 1c. An electrostatic focusing action similar to the one described above can be obtained by operating the two helices at different potentials, as shown in Figure 1d. The average beam velocity must be very nearly equal to the wave velocity to obtain interaction between the component of the r-f wave traveling along the tube axis and the electron beam. The average of the two helix voltages, therefore, must be approximately the voltage at which the tube would operate if it were focused by conventional means.

### DESIGN CONSIDERATIONS

Theoretical and experimental investigations of electrostatic focusing using bifilar helices have been made by Chang<sup>1</sup> and Tien.<sup>2</sup> Their

<sup>1</sup> K. K. N. Chang, "Confined Electron Flow in Periodic Electrostatic Fields of Very Short Periods," *Proc. I.R.E.*, Vol. 45, pp. 66-73, January 1957; K. K. N. Chang, "An Electrostatically Focused Traveling-Wave-Tube Amplifier," *RCA Review*, Vol. XIX, pp. 86-97, March, 1958.

work emphasized the beam entrance conditions necessary for a smooth laminar electron beam and those necessary to avoid beam instability. Although these focusing studies furnished the starting point for the development reported here, it was felt that laminar electron beams might not be essential in a traveling-wave-tube amplifier. Therefore, experiments were performed using conventional parallel-flow and convergent-flow electron guns instead of guns giving a thin hollow electron beam or a specially shaped distribution of current density. Care was taken to launch the beam from a drift tube well within the focusing field of the helices in order to avoid the defocusing effects of transverse field components. Care was also taken to insure that the bifilar helix was rigidly and accurately supported. For this purpose, a special construction technique was developed in which the glass bulb is shrunk directly onto the helix wires.



Fig. 2—Developmental Estiatron, complete with r-f input and output couplers, attenuator, and collector cooling fins.

### EXPERIMENTAL RESULTS

Studies were made with an experimental, medium-power, S-band, electrostatically focused traveling-wave tube employing bifilar helices. Figure 2 is a photograph of the experimental tube, complete with r-f input and output couplers, attenuator, and collector cooling fins. The tube, called an "Estiatron," employs a standard convergent-flow electron gun, coupled-helix-type input and output couplers, and external attenuator.

Figure 3 shows the excellent focusing performance obtained. The beam-current interception is plotted as a function of the focusing-voltage ratio (the difference between the high helix voltage and the low helix voltage, divided by the average helix voltage) for various beam permeances. For example, if the average helix voltage is 2000 volts, the voltage difference between helices would be 2000 volts at 1 on the abscissa, 1800 volts at 0.9, 1600 volts at 0.8, and so on. These

<sup>2</sup> P. K. Tien, "Focusing of a Long, Cylindrical Electron Stream by Means of Periodic Electrostatic Fields," *Jour. Appl. Phys.*, Vol. 25, pp. 1281-1288, October 1954.

data represent focusing of the electron beam without any r-f input signal to the tube.

As shown in Figure 4, the increase in beam-current interception due to r-f bunching of the beam is only slight—from 0.8 per cent without an r-f input signal to 1.5 per cent under saturated r-f conditions. These curves also indicate that the r-f performance is not very sensitive to changes in the helix-voltage difference. The output power and gain are essentially constant for helix-voltage differences ranging from 1600 to 2400 volts.

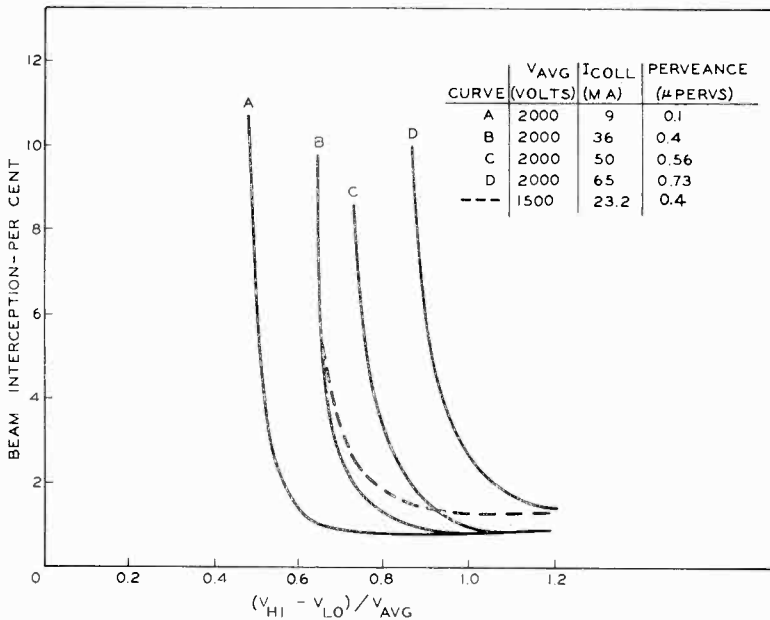


Fig. 3—Beam interception as a function of the ratio of voltage difference to average voltage.

Input-output characteristics of the tube are shown in Figure 5. The continuous-wave power output is plotted as a function of power input for three different frequencies with voltages fixed at each frequency. At 1900 megacycles, for example, gain is constant at 28 decibels up to a power output of 13 watts. The tube then saturates with 23 decibels gain at a power output of 21 watts.

Noise figure of the particular tube described here is about 25 to 30 decibels. This value is approximately the same as that quoted for magnetically focused traveling-wave tubes of the same power level.

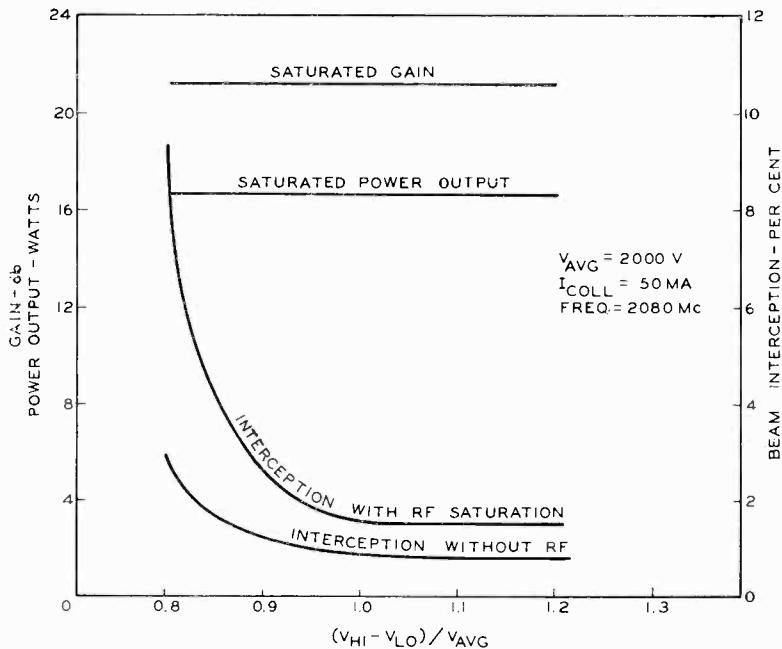


Fig. 4—Gain, power output, and beam interception as functions of the ratio of voltage difference to average voltage.

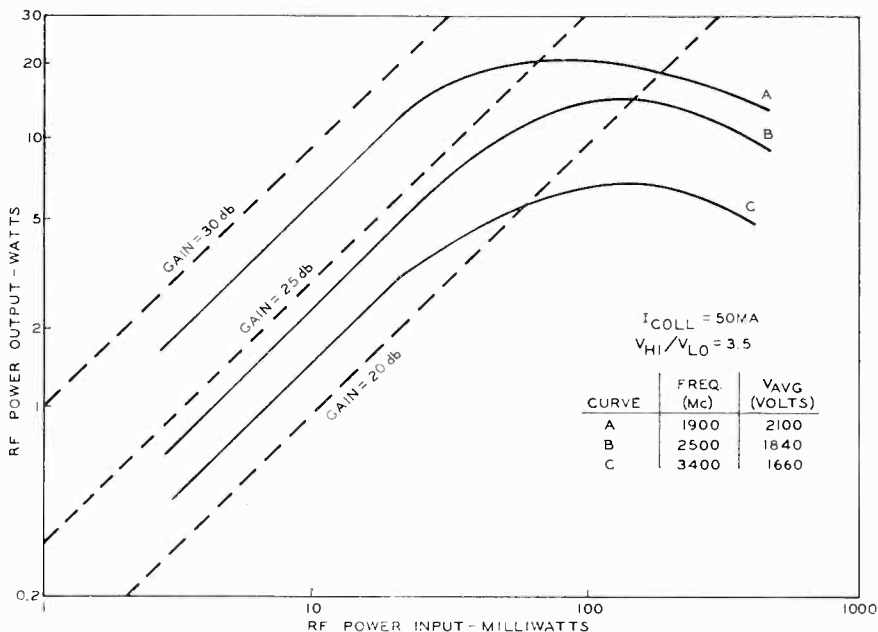


Fig. 5—R-F power output as a function of r-f power input.

Low-noise tubes can be built with slight modification of the present design.

The current intercepted by the low-voltage helix is negative, indicating that it is due to secondary emission and collected positive ions. Subsequent tests confirmed the absence of ion oscillations.

Tests were also performed with a parallel-flow electron gun, and virtually the same performance was observed. The tube with the parallel-flow gun was also tested in a solenoid with confined flow of the beam and the two helices at the same potential. Because the beam diameter in this case was smaller than that of the electrostatically focused beam, the measured gain was somewhat less.

### CONCLUSIONS

The advanced development work reported here demonstrated the practicality of traveling-wave tubes using nonlaminar electrostatically focused beams. With no compromise of the advantageous features of traveling-wave-tube amplifiers—large bandwidth, high gain, linear small-signal amplification—many of their disadvantages have been removed. The electrostatically focused traveling-wave tube requires no magnetic focusing field (hence no alignment), is light in weight, and can be made as independent of environmental conditions as any thermionic vacuum tube. The electrostatic field which focuses the electron beam also serves as an ion trap, insuring freedom from ion oscillation noise.

## PART II—PRODUCT DEVELOPMENT\*

### INTRODUCTION

A product-development program based on the Estiatron described in Part I resulted in a ruggedly packaged tube of stable operation providing a power output of five watts and a gain of 20 decibels over the frequency range from 2000 to 3500 megacycles. Figure 6a is a photograph of the packaged tube. The complete package is 18 inches long and  $1\frac{1}{2}$  inches in diameter and weighs less than two pounds. Most of this weight is contributed by the capsule and the mounting blocks.

Figure 6a also shows the components which are housed in the capsule, including the tube, the external attenuator, the input coupler at the gun end of the tube, the output coupler at the collector end of the tube, and the radiator. These components, with the addition of power supplies, are all that is required for microwave-signal amplification and beam focus. Any other components included in the final

---

\* This product development was done at Harrison by C. L. Cuccia and W. C. Johnson.

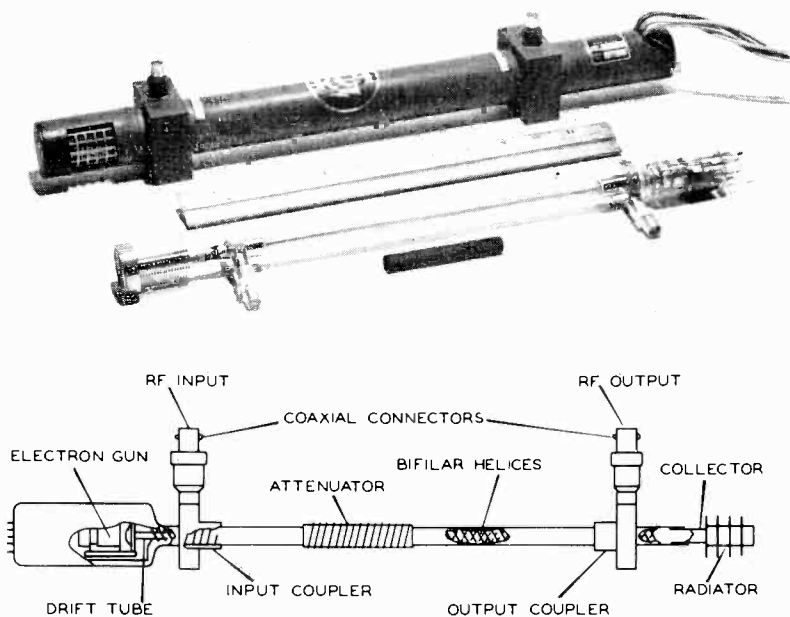


Fig. 6a (above)—Completed Estiatron and its enclosing package. 6b (below) Details of the electron tube, couplers, and attenuator of the Estiatron.

package are used for packaging and ruggedizing only. The simplicity of the structure shown is evidence of the attractive mechanical features provided by the Estiatron. Figure 6b shows details of many of the above components and the relative positioning of these components.

#### COMPONENTS OF THE ESTIATRON

Figure 7 shows the component parts of the tube itself, including

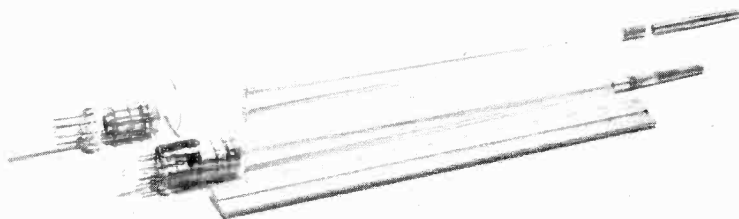


Fig. 7—Photograph showing the electron gun, envelope, and collector of an Estiatron before and after assembly.

the electron gun and its supporting stem, the glass envelope which contains and supports the bifilar-wound helices, and the collector. The electron gun may be any of several types. Both convergent-flow and parallel-flow guns have been successfully used in Estiatrons. The gun shown in Figure 7 is a modified "Pierce" convergent-flow type having a perveance of 1.2 micropervs and a convergence ratio of 4 to 1. The oxide cathode is a concave disk having a conservative current loading of less than 0.075 ampere per square centimeter for beam currents of the order of 40 milliamperes. The gun elements are supported by glass beads, and the entire gun assembly is mounted on a nine-pin glass-button stem which includes the tubulation through which the assembled tube is exhausted.

A mica disk is used to center the drift-tube section of the gun on the axis of the bifilar helices, and to support the electrical connections between the helices and the stem. This disk is a very important component of the tube because proper focusing cannot be obtained unless the drift tube is precisely centered on the axis of the bifilar-helix structure.

The glass envelope must support the bifilar-wound helices in such a manner as to maintain their precise axial alignment and the uniform spacing between adjacent turns. It must also have the smallest possible area of contact with the helices to minimize losses due to dielectric loading. These considerations required the development of entirely new methods for winding and supporting the helices.

The helix-collector portion of the envelope is made of glass tubing and has a Kovar<sup>\*</sup> ring attached to the collector end. The bifilar-helix structure is wound of tungsten wire. After the helix structure is inserted in the envelope, the assembly is placed in a cylindrical furnace and connected to an exhaust system, as shown in Figure 8. While the tube is being evacuated, the helix section of the envelope is heated until the glass softens and shrinks onto the helix structure. This shrinkage bonds the glass to the helix structure and holds it firmly in place.

This envelope-shrinking process must be carefully controlled, with inspection at each point in the process, because penetration of the glass between the helix wires would form a surface within the field of the electron beam during tube operation which could acquire a charge sufficient to interrupt the beam. This interruption could result in collection of electrons by the helix at points near the exposed glass surface, and in burn-out of a helix.

The design of the collector for an electrostatically focused traveling-

---

\* Registered trade mark.

wave tube is more critical than that for a magnetically focused tube because the electrostatically focused beam starts to defocus immediately after it leaves the bifilar-helix region. The Estiatron uses a long, hollow, cylindrical collector, installed immediately adjacent to

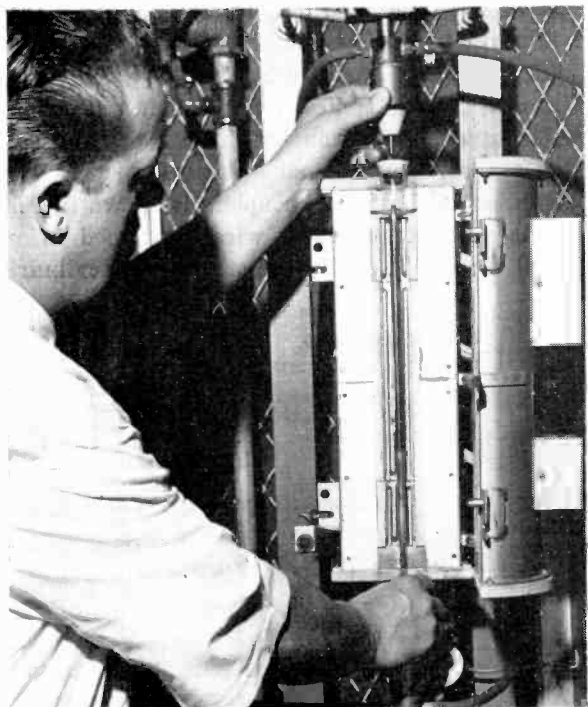


Fig. 8—Furnace used in “envelope-shrinking” operation for bonding helix structure to envelope.

the ends of the helices, to prevent the defocused electron beam from striking the envelope and producing secondary electrons which might be attracted to the helix structure. The radiator is used to facilitate removal of heat from the collector by forced-air cooling.

#### *The Attenuator and Helical Couplers*

The attenuator and helical couplers in the Estiatron are similar to those now used with traveling-wave tubes employing periodic permanent-magnet focus, and present straightforward design problems for bandwidth and insertion loss, rather than fabrication problems.

The attenuator is a bifilar helix wound on a grooved ceramic cylinder three inches long. This attenuator acts as a lossy coupling

between the two coils of the bifilar helix, and is installed in the tube envelope at a point where it provides the desired insertion loss (usually 30 to 50 decibels) between the input and output couplers. This point is approximately one-third of the distance between the input and output couplers.

The design of the input and output couplers for a traveling-wave tube is an important consideration because these couplers have a substantial effect on the bandwidth and the gain-versus-frequency characteristics of the tube. Helical input and output couplers are used in the Estiatron because such couplers have wide-band coupling characteristics and are entirely external to the tube.

The construction of the helical couplers is shown in Figure 9. The coupling helix is a coil of tungsten wire positioned in an internally threaded Teflon<sup>®</sup> sleeve. The coil is installed in a cylindrical housing

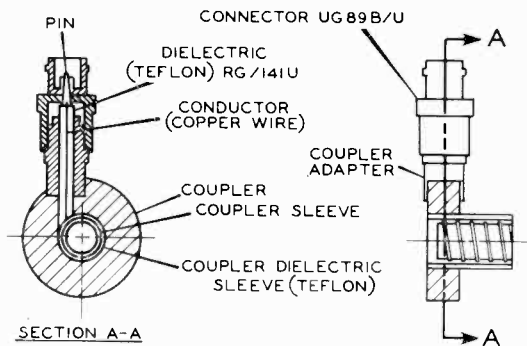


Fig. 9—Helical coupler of the type used with the packaged Estiatron.

and connected by a short coaxial line to an external coaxial connector. The impedance match between these helical couplers and the bifilar helices is such that the voltage standing-wave ratio is less than two over the frequency range from 1500 to 3600 megacycles.

Other methods of coupling, such as direct connection, antenna-to-cavity coupling, and capacitive coupling, may also be used.

#### PERFORMANCE DATA

##### *Typical Operation*

Tests of 50 Estiatrons have provided a substantial amount of information on the performance capabilities of the type and permitted accurate determination of its average characteristics. Table I shows typical operating data and principal characteristics. With forced-air cooling of the collector and helix voltages of approximately 2800 and

\* Registered trade mark.

800 volts, the tube provides a focused beam current of 40 milliamperes with a maximum helix interception of 2 milliamperes, and delivers a power output in excess of 3 watts and a small-signal gain of 25 decibels across the frequency band from 2000 to 3500 megacycles.

Table I—Mechanical Data and Typical Operation of the Packaged Estiatron

*Mechanical*

Mounting Position .....	Any
Cooling .....	10 cfm Forced air at 25° C and 15 psi
Maximum Over-all Length .....	18 inches
Maximum Shell Diameter .....	1½ inches
Collector Connector .....	grounded
RF Connectors:	
Input .....	UG89B/U
Output .....	UG89B/U
Weight .....	2 pounds

*Typical Operating Conditions*

DC Collector Voltage .....	3000 volts
DC Helix Voltage (low) .....	800 volts
DC Helix Voltage (high) .....	2800 volts
DC Drift-Tube Electrode Voltage .....	1200 volts
DC Anode Voltage .....	1300 volts
DC Collector Current .....	40 ma
DC Helix Current (low) .....	0.5 ma
DC Helix Current (high) .....	2.0 ma
DC Drift-Tube Electrode Current .....	0.2 ma
DC Anode Current .....	0.2 ma
Saturated Gain .....	23 db
Low-Level Gain .....	25 db
Power Output across the band .....	3 watts
Midband Power Output .....	5 watts
Heater Voltage (ac or dc) .....	6.3 volts
Heater Current at 6.3 volts .....	1.8 amperes
Maximum Heater Starting Current .....	10 amperes
Cathode Heating Time .....	3 minutes
Frequency Range .....	2000 to 3500 mc
Cold Insertion Loss .....	50 db
Low-Level Gain .....	25 db
Input VSWR (maximum) .....	2 to 1
Output VSWR (maximum) .....	2 to 1
Focusing .....	Electrostatic
Nominal Power Output .....	5 watts
Base Connections .....	Flying leads
Focusing Solenoid .....	None

Figure 10 shows the saturated power output and saturated gain of a typical Estiatron over the frequency band from 2000 to 3600 megacycles. These data were measured with the helix voltages fixed for optimum operation at 3200 megacycles. The saturated power output varies from 3 to 5.4 watts, and the saturated gain from 21 to 30 decibels.

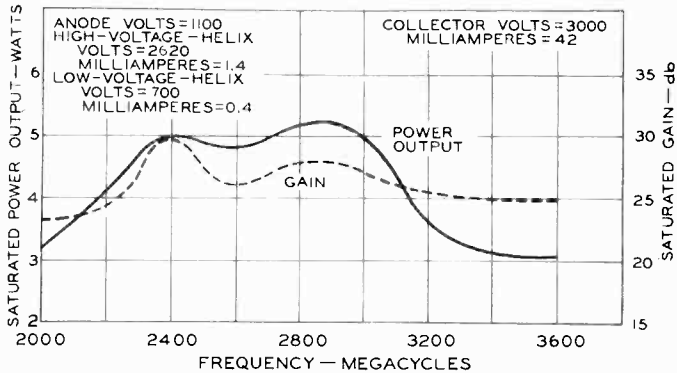


Fig. 10—Saturated power output and gain of a typical Estiatron as functions of frequency over the 2000-to-3600 megacycle band.

The saturated power output at frequencies in the 1800-to-2400-megacycle range is greater than 10 watts for the voltage-optimized conditions. Although the gain at higher frequencies falls off rapidly when helix voltages are optimized for operation at any of these lower frequencies, operation at frequencies as low as 1300 megacycles is practicable. Figure 11 shows the saturated power output and saturated gain over the frequency band from 1300 to 2000 megacycles for a fixed set of operating voltages. The saturated power output is greater than 4 watts and the gain greater than 16 decibels between 1500 and 2000 megacycles.

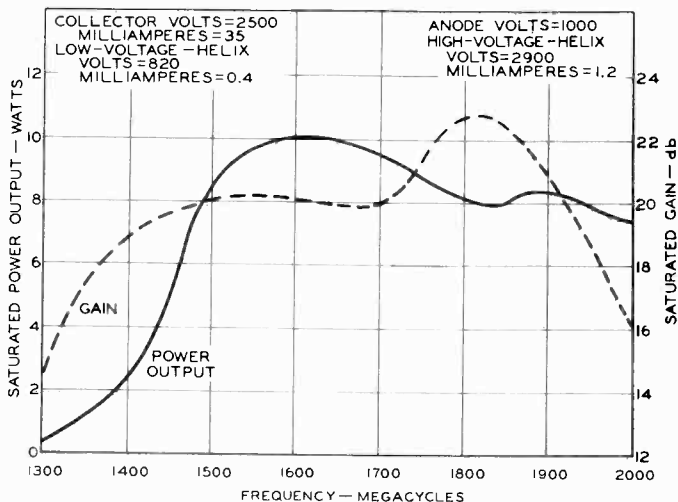


Fig. 11—Saturated power output and gain of a typical Estiatron as functions of frequency over the 1300-to-2000-megacycle band.

*Beam Focus*

Figure 12 shows the currents intercepted by the high-voltage helix and low-voltage helix when the voltage of the high-voltage helix is varied from 3200 volts to 1850 volts and all other parameters are held constant. The low-voltage-helix voltage was 800 volts, the collector voltage 3000 volts, and the beam current 30 milliamperes. No r-f signal was applied, and the synchronous-voltage region of the high-voltage helix was above 2500 volts. It is evident that under these conditions focus is not critically dependent upon helix voltage. For example, the current intercepted by the high-voltage helix is less than 2 milliamperes for all high-voltage-helix voltages above 2300 volts, and the curve for low-voltage-helix interception is substantially flat for high-voltage-helix voltages greater than 2500 volts.

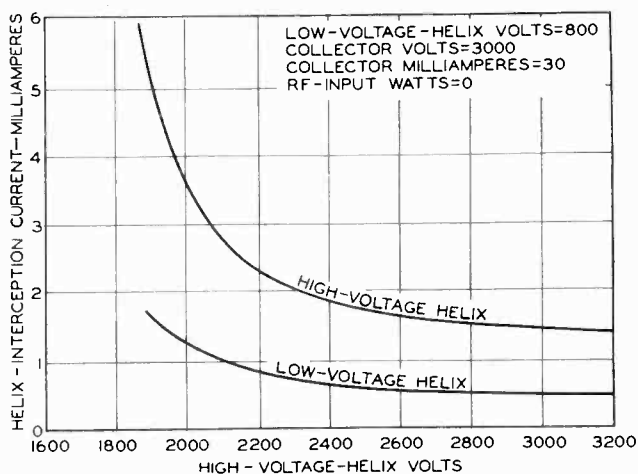


Fig. 12—Helix-interception currents as functions of the voltage applied to the high-voltage helix. Low-voltage-helix currents are negative.

Figure 13 shows the currents intercepted by the high-voltage and low-voltage helices as functions of collector voltage. These currents were measured for an output of 4 watts at a frequency of 3000 megacycles and with no r-f signal applied to the tube. It is evident that interception by the high-voltage helix does not increase appreciably until the collector voltage is depressed below 1800 volts. Current interception is of the same general magnitude with and without r-f signal. The power output of the Estiatron remained substantially constant for collector voltages between 1600 volts and 3000 volts.

The suitability of the Estiatron for operation at very high temperatures was demonstrated by the successful focusing of a typical

tube during exhaust at rated beam current while the tube was heated to temperatures in excess of 400 degrees centigrade.

### Noise Figure and Ion Oscillations

The noise figure of two packaged Estiatrons was measured. The observed values at rated current and power output were of the order of 30 decibels. These values were substantially the same as those observed in traveling-wave tubes using periodic permanent-magnet focus and magnetically shielded convergent-flow guns.

No ion noise was observed in either of two packaged tubes. The lack of ion noise results from the fact that the ions are drained to the helix by the electrostatic focusing action.

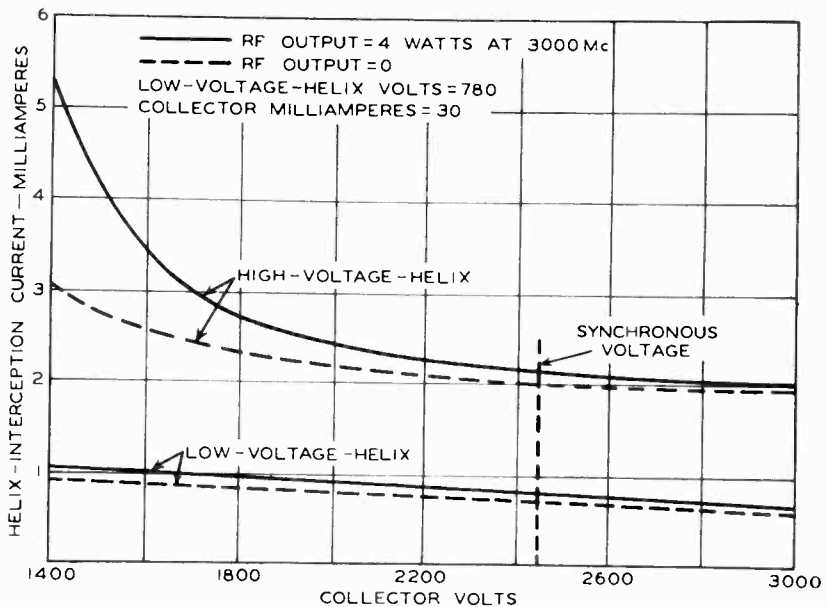


Fig. 13—Helix-interception currents as functions of collector voltage. Low-voltage-helix currents are negative.

### Tube Testing

For all preliminary tests, the tube is removed from its capsule so that the positions of the helical couplers and the attenuator may be adjusted for optimum operation.

Early tests showed that when the d-c voltages for the various elements of the Estiatron were obtained from separate power supplies, the different "snap-on" times of these supplies and the resulting differences in voltage-rise times produced momentary combinations of

voltages capable of damaging the helix structure. This difficulty can be overcome if the anode voltage is maintained at a very low value until the voltages on the two helices have reached the desired values. The anode voltage is then increased until the rated current flows in the collector circuit.

# AN ANALYSIS OF PARAMETRIC AMPLIFICATION IN PERIODICALLY LOADED TRANSMISSION LINES\*†

By

GEORGE H. HEILMEIER

RCA Laboratories,  
Princeton, N. J.

*Summary*—This paper presents a realistic approach to the theory of traveling-wave parametric amplifiers. The propagating structure is considered as a lossless transmission line periodically loaded with nonlinear capacitance in the form of back-biased semiconductor diodes. Analysis of the loaded transmission line indicates the presence of stop and pass-bands instead of the all-pass property of the unloaded line. "Growing" waves at the signal and idle frequencies are produced if the phase and group velocities of the signal, idle, and pump waves are in the same direction. The gain of such a structure is a function of the nonlinearity of the capacitance of the loading diodes, the spacing of the diodes, the characteristic impedance of the unloaded line, the static capacitance of the diode, and the frequencies of operation.

## INTRODUCTION

THE TREMENDOUS recent interest in parametric amplification has resulted from the promise such devices offer as low-noise microwave amplifiers. Most of the experimental results published to date have verified the low-noise capabilities of such devices, but have also shown comparatively narrow bandwidths—a few tenths of one per cent.<sup>1-3</sup> This is due to the fact that they employ sharply tuned resonant circuits to support the three frequencies of interest—the signal, idle, and pump frequencies. Also, the input and output are not inherently separated.

The advantages of a traveling-wave-type parametric amplifier over

---

\* Manuscript received July 2, 1959.

† This work was sponsored in part by the Electronics Research Directorate, Air Force Cambridge Research Center.

<sup>1</sup> H. Heffner and K. L. Kotzbue, "Experimental Characteristics of a Microwave Parametric Amplifier Using a Semiconductor Diode," *Proc. I.R.E.*, Vol. 46, p. 1301, June, 1958.

<sup>2</sup> G. F. Hermann, M. Uenohara and A. Uhler, Jr., "Noise Figure Measurements on Two Types of Variable Reactance Amplifiers Using Semiconductor Diodes," *Proc. I.R.E.*, Vol. 46, p. 1301, June, 1958.

<sup>3</sup> K. K. N. Chang and S. Bloom, "A Parametric Amplifier Using Lower-Frequency Pumping," *Proc. I.R.E.*, Vol. 46, p. 1383, July, 1958.

the resonant circuit types were first disclosed by Cullen.<sup>4</sup> It was reasoned that if the nonlinear reactances could be incorporated as part of a transmission line which propagated the signal, idle, and pump frequencies, extremely broad-band parametric amplification could be obtained. In addition, if the line were properly terminated, separation between input and output would be obtained.

A theoretical analysis of the traveling-wave scheme was carried out by Tien<sup>5</sup> assuming distributed nonlinear reactance. This approach is very artificial in terms of present materials and yields little insight into the problem of realizing such a propagating structure at microwave frequencies. At these frequencies, it becomes impossible to incorporate sufficient diodes per wavelength to approximate a distributed structure with presently available encapsulations.

The purpose of this paper is to present a more realistic approach to the analysis of the traveling-wave parametric amplifier. In this paper, the propagating structure is considered as a lossless transmission line periodically loaded with nonlinear capacitance in the form of back-biased semiconductor diodes. This is the form any traveling-wave parametric amplifier must take with present materials. This analysis yields information about the relationship of diode parameters, spacing, and circuit parameters to the gain and bandwidth of the structure. The results of Tien can be obtained as a special case.

#### ANALYSIS

The traveling-wave parametric amplifier offers an attractive means of obtaining broadband microwave amplification. It employs the nonlinear reactance necessary for parametric amplification as part of a transmission line. If the line is terminated in its characteristic impedance, there is no reflection of the signal, idle, or pump frequencies, and hence isolation between input and output is obtained. The narrow-bandwidth restriction of conventional parametric amplifiers is not a limitation of the traveling-wave scheme because resonant circuits are not employed. The structure to be treated is shown schematically in Figure 1.

The unloaded transmission line is defined by

$$x = \text{unit of length,}$$

$$z = \text{series impedance per unit length,}$$

---

<sup>4</sup> A. L. Cullen, "A Traveling-Wave Parametric Amplifier," *Nature*, Vol. 181, p. 332, February 1, 1958.

<sup>5</sup> P. K. Tien, "Parametric Amplification and Frequency Mixing in Propagating Circuits," *Jour. Appl. Phys.*, Vol. 29, p. 1347, September, 1958.

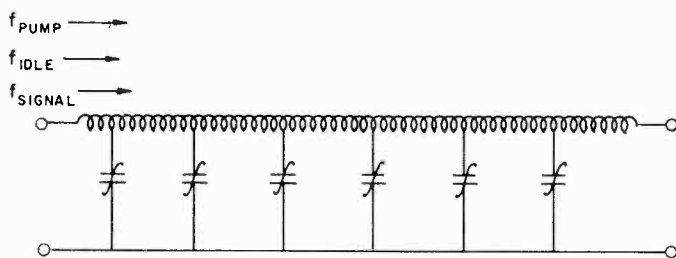


Fig. 1—Uniform transmission line periodically loaded with non-linear capacitance.

$y$  = shunt admittance per unit length,

$Z_0 = \sqrt{z/y}$  = characteristic impedance,

$k = -j\gamma$  = propagation constant of the unloaded line.

This uniform line can be represented by an equivalent- $\pi$  section as shown in Figure 2.

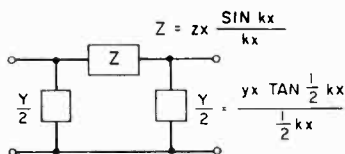
If the loading is in the form of shunt diodes spaced at a distance  $x$  apart, the shunt admittance becomes

$$\frac{Y'}{2} = \frac{Y}{2} + \frac{Y_{\text{diode}}}{2} = \frac{yx \tan(kx/2)}{kx} + \frac{Y_{\text{diode}}}{2}$$

The series impedance remains the same as before. The propagation constant of the uniform line is given by

$$\cos kx = 1 + \frac{ZY}{2}$$

For the loaded line, there will be a new propagation constant  $B$ , defined by



$$\cos kx = 1 + \frac{ZY}{2}$$

$k = -j\gamma$  = PROPAGATION CONSTANT OF UNLOADED LINE

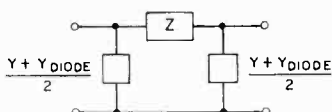
Fig. 2—Transmission line “ $\pi$ ” equivalent.

$$\cos Bx = 1 + \frac{ZY'}{2}$$

When the expressions for  $Z$  and  $Y'$  are substituted in this equation and the relation  $\tan(kx/2) \cong \sin kx / (1 + \cos kx)$  is used, the propagation constant of the loaded line without pumping power,  $B$ , takes the form

$$\cos Bx = \cos kx + \frac{jZ_0}{2} Y_{\text{diode}} \sin kx. \quad (1)$$

The equivalent- $\pi$  section of the loaded line is shown in Figure 3.



$$\cos Bx \approx \cos kx - \frac{\omega C_0 Z_0}{2} \sin kx \quad (Q \gg 1)$$

$B$  = PROPAGATION CONSTANT OF THE UNPUMPED  
LOAD LINE

$x$  = DIODE SPACING

Fig. 3—Transmission line “ $\pi$ ” equivalent with loading.

In general, the admittance of the diode is defined by the current through it and the voltage across it;

$$Y_{\text{diode}} = \frac{i}{v}$$

If the diode has a capacitance  $C$  and a series resistance  $R$ , the diode admittance is

$$Y_{\text{diode}} = \frac{j\omega C}{1 + j\omega CR},$$

and Equation (1) becomes

$$\cos Bx = \cos kx + \left[ \frac{-Z_0 \omega C}{2(1 + j\omega CR)} \right] \sin kx. \quad (2)$$

Equation (2) illustrates the band-pass characteristics of the loaded line. The propagation constant of the loaded line,  $B$ , has a real and imaginary part. Pass bands are defined by a real  $B$ , while imaginary  $B$

implies attenuation and hence a stop band. The plot of Equation (2) assuming high  $Q$  in Figure 4 clearly indicates these regions. The parameter  $\xi$  in these curves is inversely proportional to the diode spacing and directly proportional to the characteristic impedance of the unloaded line and the constant capacitance of the diode. It is a measure of the loading, and the width of the pass bands is seen to decrease with increased  $\xi$ .

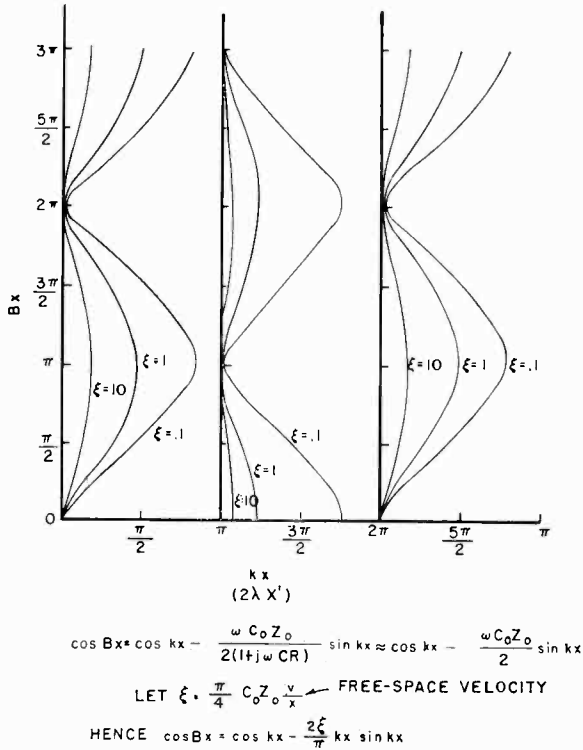


Fig. 4—Propagation constant times diode spacing for loaded line versus propagation constant times diode spacing for unloaded line.

The capacitance of a back-biased semiconductor diode has the form

$$C = C_0 + C_1 V_c$$

if the charge is assumed to be a quadratic function of voltage.

$$C_0 = \text{static capacitance,}$$

$$C_1 = \frac{\text{change in capacitance}}{\text{applied voltage}},$$

$V_C =$  voltage across the capacitance.

If the signal, idle, and pump frequencies ( $\omega_1$ ,  $\omega_2$ ,  $\omega_3$ , respectively) are chosen in the pass bands of a properly designed line, most of the spurious frequencies,  $n\omega_p \pm m\omega_s$ , will fall in the stop bands and hence need not be considered in the analysis. The line is terminated in its approximate characteristic impedance, hence reflected waves also need not be considered.

The current through the diode at the signal frequency,  $\omega_1$ , is given by

$$i_1 = j\omega_1 C_0 V_{C_1} + j\omega_1 C_1 V_{C_3} V_{C_2}^*. \quad (3)$$

Similarly, the current through the diode at the idle frequency,  $\omega_2$ , is

$$i_2^* = -j\omega_2 C_0 V_{C_2}^* - j\omega_2 C_1 V_{C_3}^* V_{C_1}. \quad (4)$$

The total voltage across the diodes at these frequencies is

$$V_1 = i_1 R + V_{C_1},$$

$$V_2^* = i_2^* R + V_{C_2}^*,$$

$$V_3 = V_{C_3} + i_3 R.$$

Combining these relations and ignoring the effects of the  $V_{C_1}$  and  $V_{C_2}$  terms on  $V_{C_3}$ , which neglects signal distortion, Equations (3) and (4) become

$$0 = j\omega_1 C_0 V_1 - (1 + j\omega_1 C_0 R) i_1 + \frac{j\omega_1 C_1 V_3 (V_2^* - i_2^* R)}{1 + j\omega_3 C_0 R}, \quad (5)$$

$$0 = -j\omega_2 C_0 V_2^* - (1 - j\omega_2 C_0 R) i_2^* - \frac{j\omega_2 C_1 V_3^* (V_1 - i_1 R)}{1 - j\omega_3 C_0 R}. \quad (6)$$

The voltages  $V_1$ ,  $V_2$ ,  $V_3$  have the form

$$V_1 = V_{1n} \exp(-jB_1' nx)$$

$$V_2 = V_{2n} \exp(-jB_2' nx)$$

$$V_3 = V_{3n} \exp(-jB_3' nx)$$

where  $B'$  is the propagation constant of the loaded line with pump applied. The node current at each diode has the form of Equation (1) with  $B'$  substituted for  $B$ .

$$i = \frac{2V [\cos B'x - \cos kx]}{jZ_0 \sin kx}.$$

Equations (5) and (6) yield, upon substitution of these relationships,

$$0 = \left[ j\omega_1 C_0 - \frac{2(1 + j\omega_1 C_0 R)}{jZ_0} \left( \frac{\cos B_1'x - \cos k_1x}{\sin k_1x} \right) \right] V_{1n} \exp -j B_1' n x \quad (7)$$

$$+ \frac{j\omega_1 C_1 V_{3n}}{1 + j\omega_3 C_0 R} \left( 1 + 2R \frac{\cos B_2'x - \cos k_2x}{jZ_0 \sin k_2x} \right) V_{2n}^* \exp -j (B_3' - B_2') n x$$

$$0 = - \left[ j\omega_2 C_0 - \frac{2(1 - j\omega_2 C_0 R) (\cos B_2'x - \cos k_2x)}{jZ_0 \sin k_2x} \right] V_{2n}^* \exp j B_2' n x \quad (8)$$

$$- \left[ \frac{j\omega_2 C_1 V_{3n}^*}{1 - j\omega_3 C_0 R} \left( 1 - 2R \frac{\cos B_1'x - \cos k_1x}{jZ_0 \sin k_1x} \right) \right] V_{1n} \exp j (B_3' - B_1') n x.$$

The result of combining these equations is

$$\begin{aligned} & \left[ j\omega_1 C_0 - \frac{2(1 + j\omega_1 C_0 R)}{jZ_0} \frac{\cos B_1'x - \cos k_1x}{\sin k_1x} \right] \left[ j\omega_2 C_0 \right. \\ & \quad \left. - \frac{2(1 - j\omega_2 C_0 R)}{jZ_0} \frac{\cos B_2'x - \cos k_2x}{\sin k_2x} \right] \\ & = \frac{\omega_1 \omega_2 C_1^2 V_3 V_3^*}{1 + \omega_3^2 C_0^2 R^2} \left[ 1 - \frac{2R}{jZ_0} \frac{\cos B_1'x - \cos k_1x}{\sin k_1x} \right] \left[ 1 + \frac{2R}{jZ_0} \frac{\cos B_2'x - \cos k_2x}{\sin k_2x} \right]. \quad (9) \end{aligned}$$

The following conditions on the propagation constants with pump power applied will now be assumed:

$$\begin{aligned} B_1 + B_2 &= B_3 + \delta B_0, \\ B_1' &= B_1 + \delta B, \\ B_2' &= B_2 - (\delta B + \delta B_0). \end{aligned} \quad (10)$$

The change in the propagation constant of the signal wave with pumping power applied is assumed to be small. It is just this small perturbation, however, which makes it possible to obtain gain from such a device.  $\delta B_0$  is the amount by which the sum of the propagation constants of the signal and idle waves differ from the pump wave. Multiplying Equation (9) by

$$\left[ \frac{jZ_0 \sin k_1 x}{1 + j\omega_1 C_0 R} \right] \left[ \frac{jZ_0 \sin k_2 x}{1 - j\omega_2 C_0 R} \right]$$

results in

$$\begin{aligned} & \left[ \frac{-\omega_1 C_0 Z_0 \sin k_1 x}{1 + j\omega_1 C_0 R} - 2(\cos B_1' x - \cos k_1 x) \right] \left[ \frac{-\omega_2 C_0 Z_0 \sin k_2 x}{1 - j\omega_2 C_0 R} \right. \\ & \quad \left. - 2(\cos B_2' x - \cos k_2 x) \right] \\ &= -Z_0^2 \frac{\omega_1 \omega_2 C_1^2 V_3 V_3^*}{1 + \omega_3^2 C_0^2 R^2} \frac{\left( 1 - \frac{2R \cos B_1' x - \cos k_1 x}{jZ_0 \sin k_1 x} \right)}{1 + j\omega_1 C_0 R} \\ & \quad \frac{\left( 1 + \frac{2R \cos B_2' x - \cos k_2 x}{jZ_0 \sin k_2 x} \right)}{1 - j\omega_2 C_0 R} \sin k_1 x \sin k_2 x. \quad (9a) \end{aligned}$$

Now, from Equation (2),

$$2[\cos B_1 x - \cos k_1 x] = \frac{-\omega_1 C_0 Z_0 \sin k_1 x}{1 + j\omega_1 C_0 R}.$$

If the  $Q$  of the diode is much greater than unity,  $\omega RC$  is much less than unity, and

$$1 + j\omega C_0 R \approx 1 - j\omega C_0 R,$$

$$\text{hence} \quad 2[\cos B_2 x - \cos k_2 x] \approx \frac{-\omega_2 C_0 Z_0 \sin k_2 x}{1 - j\omega_2 C_0 R}.$$

Substituting these expressions and those of Equation (10) in Equation (9a), and using the identity

$$\cos x - \cos y \equiv -2 \sin \frac{1}{2} (x + y) \sin \frac{1}{2} (x - y),$$

yields Equation (11).

$$16 \sin \frac{\delta B x}{2} \sin \left( \frac{\delta B + \delta B_0}{2} \right) x \sin \left( B_1 + \frac{\delta B}{2} \right) x \sin \left( B_2 - \frac{\delta B + \delta B_0}{2} \right) x$$

$$= \frac{-Z_0^2 \omega_1 \omega_2 C_1^2 V_3 V_3^*}{1 + \omega_3^2 C_0^2 R^2} \left( \frac{1 - \frac{2R \cos B_1' x - \cos k_1 x}{jZ_0 \sin k_1 x}}{1 + j\omega_1 C_0 R} \right)$$

$$\left( \frac{1 + \frac{2R \cos B_2' x - \cos k_2 x}{jZ_0 \sin k_2 x}}{1 - j\omega_2 C_0 R} \right) \sin k_1 x \sin k_2 x. \quad (11)$$

Normally,  $B_1$  is not near 0 or  $\pi$  which assumes that the edges of the pass bands are not approached. Noting that  $B_1 \gg \delta B$  and  $\delta B x \ll 1$ , and under the assumption of a diode  $Q$  which is much greater than unity, Equation (11) becomes

$$\delta B (\delta B + \delta B_0) x^2 = \frac{-\omega_1 \omega_2}{\omega_3^2} \left| \frac{V_3 C_1}{C_0} \right|^2 \left( \frac{\omega_3 C_0 Z_0}{2} \right)^2 \frac{\sin k_1 x \sin k_2 x}{\sin B_1 x \sin B_2 x} \equiv -M.$$

Solving for  $\delta B$ , one obtains

$$\delta B = -\frac{\delta B_0}{2} \pm j \sqrt{\frac{M}{x^2} - \left( \frac{\delta B_0}{2} \right)^2} = -\frac{\delta B_0}{2} \pm j\alpha. \quad (12)$$

$\alpha$  is defined as the attenuation constant of the pumped, loaded line. It is negative if the group and phase velocities of the signal, idle, and pump waves are in the same direction. The significance of a negative  $\alpha$  is that waves at the signal and idle frequency are not attenuated as is usually the case, but are amplified by the variable-reactance loading.

In the case where the diode spacing,  $x$ , approaches zero, the expression obtained for  $\alpha$  degenerates to the same form as that obtained by Tien for the distributed nonlinear-reactance approach.

The gain parameter of the periodically loaded transmission line may now be examined in more detail. From Equation (12) it is seen that

$$\alpha x = \sqrt{\frac{\omega_1 \omega_2}{\omega_3^2} \Delta^2 \lambda_3^2 \frac{\sin k_1 x \sin k_2 x}{\sin B_1 x \sin B_2 x} - \left( \frac{\delta B_0 x}{2} \right)^2} \quad (12a)$$

where 
$$\Delta \equiv \left| \frac{V_3 C_1}{C_0} \right|, \quad \text{and} \quad \lambda_3 \equiv \frac{\omega_3 C_0 Z_0}{2}.$$

$\Delta$  is a measure of the diode nonlinearity, and  $\lambda_3$  is a measure of the loading at the pump frequency. It is seen that the gain can be increased with greater loading, but at the expense of narrower pass bands. This is evident from Figure 4.

When a high  $Q$  is assumed, Equation (2), which relates the propagation constant of the loaded line to that of the unloaded line, may be written for the frequencies of concern as

$$\begin{aligned} \cos B_1 x &= \cos k_1 x - \frac{\omega_1 C_0 Z_0}{2} \sin k_1 x, \\ \cos B_2 x &= \cos k_2 x - \frac{\omega_2 C_0 Z_0}{2} \sin k_2 x, \\ \cos B_3 x &= \cos k_3 x - \frac{\omega_3 C_0 Z_0}{2} \sin k_3 x. \end{aligned} \tag{13}$$

Defining

$$\begin{aligned} \lambda_1 &= \frac{\omega_1 C_0 Z_0}{2}, \\ \lambda_2 &= \frac{\omega_2 C_0 Z_0}{2}, \\ \lambda_3 &= \frac{\omega_3 C_0 Z_0}{2}, \end{aligned}$$

and

$$\begin{aligned} \theta_1 &= \tan^{-1} \lambda_1, \\ \theta_2 &= \tan^{-1} \lambda_2, \\ \theta_3 &= \tan^{-1} \lambda_3. \end{aligned}$$

equation (13) becomes

$$\begin{aligned} \cos B_1 x &= \sqrt{1 + \lambda_1^2} \cos (k_1 x + \theta_1), \\ \cos B_2 x &= \sqrt{1 + \lambda_2^2} \cos (k_2 x + \theta_2), \\ \cos B_3 x &= \sqrt{1 + \lambda_3^2} \cos (k_3 x + \theta_3). \end{aligned} \tag{13a}$$

Thus, since

$$B_1x + B_2x = B_3x + \delta B_0x, \quad (10)$$

$\delta B_0x$  is expressed in terms of the properties of the line as

$$\begin{aligned} \delta B_0x = & \cos^{-1} [\sqrt{1 + \lambda_1^2} \cos (k_1x + \theta_1)] \\ & + \cos^{-1} [\sqrt{1 + \lambda_2^2} \cos (k_2x + \theta_2)] \\ & - \cos^{-1} [\sqrt{1 + \lambda_3^2} \cos (k_3x + \theta_3)]. \end{aligned} \quad (14)$$

As previously noted,  $\delta B_0$  is a measure of the lack of synchronization

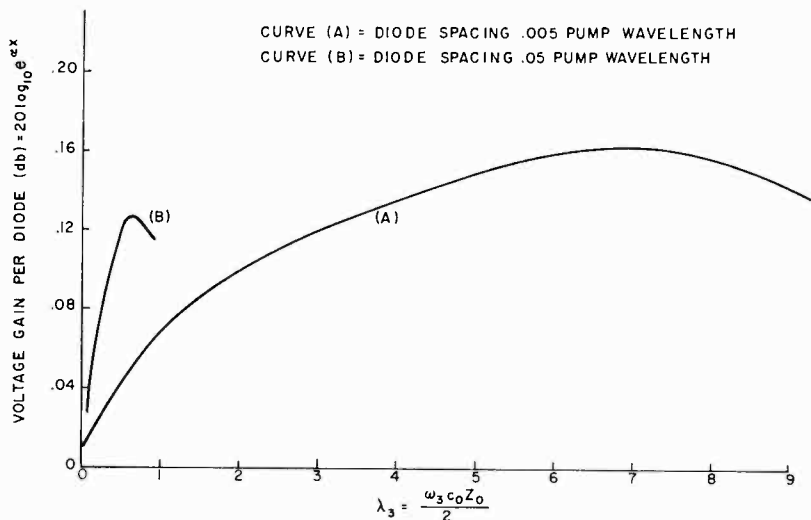


Fig. 5—Voltage gain per diode (db) versus  $\lambda_3$  where  $\omega_1 = 2\omega_2$  and  $\Delta = 0.1$ .

between the signal, idle, and pump waves. It is a factor which reduces the gain. Equation (12a) for the gain parameter becomes, after substitution of Equations (13a) and (14) and normalization,

$$\alpha x = \left[ \frac{\lambda_1 \lambda_2 \Delta^2 \sin 2\lambda_1 x' \sin 2\lambda_2 x'}{\{[1 - (1 + \lambda_1^2) \cos^2 (2\lambda_1 x' + \theta_1)] [1 - (1 + \lambda_2^2) \cos^2 (2\lambda_2 x' + \theta_2)]\}^{1/2}} \left( \frac{\delta B_0 x}{2} \right)^2 \right]^{1/2} \quad (15)$$

where

$$x' = \frac{x}{v C_0 Z_0},$$

$v$  = free-space velocity of propagation.

Figures 5-7 show the voltage gain per diode as a function of  $\lambda_3$ ,  $\lambda_2$

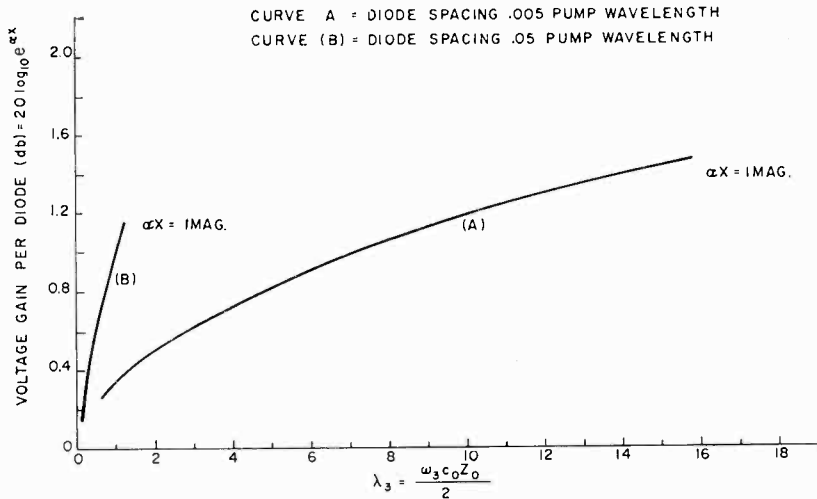


Fig. 6—Voltage gain per diode (db) versus  $\lambda_3$  where  $\omega_1 = 2\omega_2$  and  $\Delta = 0.5$ .

being a measure of the loading at the pump frequency. The normalized diode spacing,  $\Delta$  (a measure of the diode nonlinearity), and the center relation between the signal and idle frequencies are fixed parameters in these curves. The bandwidth is calculated by obtaining the gain for a given center frequency relation and set of parameters from the curve. The bandwidth is then determined from the half power points.

#### CONCLUSION

The bandpass characteristics of the loaded line appear to be useful in that lower losses can result due to the spurious frequencies falling in the stop bands. Caution must be exercised, however, because if high gains are desired from a given number of diodes, the loading of the line must be increased, and, as noted previously, this causes a corresponding decrease in the width of the pass bands and results in narrower bandwidths. It is inferred, therefore, that the bandwidths

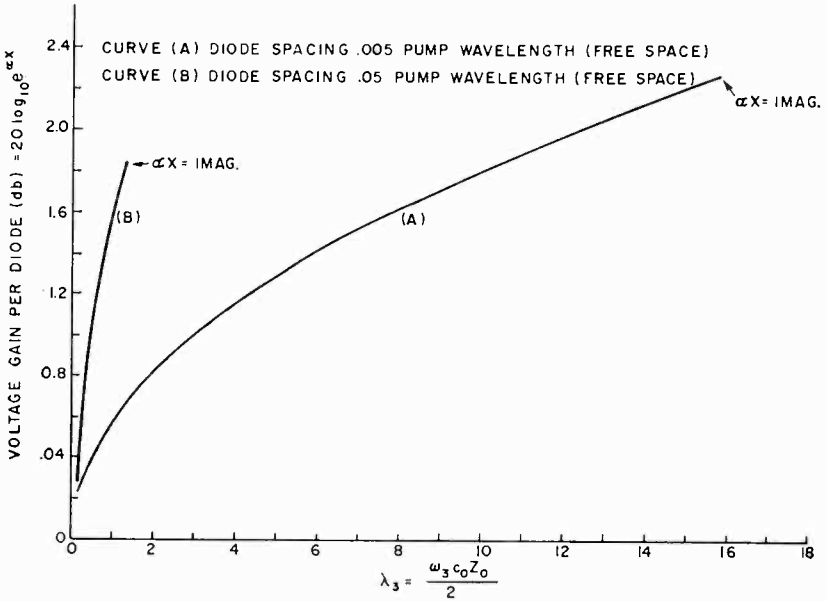


Fig. 7—Voltage gain per diode (db) versus  $\lambda_3$ ; where  $\omega_1 = 2\omega_2$  and  $\Delta = 0.75$ .

obtained at lower frequencies cannot be expected at microwave frequencies with similar numbers of diodes in presently available encapsulations due to the inability to incorporate a sufficient number of diodes per wavelength in the structure.

#### ACKNOWLEDGMENT

The author wishes to express his gratitude to Dr. Kern Chang not only for his assistance, interest, and enthusiastic support of this work, but for his guidance and patience in introducing a novice to the microwave field.

# TRANSIENT CROSS MODULATION IN THE DETECTION OF ASYMMETRIC SIDE BAND SIGNALS\*

BY

T. MURAKAMI† AND R. W. SONNENFELDT‡

*Summary*—A detailed analytical study of transient cross modulation in the detection of multiple-signal asymmetric-sideband systems is presented. Various signal conditions and detection methods are considered. The transient cross talk in both an idealized system and in a practical system is determined. Calculations show that the peak amplitude of the transient cross modulation can be many times as large as the steady-state cross modulation. It is shown that product or synchronous detectors can eliminate the effects of cross modulation.

## INTRODUCTION

IF AN amplitude-modulated wave is transmitted through a network with an asymmetric frequency response about the carrier, the resulting envelope will be distorted.<sup>1-5</sup> The shape of the envelope is a nonlinear function of the depth of modulation. The distortion increases with the depth of modulation and is accompanied by phase modulation of the carrier at the modulation frequency. If there is more than one frequency in the modulation envelope, there may be distortion resulting from intermodulation in the detected output. This distortion is *inherent* in envelope detection of asymmetric sideband signals and is present even when the envelope detector is "ideal," with the output voltage an exact replica of the signal envelope.

This paper presents a study of both envelope and synchronous detection of asymmetric sideband signals so that a comparison of the two

\* Manuscript received June 29, 1959.

† RCA Victor Home Instruments, Camden, N. J.

‡ Formerly, RCA Victor Home Instruments, Camden, N. J.; now, RCA Industrial Electronic Products Division, Camden, N. J.

<sup>1</sup> W. J. Poch and D. W. Epstein, "Partial Suppression of One Sideband in Television Reception," *RCA Review*, Vol. I, p. 19, January, 1937.

<sup>2</sup> P. P. Eckersley, "Asymmetric Sideband Broadcasting," *Proc. I.R.E.*, Vol. 26, p. 1041, September, 1938.

<sup>3</sup> J. M. Hollywood, "Single Sideband Filter Theory with Television Applications," *Proc. I.R.E.*, Vol. 27, p. 457, July, 1939.

<sup>4</sup> R. Urtel, "Observations Regarding Single-Sideband Transmission in Television," *Telefunken Hausmitteilungen*, Vol. 20, pp. 80-83, July, 1939.

<sup>5</sup> S. Goldman, "Television Detail and Selective Sideband Transmission," *Proc. I.R.E.*, Vol. 27, p. 725, November, 1939.

methods of detection as to transient cross modulation can be made. It is shown that synchronous or product detection can be made distortionless for asymmetric sideband signals in this respect.

### CROSS TALK IN ENVELOPE DETECTORS

A basic limitation of the envelope detector is its generation of unwanted cross-talk (cross-modulation) products under certain conditions. This type of distortion occurs when two or more signals are involved in the detection action. When the desired signal is much larger than the others present at the detector, the amount of cross talk is small. As the signals applied to the envelope detector approach each other in magnitude, the amount of cross talk increases.

The cross talk occurs in both the steady and transient states. Thus if two signals are present at the detector, a sudden change in one of them causes a spurious change in the amplitude and phase of the other. This type of distortion will be called transient cross talk distortion to differentiate it from the normal cross talk between two or more steady carriers. A later section shows that the transient cross talk distortion can be many times the steady-state cross talk.

### METHOD OF ANALYSIS

To determine the amount and nature of the cross talk in envelope detectors, the case of two independent amplitude-modulated carriers is considered. One of these carriers can be a subcarrier of the other. Let the selectivity function of the system through which the two signals are transmitted be given by the curves shown in Figure 1(a). These curves depict the amplitude and phase of the system transfer function at the input to the envelope detector at point A in Figure 1(b). It is assumed that there is no cross talk between the two signals in the amplifiers contained within the system transfer function.

The mathematical process involved in the computation of the cross talk consists of finding the envelope of the resultant signal at the detector with one of the signals as the reference.

### TWO-SIGNAL OPERATION OF ENVELOPE DETECTORS

A modulated carrier, after passage through a linear system, can be expressed as

$$\begin{aligned} R(t) &= P(t) \cos [\omega_c t + \theta(\omega_c)] - Q(t) \sin [\omega_c t + \theta(\omega_c)] \quad (1) \\ &= \text{Re} \{ [P(t) + jQ(t)] \exp j[\omega_c t + \theta(\omega_c)] \}, \end{aligned}$$

where  $\text{Re}$  indicates the real part of the quantity.  $P(t)$  is the envelope of the in-phase component and  $Q(t)$  the envelope of the quadrature component. When two such modulated carriers are applied to an envelope detector the total signal is

$$e = \text{Re} \{ [P_1(t) + j Q_1(t)] \exp j(\omega_1 t + \theta_1) + [P_2(t) + j Q_2(t)] \exp j(\omega_2 t + \theta_2) \} \quad (2)$$

where the angular frequencies  $\omega_1$  and  $\omega_2$  are those shown in Figure 1(a) with the corresponding phase angles  $\theta_1$  and  $\theta_2$ .  $P_1(t)$ ,  $Q_1(t)$ ,  $P_2(t)$ , and  $Q_2(t)$  represent the in-phase and quadrature components of either

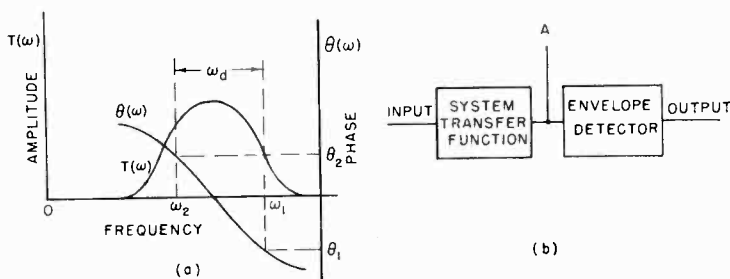


Fig. 1—Relation between signals applied to detector.

the steady-state or transient response of the system to the modulated carriers  $\omega_1$  and  $\omega_2$ , respectively. The detector output will be the envelope of the resultant r-f carrier given in Equation (2) as

$$\begin{aligned} e &= \text{Re} \{ (P_1^2 + Q_1^2)^{1/2} \exp j(\omega_1 t + \theta_1 + \psi_1) + \\ &\quad (P_2^2 + Q_2^2)^{1/2} \exp j(\omega_2 t + \theta_2 + \psi_2) \} \\ &= \text{Re} \{ \exp j(\omega_1 t + \theta_1 + \psi_1) [E_1 + E_2 \exp j(-\omega_d t + \theta_2 - \theta_1 - \psi_1 + \psi_2)] \} \end{aligned} \quad (3)$$

where

$$\begin{aligned} \omega_d &= \omega_1 - \omega_2 \\ E_1 &= (P_1^2 + Q_1^2)^{1/2} \\ E_2 &= (P_2^2 + Q_2^2)^{1/2} \\ \psi_1 &= \tan^{-1} \frac{Q_1}{P_1} \\ \psi_2 &= \tan^{-1} \frac{Q_2}{P_2}, \end{aligned}$$

and where  $P$  and  $Q$  are written for  $P(t)$  and  $Q(t)$ , respectively.

For convenience, let  $\gamma = -\omega_d t + \theta_2 - \theta_1 - \psi_1 + \psi_2$  in Equation (3) so that

$$e = \text{Re} \{ \exp j(\omega_1 t + \theta_1 + \psi_1) | E_1 + E_2 (\cos \gamma + j \sin \gamma) | \}. \quad (4)$$

The envelope of the response is then

$$E = (E_1^2 + E_2^2 + 2E_1E_2 \cos \gamma)^{1/2}. \quad (5)$$

The terms  $E_1$  and  $E_2$  are the envelopes of the individual carriers  $\omega_1$  and  $\omega_2$  after they have passed through the system. The phase modulation on the reference carrier  $\omega_1$  is given the quantity

$$\tan \psi(t) = \frac{E_2 \sin \gamma}{E_1 + E_2 \cos \gamma}. \quad (6)$$

If the right-hand side of Equation (5) is expanded in terms of  $E_1$  and  $E_2$ , the various cross-talk components can be found.

#### DISTORTION AT LIMIT CONDITIONS

Before proceeding with the complete expansion of Equation (5), an analysis of several limiting cases may be of interest.

**Case I:** The modulation  $m_1$  on the reference carrier is small ( $m_1^2 \ll 1$ ) and the amplitude of the second signal is sufficiently small that  $E_2 \ll E_1$ . In this case, the second term within the parenthesis in Equation (5) may be neglected and the square root can be approximated by the first two terms of the binomial expansion. This yields the result

$$E = E_1 \left( 1 + \frac{E_2}{E_1} \cos \gamma \right) \quad (7)$$

For these same conditions ( $m_1^2 \ll 1$ ,  $E_2 \ll E_1$ ),  $Q_1$  and  $\psi_1$  can be neglected. Since the quadrature component  $Q_1$  is a direct function of the modulation  $m_1$ , then  $E_1 = (P_1^2 + Q_1^2)^{1/2} \cong P_1$ . Substituting now the value of  $\gamma = -\omega_d t + \theta_2 - \theta_1 + \psi_2$  in Equation (7) and expanding  $\cos \gamma$  so that  $\psi_2$  is outside the argument, gives the envelope

$$E = P_1 + P_2 \cos (\omega_d t + \theta_1 - \theta_2) + Q_2 \sin (\omega_d t + \theta_1 - \theta_2) \quad (8)$$

since  $P_2 = E_2 \cos \psi_2$  and  $Q_2 = E_2 \sin \psi_2$ .

Equation (8) shows that there is no cross talk; however, there may be quadrature distortion of the second signal due to asymmetrical transmission through the system at frequency  $\omega_2$ . If the percentage modulation  $m_2$  of the second signal is made small compared to unity, the quadrature component  $Q_2$  will be negligible so that ideal detection will be obtained. The method of obtaining  $P_2$  and  $Q_2$  is discussed later.

If  $E_2$  were the desired signal, this would correspond to an adjacent-channel situation where an undesired signal may be much stronger than the desired signal. Equation (8) shows that the output consists of the envelope of the larger signal plus a distorted desired signal. The envelope of the desired signal is modulated at the beat frequency corresponding to the difference between the two carrier frequencies. If the frequency spacing  $\omega_d$  exceeds the normal modulation bandwidth of the system, the desired signal is completely suppressed.

**Case II:**  $E_2 \ll E_1$  but  $m_1^2$  not negligible. Under this condition the second term within the brackets in Equation (5) may again be omitted and the expansion given by Equation (7) used. When this is done and the value of  $\gamma$  substituted, the envelope will be given by

$$E = (P_1^2 + Q_1^2)^{\frac{1}{2}} + (P_2^2 + Q_2^2)^{\frac{1}{2}} \cos (\omega_d t + \theta_1 - \theta_2 + \psi_1 - \psi_2). \quad (9)$$

Since  $Q_1$  and  $Q_2$  are both present, there is quadrature distortion of the signals if the transmission for the corresponding carriers through the system is asymmetrical. In addition, there will be phase modulation of the second signal due to the term  $\psi_1$ . The rate and deviation of this phase modulation is determined by the modulation frequency and percentage  $m_1$  on the first carrier.

**Case III:**  $m_1^2 \ll 1$  and  $E_2$  is of the same order of magnitude as  $E_1$ , but not equal to  $E_1$ . Equation (5) can be expanded as

$$\begin{aligned} E &= \{E_1^2 + E_2^2 + 2E_1E_2 \cos \gamma\}^{\frac{1}{2}} \\ &= \{P_1^2 + Q_1^2 + P_2^2 + Q_2^2 + 2(P_1P_2 + Q_1Q_2) \cos (\omega_d t + \theta_1 - \theta_2) \\ &\quad + 2(P_1Q_2 - P_2Q_1) \sin (\omega_d t + \theta_1 - \theta_2)\}^{\frac{1}{2}}, \quad (10) \end{aligned}$$

since

$$\begin{aligned} \cos \gamma &= (\cos \psi_1 \cos \psi_2 + \sin \psi_1 \sin \psi_2) \cos (\omega_d t + \theta_1 - \theta_2) \\ &\quad + (\cos \psi_1 \sin \psi_2 - \sin \psi_1 \cos \psi_2) \sin (\omega_d t + \theta_1 - \theta_2), \quad (11) \end{aligned}$$

and

$$\begin{aligned} P_1 &= E_1 \cos \psi_1, & Q_1 &= E_1 \sin \psi_1 \\ P_2 &= E_2 \cos \psi_2, & Q_2 &= E_2 \sin \psi_2. \end{aligned} \quad (12)$$

Equation (10) can be better interpreted if the case of a cosine-wave modulated carrier and a steady carrier is considered. For this case,

$$\begin{aligned} P_1 &= V_1 (1 + m_1 \cos \omega_m t), \\ Q_1 &= m_1 V_1 \sin \omega_m t \cong 0, \\ P_2 &= V_2, \\ Q_2 &= 0, \end{aligned} \quad (13)$$

where  $V_1$  and  $V_2$  are relative amplitudes.

When these quantities are substituted into Equation (10), the envelope can be rewritten as

$$\begin{aligned} E &= (V_1^2 + V_2^2 + 2V_1V_2 \cos (\omega_d t + \theta_1 - \theta_2) \\ &\quad + 2m_1V_1 [V_1 + V_2 \cos (\omega_d t + \theta_1 - \theta_2)] \cos \omega_m t \\ &\quad - 2m_1V_1V_2 \sin (\omega_d t + \theta_1 - \theta_2) \sin \omega_m t)^{\frac{1}{2}}, \end{aligned} \quad (14)$$

where the term containing  $m_1^2$  as a factor has been neglected. If Equation (14) is written as

$$\begin{aligned} E &= (V_1^2 + V_2^2 + 2V_1V_2 \cos (\omega_d t + \theta_1 - \theta_2) \\ &\quad + 2m_1V_1 \sqrt{V_1^2 + V_2^2 + 2V_1V_2 \cos (\omega_d t + \theta_1 - \theta_2)} \cos (\omega_m t + \phi))^{\frac{1}{2}} \\ &= \sqrt{V_1^2 + V_2^2 + 2V_1V_2 \cos (\omega_d t + \theta_1 - \theta_2)} \\ &\quad \left\{ 1 + \frac{2m_1V_1 \cos (\omega_m t + \phi)}{V_1^2 + V_2^2 + 2V_1V_2 \cos (\omega_d t + \theta_1 - \theta_2)} \right\}^{\frac{1}{2}}, \end{aligned} \quad (15)$$

where  $V_1 \neq V_2$ , and

$$\phi = \tan^{-1} \frac{V_2 \sin (\omega_d t + \theta_1 - \theta_2)}{V_1 + V_2 \cos (\omega_d t + \theta_1 - \theta_2)}, \quad (16)$$

the envelope can be approximated by the first two terms of the binomial expansion. With this approximation, the detector output is

$$E = \sqrt{V_1^2 + V_2^2 + 2V_1V_2 \cos(\omega_d t + \theta_1 - \theta_2)} + m_1 V_1 \cos(\omega_m t + \phi). \quad (17)$$

The first term in Equation (17) represents the distorted single-sideband envelope of the carrier of angular frequency  $\omega_2$ . The second is an undistorted envelope of the carrier of angular frequency  $\omega_1$  with phase modulation at a rate determined by  $\omega_d$  as given in Equation (16).

Thus, the analysis of the behavior of an envelope detector with respect to a *number* of signals such as must be detected in commercial receivers is very complicated. The detection characteristics depend on the relative modulation depths and signal amplitudes in a rather complex manner. When more than one signal is present at the input terminals to the envelope detector:

1. There will be phase modulation of the weaker signal by the stronger,
2. There will be phase and amplitude modulation of each by the other when both are large,
3. There will be complete suppression of the weaker signal when the other is much larger,
4. There will be distortionless detection only when all other signals are small compared to a desired carrier.

#### EXPANSION OF THE ENVELOPE FUNCTION

When two modulated carriers of frequencies  $\omega_1$  and  $\omega_2$  are transmitted through a linear system, it was shown by Equation (5) that the envelope could be written in the form

$$E = E_1 \left( 1 + \frac{E_2^2}{E_1^2} + 2 \frac{E_2}{E_1} \cos \gamma \right)^{\frac{1}{2}}, \quad (18)$$

where  $E_1 > E_2$ . If  $y = E_2/E_1$ , this equation can be written

$$E = E_1 (1 + y^2 + 2y \cos \gamma)^{\frac{1}{2}}. \quad (19)$$

This function may be expanded as<sup>6</sup>

$$E = E_1 (a_0 + a_1 \cos \gamma + a_2 \cos 2\gamma + \dots) \quad (20)$$

<sup>6</sup> M. S. Corrington, "Frequency Modulation Distortion Caused by Common and Adjacent Channel Interference," *RCA Review*, Vol. VII, p. 522, December, 1946. (Especially pp. 547-548.)

where

$$a_0 = 1 + \frac{y^2}{4} + \frac{y^4}{64} + \frac{y^6}{256} + \frac{25y^8}{16384} + \dots,$$

$$a_1 = y \left( 1 - \frac{y^2}{8} - \frac{y^4}{64} - \frac{5y^6}{1024} - \frac{35y^8}{16384} - \dots \right),$$

$$a_2 = -\frac{y^2}{4} \left( 1 - \frac{y^2}{4} - \frac{5y^4}{128} - \frac{7y^6}{512} - \frac{105y^8}{16384} - \dots \right),$$

In Equation (20) the first term  $a_0 E_1$  represents the envelope of the carrier of frequency  $\omega_1$  after detection. Since  $a_0$  is a function of the modulation on both of the carriers, the term  $a_0 E_1$  will contain the cross talk from the second carrier of frequency  $\omega_2$ . Since the terms  $E_1$  and  $E_2$  represent either transient or steady-state conditions, the cross talk can be either transient or steady state in character.

The distorted in-phase and quadrature components of the envelope of the second carrier can be found by expanding the second term as

$$\begin{aligned} E_1 a_1 \cos \gamma &= E_1 a_1 [\cos \psi_1 \cos (\omega_d t + \theta_1 - \theta_2 - \psi_2) \\ &\quad - \sin \psi_1 \sin (\omega_d t + \theta_1 - \theta_2 - \psi_2)] \\ &= a_1 [P_1 \cos (\omega_d t + \theta_1 - \theta_2 - \psi_2) - Q_1 \sin (\omega_d t + \theta_1 - \theta_2 - \psi_2)]. \end{aligned} \quad (21)$$

The coefficients  $a_1 P_1$  and  $a_1 Q_1$  correspond to the in-phase and quadrature components of the envelope of the carrier of frequency  $\omega_2$ . It is noted that the in-phase and quadrature components of the envelope of the first carrier have been transferred to the corresponding components of the envelope of the second carrier.

#### CROSS TALK IN IDEALIZED SYSTEM

To illustrate the cross talk in the envelope detector, the detection of two carriers of frequencies  $\omega_1$  and  $\omega_2$  after transmission through an idealized bandpass system is considered. In order to simplify the mathematics, the phase shift will be assumed zero for all frequencies. It can be shown that the same result is obtained if a linear phase is assumed except that the time function at the output is shifted by the delay in the linear-phase system. Assume that the amplitude characteristic of the bandpass system is as shown in Figure 2, so

$$\begin{aligned}
 T(\omega) &= 1 \quad \text{for } |\omega| \leq |\omega_a|, \\
 T(\omega) &= 0 \quad \text{for all other values of } \omega.
 \end{aligned}
 \tag{22}$$

Let the amplitude of the carrier of frequency  $\omega_1$  be increased suddenly by amount  $V_1$  so that the driving function is expressed by

$$F(t) = [V_1 \cos \omega_1 t] U(t) + A_1 \cos \omega_1 t,
 \tag{23}$$

where  $A_1$  is the steady carrier amplitude and  $U(t)$  is the unit-step function.

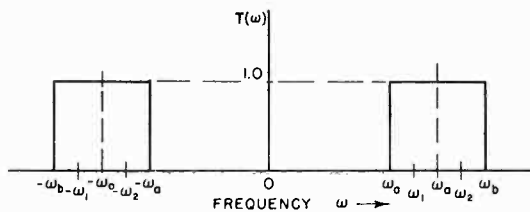


Fig. 2—Amplitude characteristic of ideal bandpass system.

The corresponding Fourier transform of the transient component is given by

$$G(\omega) = \frac{jV_1\omega}{\omega_1^2 - \omega^2}.
 \tag{24}$$

The Fourier integral expression for the transient response of the idealized system to a driving function whose transform is  $G(\omega)$  can be written

$$\begin{aligned}
 R_1(t) &= \frac{1}{2\pi} \int_{-\infty}^{\infty} G(\omega) T(\omega) e^{j\omega t} d\omega \\
 &= \frac{1}{2\pi} \int_{-\omega_b}^{-\omega_a} G(\omega) e^{j\omega t} d\omega + \frac{1}{2\pi} \int_{\omega_a}^{\omega_b} G(\omega) e^{j\omega t} d\omega.
 \end{aligned}
 \tag{25}$$

Letting  $\omega = -\omega'$  in the first integral of Equation (25) and interchanging the limits of integration, the equation may be rewritten as

$$R_1(t) = \frac{1}{2\pi} \int_{\omega_a}^{\omega_b} G(-\omega') e^{-j\omega' t} d\omega' + \frac{1}{2\pi} \int_{\omega_a}^{\omega_b} G(\omega) e^{j\omega t} d\omega$$

$$\begin{aligned}
 &= \frac{1}{2\pi} \int_{\omega_a}^{\omega_b} G(\omega) (e^{j\omega t} - e^{-j\omega t}) d\omega \\
 &= \frac{j}{\pi} \int_{\omega_a}^{\omega_b} G(\omega) \sin \omega t d\omega.
 \end{aligned} \tag{26}$$

since  $\omega'$  may be replaced by  $\omega$  and  $G(-\omega) = -G(\omega)$ . When  $G(\omega)$ , given by Equation (24), is substituted into Equation (26), the response becomes,<sup>7</sup> after addition of the steady-state term,

$$\begin{aligned}
 R(t) &= \frac{V_1}{\pi} \int_{\omega_a}^{\omega_b} \frac{\omega}{\omega^2 - \omega_1^2} \sin \omega t d\omega + A_1 \cos \omega_1 t \\
 &= \frac{V_1}{2} \cos \omega_1 t - \frac{V_1}{2\pi} \sin \omega_1 t \{ \text{Ci} [t(\omega_b + \omega_1)] - \text{Ci} [t(\omega_a + \omega_1)] \\
 &\quad - \text{Ci} [t(\omega_b - \omega_1)] + \text{Ci} [t(\omega_a - \omega_1)] \} \\
 &\quad + \frac{V_1}{2\pi} \cos \omega_1 t \{ \text{Si} [t(\omega_b + \omega_1)] - \text{Si} [t(\omega_a + \omega_1)] \\
 &\quad + \text{Si} [t(\omega_b - \omega_1)] - \text{Si} [t(\omega_a - \omega_1)] \} + A_1 \cos \omega_1 t,
 \end{aligned} \tag{27}$$

where the term  $\frac{1}{2} V_1 \cos \omega_1 t$  is due to the contribution of the residues at the poles at  $\omega = \pm \omega_1$ . The steady-state component is  $A_1 \cos \omega_1 t$ .

If the ratio of the bandwidth to the center frequency of the pass-band,  $\omega_0$ , is small, the terms involving  $\omega_a + \omega_1$  and  $\omega_b + \omega_1$  will cancel, since the corresponding Si and Ci functions will be nearly equal for large arguments. The in-phase and quadrature components of the envelope of the carrier of the carrier of frequency  $\omega_1$  are then

$$P_1(t) = \frac{V_1}{2\pi} \{ \pi + \text{Si} [t(\omega_b - \omega_1)] - \text{Si} [t(\omega_1 - \omega_a)] \} + A_1, \tag{28}$$

and

$$Q_1(t) = \frac{V_1}{2\pi} \{ \text{Ci} [t(\omega_b - \omega_1)] - \text{Ci} [t(\omega_1 - \omega_a)] \}. \tag{29}$$

If the second carrier of frequency  $\omega_2$  is of steady amplitude  $E_2$ , the distorted envelope components of the second carrier are, from Equation (21),

<sup>7</sup> W. Meyer Zur Capellen, *Integraltafeln*, Springer-Verlag, Berlin, Göttingen, Heidelberg, 1950, p. 241, equation 1.5.2.2.

$$\text{in-phase component} = a_1 P_1(t), \tag{30}$$

and

$$\text{quadrature component} = a_1 Q_1(t), \tag{31}$$

where

$$a_1 = y \left( 1 - \frac{y^2}{8} - \frac{y^4}{64} - \frac{5y^6}{1024} - \frac{35y^8}{16384} - \dots \right), \tag{32}$$

and

$$y = \frac{E_2}{[P_1^2(t) + Q_1^2(t)]^{1/2}}. \tag{33}$$

Equations (30) and (31) are plotted in Figure 3 for a normalized bandwidth of 0.1 with  $\omega_a = .95$ ,  $\omega_b = 1.05$ ,  $\omega_1 = 1.03$ , and  $\omega_2 = 0.98$ . In

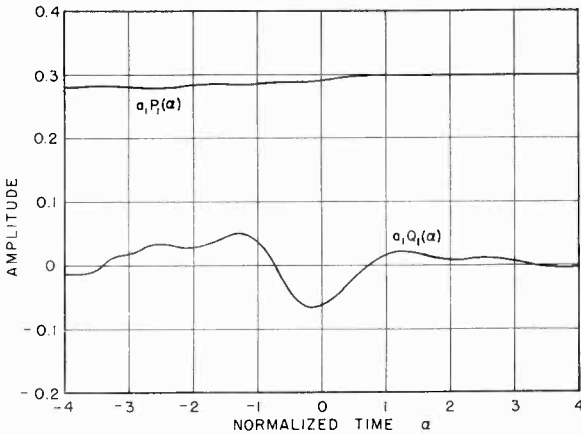


Fig. 3—Transient cross talk in ideal system.

the calculation, the steady carrier amplitude,  $A_1$ , is taken as 0.5, and the jump in carrier amplitude,  $V_1$ , as unity. The steady amplitude  $E_2$  of second carrier is 0.30. Figure 3 shows that a considerable amount of quadrature voltage is produced in the second carrier by the transient change of the first. The change in amplitude of the in-phase component of the second carrier due to transient cross talk is seen to be quite small. The change in the envelope of the second carrier is nearly the same as the change in the in-phase component  $a_1 P_1(\alpha)$  since the maximum quadrature component is about one quarter of the amplitude of the in-phase component. Due to cross talk, the maximum transient

shift in phase of the second carrier is 13 degrees.

Since the phase characteristic has been assumed to be linear for the given amplitude characteristic, the transient begins at time  $t = -\infty$ . In a realizable system, the phase characteristic is usually not linear over the entire passband so that considerably more cross talk between two signals would be produced than in the ideal case described above.

### CROSS TALK IN PRACTICAL SYSTEM

To illustrate the cross talk in the detection process in a practical system, the detection of a vestigial sideband signal with a single-sideband subcarrier is considered. Assume that the curve shape of the system transfer function shown in Figure 4(a) up to the detector at point A in Figure 4(b) can be obtained by a flat-staggered triple-tuned circuit. The step-modulated carrier of frequency  $\omega_c$  is applied vestigially

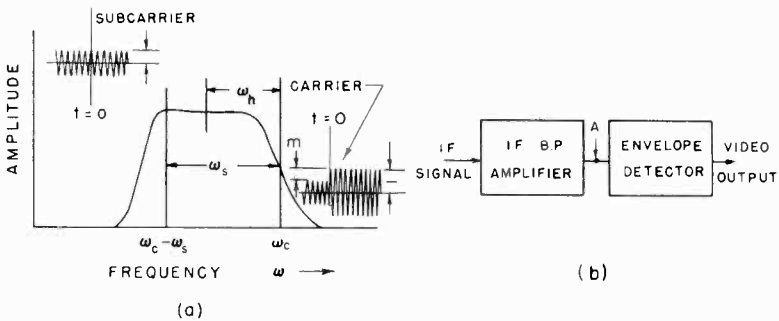


Fig. 4—Relationship between picture and color signals.

in the presence of a single-sideband subcarrier of frequency  $\omega_c - \omega_s$ , as shown in Figure 4(a). The mathematical expression for input to the detector can be written as

$$e = \text{Re} \{ [P(t) + jQ(t)] \exp j(\omega_c t + \theta) + E_2 \exp j[(\omega_c - \omega_s)t + \phi] \}. \quad (34)$$

$P(t)$  and  $Q(t)$  represent the amplitude of the in-phase and quadrature components of the envelope of the step-modulated carrier, and  $E_2$  is the amplitude of the single-sideband subcarrier signal.  $\theta$  and  $\phi$  are the phases of the vestigial-sideband and single-sideband subcarrier signals, respectively, after they have passed through the i-f amplifier. For a modulation of  $m$  per cent and a 3-decibel bandwidth for the

triple-tuned circuit of two units,  $P(t)$  and  $Q(t)$  are given by<sup>8</sup>

$$\begin{aligned} P(t) &= 1 - m (X \cos \omega_h t + Y \sin \omega_h t) && \text{upward modulation} \\ &= 1 - m + m (X \cos \omega_h t + Y \sin \omega_h t) && \text{downward modulation} \end{aligned} \quad (35)$$

$$\begin{aligned} Q(t) &= m (X \sin \omega_h t - Y \cos \omega_h t) && \text{upward modulation} \\ &= -m (X \sin \omega_h t - Y \cos \omega_h t) && \text{downward modulation} \end{aligned} \quad (36)$$

where

$$\begin{aligned} X &= (1 - \omega_h^2) e^{-t} + \frac{1}{\sqrt{3}} (1 - 2\omega_h^2) e^{-t/2} \sin \left( \frac{\sqrt{3}}{2} t - \frac{\pi}{3} \right) \\ &\quad + e^{-t/2} \cos \left( \frac{\sqrt{3}}{2} t - \frac{\pi}{3} \right), \end{aligned} \quad (37)$$

$$\begin{aligned} Y &= \omega_h e^{-t} + \sqrt{3} \omega_h e^{-t/2} \sin \left( \frac{\sqrt{3}}{2} t - \frac{\pi}{3} \right) \\ &\quad + \omega_h e^{-t/2} \cos \left( \frac{\sqrt{3}}{2} t - \frac{\pi}{3} \right), \end{aligned} \quad (38)$$

$\omega_h$  = difference between center frequency of pass band and frequency of 50 per cent response.

The coefficients  $a_1 P(t)$  and  $a_1 Q(t)$  of the general Equation (21) give the amplitudes of the in-phase and quadrature components of the single-sideband subcarrier signal at the output of the envelope detector.

Assume that the vestigial-sideband signal is suddenly changed from an amplitude of 0.3 to 1.0 so that  $m$  is 70 per cent. The assumed value for the subcarrier signal was arbitrarily chosen constant at 0.23 with no associated phase shift other than  $\phi$ , the phase shift through the bandpass system.

The envelope and the in-phase and quadrature components of the response of a flat-staggered triple-tuned circuit to a 70 per cent step-modulated carrier is shown in Figure 5. It is noted from Equation (21) that the quadrature component of the single-sideband subcarrier is directly proportional to the quadrature component  $Q$  developed in the main vestigial-sideband signal. Since a considerable amount of

<sup>8</sup> T. Murakami and R. W. Sonnenfeldt, "Transient Response of Detectors in Symmetric and Asymmetric Sideband Systems," *RCA Review*, Vol. XVI, p. 580, December, 1955. (Equations (60), (61), (70), (71).)

quadrature signal is developed because of the asymmetric sideband transmission as seen in Figure 5, it is evident that some quadrature signal will be produced in the single-sideband channel since the detected output is a beat between the vestigial-sideband carrier and the subcarrier. This distortion in the detected output appears even when the subcarrier is free from distortion.

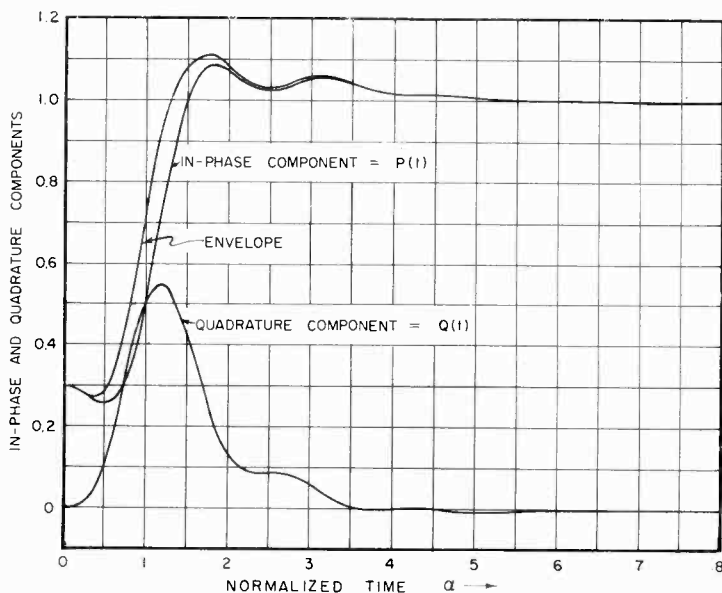


Fig. 5—Envelope of response of flat-staggered triple to suddenly applied sine wave of modulation percentage  $m = 0.70$  at 50 per cent point on selectivity curve (approximate solution).

A plot of the function  $y = E_2 / (P^2 + Q^2)^{1/2}$  as a function of the normalized time  $\alpha$  is shown in Figure 6. This curve shows that the transient cross talk developed in the quadrature channel is of relatively short duration since, as shown by Equation (21), the quadrature component is directly proportional to  $Qy$  in the first approximation. Using the values of  $y$  as given by the curve in Figure 6 in the coefficients  $a_1P(t)$  and  $a_1Q(t)$ , the transient cross-talk components were computed. The components are shown in Figure 7 for the case where the vestigial-sideband signal is modulated upward. The corresponding curves for downward modulation are shown in Figure 8. These curves show that considerable transient cross talk is introduced into the subcarrier channel when the vestigial-sideband carrier is step modulated, since the quadrature distortion of the vestigial-sideband signal is transferred to the detected subcarrier output.

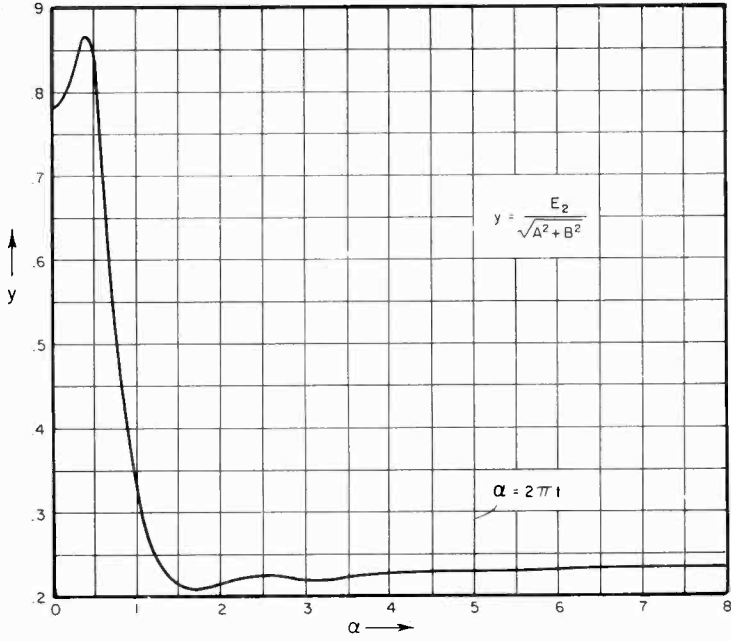


Fig. 6—Value of  $y$  as a function of  $\alpha$ .

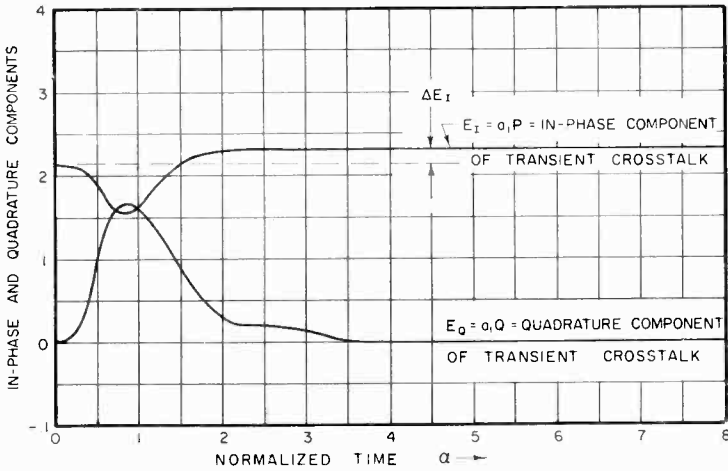


Fig. 7—Transient cross talk of  $E_1$  into subcarrier channel for upward modulation of  $E_1$ .

The steady-state change caused by cross talk is denoted by the amount  $\Delta E_I$  indicated in Figures 7 and 8. The steady-state cross talk is very much smaller than the transient cross talk. The transient cross talk can be reduced in amplitude and increased in length time-wise if the  $a_1 P(t)$  and  $a_1 Q(t)$  signals are low-passed after demodulation.

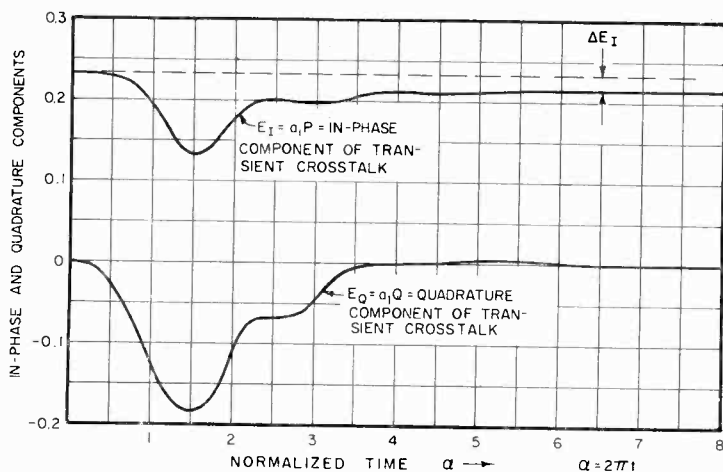


Fig. 8—Transient cross talk of  $E_I$  into subcarrier channel for downward modulation of  $E_I$ .

#### ELIMINATION OF CROSS TALK BY PRODUCT DETECTION

The transient cross-talk effects associated with envelope detectors can be eliminated by use of synchronous or product-type detectors. The essential property of detectors needed to eliminate cross modulation products other than the desired modulation components is that they produce an output that is linearly related to the modulation on the input carrier. This means that such detectors detect  $P(t)$  or  $Q(t)$  or linear combinations of the in-phase and quadrature components.

Assume again that two modulated carriers are present at the input to the detector. These may be written as

$$e = P_1(t) \cos(\omega_1 t + \theta_1) + Q_1(t) \sin(\omega_1 t + \theta_1) + P_2(t) \cos(\omega_2 t + \theta_2) + Q_2(t) \sin(\omega_2 t + \theta_2), \quad (39)$$

If, in addition, there is a reference voltage input to the detector

$$e_1 = \cos(\omega_1 t + \theta_1), \quad (40)$$

a product detector will form the product

$$\begin{aligned}
 ee_1 &= [P_1(t) \cos(\omega_1 t + \theta_1) + Q_1(t) \sin(\omega_1 t + \theta_1)] \cos(\omega_1 t + \theta_1) \\
 &\quad + [P_2(t) \cos(\omega_2 t + \theta_2) + Q_2(t) \sin(\omega_2 t + \theta_2)] \cos(\omega_1 t + \theta_1) \\
 &= P_1(t) \cos^2(\omega_1 t + \theta_1) + Q_1(t) \sin(\omega_1 t + \theta_1) \cos(\omega_1 t + \theta_1) \\
 &\quad + P_2(t) \cos(\omega_2 t + \theta_2) \cos(\omega_1 t + \theta_1) \\
 &\quad\quad\quad + Q_2(t) \sin(\omega_2 t + \theta_2) \cos(\omega_1 t + \theta_1) \\
 &= \frac{1}{2} P_1(t) [1 + \cos 2(\omega_1 t + \theta_1)] + \frac{1}{2} Q_1(t) \sin 2(\omega_1 t + \theta_1) \\
 &\quad + \frac{1}{2} P_2(t) \{ \cos [(\omega_1 + \omega_2) t + \theta_1 + \theta_2] \\
 &\quad\quad\quad + \cos [(\omega_1 - \omega_2) t + \theta_1 - \theta_2] \} \\
 &\quad + \frac{1}{2} Q_2(t) \{ \sin [(\omega_1 + \omega_2) t + \theta_1 + \theta_2] \\
 &\quad\quad\quad - \sin [(\omega_1 - \omega_2) t + \theta_1 - \theta_2] \}. \quad (41)
 \end{aligned}$$

After the second-harmonic terms and the terms of frequency  $(\omega_1 + \omega_2)$  are filtered out, there remain the lower frequency terms

$$\begin{aligned}
 e_0 &= \text{low-frequency components of } (ee_1) \\
 &= \frac{1}{2} P_1(t) + \frac{1}{2} P_2(t) \cos [(\omega_1 - \omega_2) t + \theta_1 - \theta_2] \\
 &\quad - \frac{1}{2} Q_2(t) \sin [(\omega_1 - \omega_2) t + \theta_1 - \theta_2]. \quad (42)
 \end{aligned}$$

When the modulation frequency components in  $P_1(t)$  are sufficiently less than the frequency  $(\omega_1 - \omega_2)$ , the modulation on the first carrier may be obtained by filtering. The quadrature component  $Q_1(t)$  may be obtained in a similar manner if the voltage  $e$  is multiplied by a reference voltage  $e_1 = \sin(\omega_1 t + \theta_1)$ . If the signal represented by Equation (42) is passed through a bandpass system and product detected by multiplication by

$$e_2 = \cos [(\omega_1 - \omega_2) t + \theta_1 - \theta_2], \quad (43)$$

the in-phase component  $P_2(t)$  results after transmission through the appropriate low-pass system. The quadrature component  $Q_2(t)$  may be obtained by multiplication by the corresponding sine function.

The preceding results show that a product or synchronous detector produces no cross talk regardless of how many signals are present and irrespective of their relative amplitudes.

## CONCLUSIONS

Detectors with output proportional to the envelope of a signal will have distortion and cross talk in the output voltage. If nonlinear distortion and cross talk are to be eliminated in the detection of asymmetric sideband signals, it is convenient to use a synchronous (or product) detector. It has been shown that such detectors will, under conditions of proper phasing, detect the envelope of the in-phase component rather than the envelope of a modulated signal. The in-phase component is free from the nonlinear distortion and cross-talk effects associated with the carrier envelope.

The envelope distortion and cross talk have both transient and steady-state effects, and these transient effects may have peak values many times larger than the steady-state values. Again, where these transient effects are important, they may be eliminated by use of a synchronous detector.

# VOLTAGE SENSITIVITY OF LOCAL OSCILLATORS\*

BY

WEN YUAN PAN

RCA Victor Home Instruments,  
Camden, N. J.

*Summary*—The dependence of the oscillation frequency on certain operating conditions is discussed and defined mathematically in terms of independent variables. The effects of variations in plate and heater voltages on the oscillation frequency are essentially independent of each other. Furthermore, the voltage and warm-up temperature sensitivities of local oscillators are similar in characteristics. These observations suggest an approach to the problem of oscillator stability. When the operating voltages are varied, the oscillation frequency generally exhibits an instantaneous deviation followed by a relatively slow drift. The oscillation device and frequency, circuit configuration, and oscillation strength all have important effects on the voltage sensitivity in most practical local oscillators.

## INTRODUCTION

THE FREQUENCY of an oscillator, even when the active device is assumed to have linear characteristics, differs from the frequency determined by the reactance components of the oscillation circuit alone.<sup>1</sup> In almost all practical local oscillators, particularly at very high and ultra high frequencies, any change of the operating conditions of the active device produces frequency deviations.

Since there are several parameters of a local oscillator which are dependent on certain operating conditions such as the supply voltages, it is quite difficult to ascertain the effect of a change in any one operating condition. However, if an operating condition could be expressed mathematically in terms of independent variables, it would be relatively simple to predict the consequences of a change in that condition. This paper discusses the dependence of the oscillation frequency on the operating conditions and attempts to define such dependence mathematically in terms of independent variables.

## PRINCIPAL FACTORS AFFECTING OSCILLATION FREQUENCY

In conventional local oscillators using vacuum tubes, such as the Colpitts circuit of Figure 1, the oscillation frequency,  $f$ , is a function

\* Manuscript received May 1, 1959.

<sup>1</sup> H. A. Thomas, *Theory and Design of Valve Oscillators*, Chapman & Hall, Ltd., London, England, 1939.

of the circuit inductance,  $L$ , and capacitance,  $C$ , and the operating resistances,  $r_p$ ,  $r_g$ ,  $r_k$ , looking into the plate, grid, and cathode of the tube, respectively,<sup>2</sup> or

$$f = F(L, C, r_p, r_g, r_k). \quad (1)$$

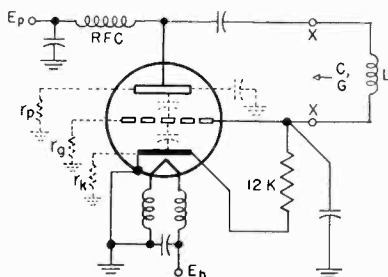


Fig. 1—Conventional local oscillator for 250 megacycles.

There are at least four principal factors which affect  $f$ :

- (1) The changes of electrode conductances resulting from varying operating voltages;
- (2) The changes of electrode capacitances due to temperature effects and variation of operating voltages;
- (3) The changes of harmonic amplitudes due to the nonlinearity of the tube characteristics which also depend upon the operating voltages and other conditions; and
- (4) The changes of component values, predominantly on account of temperature rises.

Generally, the effects of these changes on the oscillation frequency are substantially greater than can be deduced from a simple linear theory. Therefore, a practical approach is warranted which takes into consideration two chief causes of frequency instability—changes in operating voltages and rises in temperature.

Experiments and analysis reveal that these two changes are closely related. A solution to the voltage sensitivity problem generally implies a solution to the temperature problem in most applications. For this reason, a study has been made of the frequency characteristics of a very-high-frequency local oscillator under the conditions of varying

<sup>2</sup> H. Jefferson, "Stabilization of Feedback Oscillators," *Wireless Engineer*, Vol. XXII, p. 384, August, 1945.

plate or heater voltage,  $E$ . The corresponding deviations of oscillation frequency can be determined from Equation (2);

$$\frac{1}{f} \frac{\Delta f}{\Delta E} = k_1 \left( 1 - \frac{1}{\omega^2 LC} \right) \left( \frac{\Delta C}{\Delta E} \right) \left( \frac{1}{r_p} \frac{\Delta r_p}{\Delta E} + \frac{1}{r_g} \frac{\Delta r_g}{\Delta E} + \frac{1}{r_k} \frac{\Delta r_k}{\Delta E} \right). \quad (2)$$

#### EFFECT OF VARYING PLATE VOLTAGE

When the plate voltage,  $E_p$ , is varied while the heater voltage,  $E_h$ , and other conditions remain the same, the oscillation frequency deviates according to Equation (2). The deviation consists of an instantaneous component followed by a relatively slow-acting component. The instantaneous component results from the two following effects:

- (1) The operating conductances quickly assume different values.
- (2) The effective capacitance,  $C$ , also changes instantly, because any variation of operating voltages alters cathode emission and electron velocity, and, therefore, the space-charge condition around the cathode. A change of harmonic amplitudes takes place immediately after the variation of plate voltage.

The relatively slow-acting component results from the difference in plate dissipation,  $\Delta E_p I_p$ , which causes temperature rises at the tube electrodes and, hence, influences the oscillation frequency.

#### Graphical Representation

Both the instantaneous and slow-acting components are illustrated in Figure 2. Initially, the local oscillator was stabilized at 250 megacycles under controlled conditions. At  $t = 0$ ,  $E_p$  was instantly raised from 50 to 60 volts for a period of 10 minutes and then was brought back instantly to 50 volts. The frequency deviations,  $\Delta f_1$ , resulting from  $+\Delta E_p$  and  $-\Delta E_p$  are approximately, but not exactly, identical.

#### Mathematical Solution

The frequency deviation resulting from  $\Delta E_p$ , shown in Figure 2, can be expressed as

$$\Delta f_1 = \alpha_p - \alpha_1 (1 - e^{-\beta_1 t}) \quad (3)$$

where  $\alpha_p$ ,  $\alpha_1$ , and  $\beta_1$  are constants for a given oscillator under a given operating condition, and

$\alpha_p$  = magnitude of the instantaneous shift of the oscillator frequency,

$\alpha_1$  = maximum magnitude of the relatively slow drift of the oscillator frequency,

$\beta_1$  = rate at which the oscillator frequency deviates following the instantaneous frequency shift.

In this particular example, the oscillation frequency increased 40 kilocycles immediately after  $E_p$  was raised from 50 to 60 volts, then

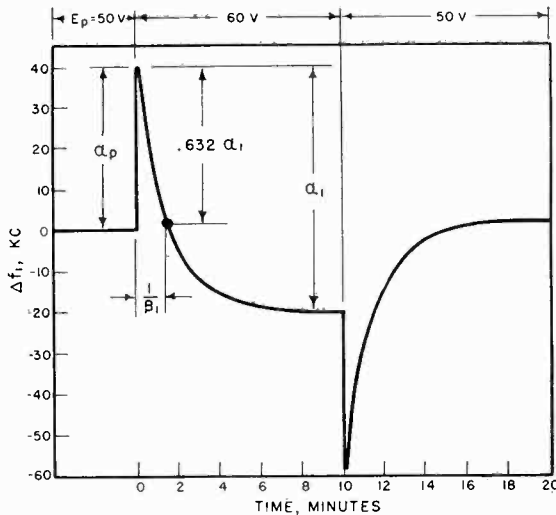


Fig. 2—Frequency deviations due to varying plate voltage.

decreased gradually approximately 60 kilocycles. However, these numerical values may differ drastically in other local oscillators or under different operating conditions. To obtain a generalized knowledge of the effect of  $\Delta E_p$  on  $f_1$ , some characteristics of these three constants were studied.

For a given percentage change of plate voltage,  $\alpha_p$  is smaller in a stronger oscillator. The dotted curve shown in Figure 3 is a plot of the grid excitation,  $E_g$ , of the 250-megacycle oscillator at different values of  $E_p$ . In this case,  $E_g$  is an approximate measure of the oscillation strength; the oscillation is stronger at higher plate voltages. The quantity  $\Delta \alpha_p / \Delta E_p$ , which is the slope of the  $\alpha_p$  curve, diminishes as the amplitude of oscillation increases. This phenomenon is consistent with the fact that the quantities

$$\left| \frac{\Delta C}{\Delta E_p} \right|_{t \rightarrow 0} \quad \text{and} \quad \left| \frac{1}{r_x} \frac{\Delta r_x}{\Delta E_p} \right|,$$

where  $x$  denotes the tube electrode of interest, are small where the oscillation is strong. Apparently, the effect of harmonics on the oscillation frequency is relatively insignificant in this local oscillator. The results might have been different, however, if a lower  $Q$  oscillatory tank circuit and an oscillation tube having more nonlinear characteristics were used.

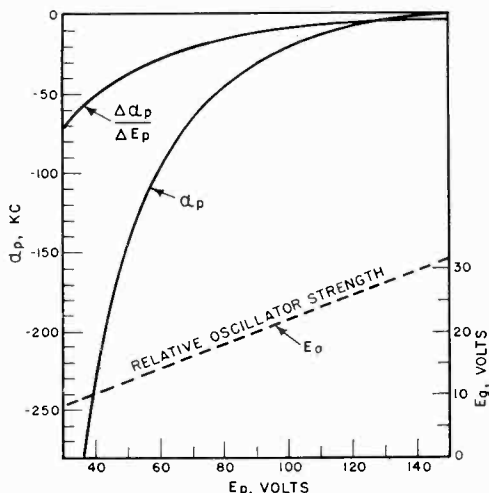


Fig. 3—Dependence of  $\alpha_p$  and  $\Delta\alpha_p/\Delta E_p$  on oscillation strength.

An examination of the  $\alpha_p$  curve in Figure 3 suggests that a fairly strong oscillation is desirable for minimum instantaneous voltage sensitivity. In addition, a proper selection of oscillation tube and component values may further reduce this quantity.

The constant  $\alpha_1$  is determined by the change of plate dissipation,  $\Delta E_p I_p$ , due to  $\Delta E_p$ . The change of plate dissipation is instantaneous but its effect on oscillation frequency follows the general law of heat radiation and conduction.<sup>3</sup> In most conventional vacuum tubes,

$$\alpha_1 = k_2 \Delta E_p I_p, \tag{4}$$

where  $k_2$  depends upon the oscillation circuit, tube, and frequency. Generally, the magnitude of  $\alpha_1$  is independent of the rate of change

<sup>3</sup> W. Y. Pan, "Frequency Characteristics of Local Oscillators," *RCA Review*, Vol. XVI, p. 379, September, 1955.

of the plate dissipation. An abrupt change of  $E_p$  would yield the same  $\alpha_1$  value as a gradual change of  $E_p$  if  $\Delta E_p I_p$  were the same in both cases.

To assure low  $\alpha_1$  for a given percentage change of  $E_p$ , a weak oscillation is desirable because the corresponding  $\Delta E_p I_p$  is small. This condition is contradictory to that required for low  $\alpha_p$ , and therefore a compromise strength of oscillation has to be reached unless either  $\alpha_p$  or  $\alpha_1$  can be compensated by circuit elements.

The time constant,  $\beta_1$ , depends largely upon the construction of the tube. It is virtually independent of the oscillation frequency and circuit, and operating conditions.

#### EFFECT OF VARYING HEATER VOLTAGE

When the heater voltage varies and the plate voltage and other operating conditions remain the same, the oscillation frequency deviates according to Equation (2). The frequency deviations ( $\Delta f_2$ ) caused by

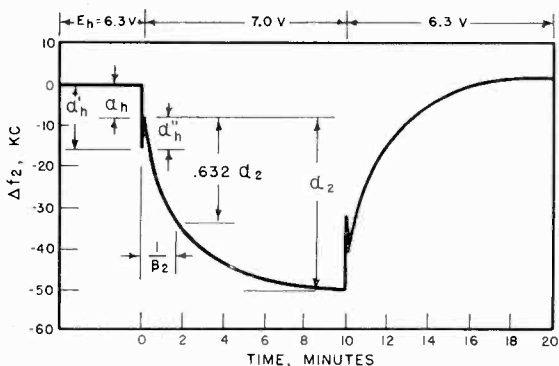


Fig. 4—Frequency deviations due to varying heater voltage.

variation of the heater voltage are shown in Figure 4. The plate voltage was kept at 60 volts, but the heater voltage was raised from 6.3 to 7.0 volts for a period of 10 minutes and then brought back to 6.3 volts. The curve is similar to that in Figure 2 except for the rapid frequency gyration ( $-\alpha'_h + \alpha''_h$ ) at the instant of changing  $E_h$ .

#### Complete Solution

Mathematically, the frequency deviations  $\Delta f_2$  can again be expressed in a simple form,

$$\Delta f_2 = -\alpha'_h + \alpha''_h - \alpha_2(1 - e^{-\beta_2 t}). \quad (5)$$

This differs from Equation (3) for  $\Delta f_1$  by the addition of the term

$\alpha''_h$ . By neglecting the slight difference in time constants,  $(-\alpha'_h + \alpha''_h)$  of Equation (5) is analogous to  $\alpha_p$  of Equation (3). Both are formed by the changing conductances and effective capacitance of the tube and the changing harmonic amplitudes, but their relative effects on  $\Delta f_1$  and  $\Delta f_2$  are appreciably different. In the case of  $\Delta f_1$ , the term  $(1/r_k)(\Delta r_k/\Delta E_p)$ , which exhibits a somewhat longer time constant, fails to contribute materially to  $\alpha_p$ , where  $r_k$  is principally the cathode interface resistance of the oscillation tube.<sup>4</sup> On the other hand, this term becomes dominant in the case of  $\Delta f_2$  for the local oscillator shown by Figure 1 at 250 megacycles.

To substantiate this explanation, the magnitude of  $\alpha''_h$  has been investigated first at 250 megacycles for a large number of tubes of the same type and then at oscillation frequencies ranging from 100 to 1000 megacycles for the same tube. The values of  $\alpha''_h$  under these conditions ranged from 0 to a magnitude many times greater than  $\alpha'_h$ . When a resistor of 1800 ohms was connected between ground and cathode of the oscillator tube,  $\alpha''_h$  was reduced to an insignificant value in all cases. Accordingly, the cathode interface resistance of the tube is probably responsible for  $\alpha''_h$  in Equation (5).

#### *Simplified Solution*

The exact cause of  $\alpha''_h$  is not pursued further because in many applications such as television receivers, any instantaneous shift of oscillation frequency may not be detrimental to the receiver function provided the oscillation frequency returns quickly to its original value. For this reason, it is more convenient to simplify Equation (5) by letting

$$\alpha_h = -\alpha'_h + \alpha''_h. \quad (6)$$

Thus, 
$$\Delta f_2 = \alpha_h - \alpha_2 (1 - e^{-\beta_2 t}), \quad (7)$$

Now the expression for  $\Delta f_2$  resulting from  $\Delta E_h$  is similar to that for  $\Delta f_1$  resulting from  $\Delta E_p$ . The constants  $\alpha_h$  and  $\beta_2$  possess essentially the same characteristics as  $\alpha_p$  and  $\beta_1$  of Equation (3), respectively, except that  $\alpha_h$  is less dependent upon the oscillation strength.

The chief dissimilarity between  $\Delta f_1$  and  $\Delta f_2$  lies in the remaining constant.  $\alpha_1$  of  $\Delta f_1$  is proportional to  $\Delta E_p I_p$ , whereas  $\alpha_2$  of  $\Delta f_2$  is proportional to the change of heater power ( $\Delta E_h I_h$ ), or

$$\alpha_2 = k_3 \Delta E_h I_h, \quad (8)$$

<sup>4</sup> L. S. Nergaard and R. W. Matheson, "Study of the Interface Layer in Oxide Cathodes," *RCA Review*, Vol. XV, p. 335, September, 1954.

where  $k_3$  is a direct function of the frequency and is dependent on the construction of the tube.

#### SIMULTANEOUS CHANGES IN PLATE AND HEATER VOLTAGES

The frequency deviations  $\Delta f_1$  and  $\Delta f_2$  are virtually independent of each other. When both  $E_p$  and  $E_h$  are varied simultaneously, the overall frequency deviation ( $\Delta f$ ) becomes

$$\Delta f = \Delta f_1 + \Delta f_2. \quad (9)$$

The dashed and dotted curves of Figure 5 are reproduced from Figures 2 and 4 showing  $\Delta f_1$  and  $\Delta f_2$ , respectively. The solid curve, which was

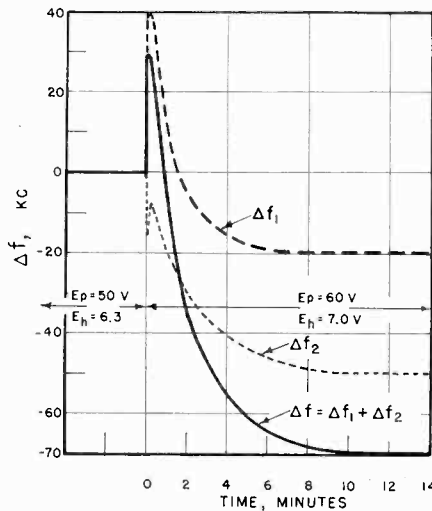


Fig. 5—Frequency deviations due to varying plate and heater voltages simultaneously.

obtained by simultaneously raising  $E_p$  from 50 to 60 volts and  $E_h$  from 6.3 to 7.0 volts, demonstrates the relationship indicated in Equation (9). Because of this relationship, the problem of stabilization for variations of operating voltages is greatly simplified, and  $\Delta f_1$  and  $\Delta f_2$  can be dealt with individually.

#### STABILIZATION CONSIDERATIONS

According to Equations (3), (7), and (9), there are six quantities which affect  $\Delta f$  when the operating voltages are varied simultaneously:  $\alpha_p$ ,  $\alpha_1$ ,  $\beta_1$ ,  $\alpha_h$ ,  $\alpha_2$ , and  $\beta_2$ . These six quantities can be divided into

three groups: (1) the fast-acting quantities  $\alpha_p$  and  $\alpha_h$ ; (2) the relatively slow-acting quantities  $\alpha_1$  and  $\alpha_2$ ; and (3) the quantities  $\beta_1$  and  $\beta_2$  which are substantially independent of operating conditions.

$\alpha_p$  and  $\alpha_h$

In contrast to  $\alpha_p$ ,  $\alpha_h$  is less dependent on the oscillation strength and is usually negative with increasing  $E_h$  in conventional tubes. Therefore, advantage can be taken in the design of local oscillators by making

$$\alpha_p + \alpha_h = 0. \quad (10)$$

This condition can be satisfied with considerable variations of  $E_p$  and  $E_h$  provided certain requirements are fulfilled. Since

$$\alpha_p = K_1 \frac{\Delta E_p}{E_p},$$

$$\alpha_h = K_2 \frac{\Delta E_h}{E_h},$$

$\alpha_p$  and  $\alpha_h$  may be expressed in terms of the changes of the line voltage,  $E_L$ . In a given receiver design,

$$\frac{\Delta E_p}{E_p} = K_3 \frac{\Delta E_L}{E_L},$$

$$\frac{\Delta E_h}{E_h} = K_4 \frac{\Delta E_L}{E_L}.$$

Consequently, Equation (10) prevails for any reasonable  $\Delta E_L/E_L$ , if

$$K_1 K_3 = K_2 K_4. \quad (11)$$

The constants  $K_3$  and  $K_4$  are determined by the over-all receiver design, whereas the relative magnitudes of  $K_1$  and  $K_2$  depend upon the choice of tube, circuit configuration, and oscillation strength. In the case where  $K_2$ ,  $K_3$ , and  $K_4$  are all fixed values, the only freedom available to the receiver designer is the adjustment of the oscillation strength in order to satisfy Equation (11).

*Warm-up Drift Analogy* ( $\alpha_1$  and  $\alpha_2$ )

Both  $\alpha_1$  and  $\alpha_2$  are heat functions, being proportional to  $\Delta E_p I_p$  and

$\Delta E_h I_h$ , respectively. Their characteristics are identical to the well-known warm-up drift of the oscillation frequency. When the local oscillator is energized from "cold start," the plate dissipation increases from 0 to  $E_p I_p$ , and similarly, the heater power increases from 0 to  $E_h I_h$ . Under this condition,

$$\Delta E_p I_p = E_p I_p,$$

$$\Delta E_h I_h = E_h I_h.$$

Thus the theoretical warm-up frequency deviation, when the instantaneous frequency shift is neglected, is given by

$$\Delta f = k_2 (E_p I_p) (1 - e^{-\beta_1 t}) + k_3 (E_h I_h) (1 - e^{-\beta_2 t}).$$

In actual operation, however, there is a time delay between the instant when the local oscillator is energized and the instant when oscillation commences. Because of this delay, the observed warm-up frequency deviation is always less than the theoretical value. This delay is taken into account in Equation (12),

$$\Delta f = k_2 (E_p I_p) [1 - e^{-\beta_1 (t - t_0)}] + k_3 (E_h I_h) [1 - e^{-\beta_2 (t - t_0)}], \quad (12)$$

where  $t_0$  is the time required to start oscillation, or any time thereafter that the warm-up drift is of interest. In television receivers, for instance, the kinescope and some deflection stages begin to function properly in approximately 30 seconds. Therefore, any frequency deviation of the local oscillator during the first 30 seconds is incidental and can be ignored.

The complete frequency characteristics of the 250-megacycle oscillator of Figure 1 during the warm-up period are indicated in Figure 6. Oscillation started in about 15 seconds, at which time both  $\alpha_p$  and  $\alpha_h$  existed. Under normal conditions, this frequency gyration has no effect on the receiver performance. In receivers incorporating discriminator-type automatic frequency control, however, this frequency gyration warrants special attention. In the presence of an interfering signal at a frequency close to that of the desired signal, the local oscillator might be locked to the unwanted carrier.

For  $t \geq 0.5$  minute, the warm-up drift of the oscillation frequency behaves in exactly the same manner as  $\Delta f_1 + \Delta f_2$  due to simultaneous  $\Delta E_p$  and  $\Delta E_h$ . This similarity between voltage sensitivity and warm-up temperature sensitivity of local oscillators simplifies the stabilization problem, because it is now possible to compensate both the warm-up

frequency deviation and the frequency deviation resulting from varying operating voltages by a single means.

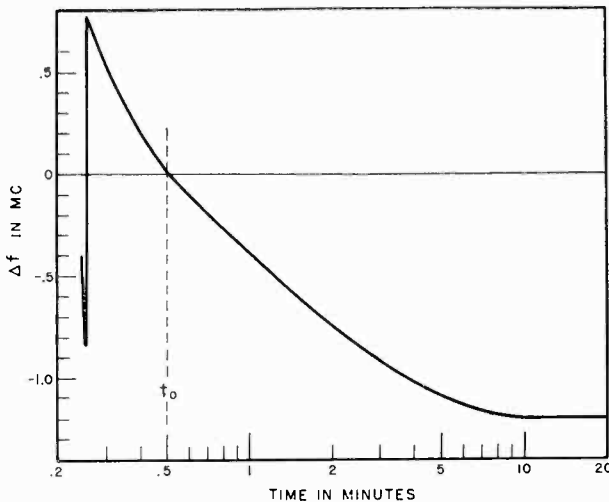


Fig. 6—Warm-up frequency characteristics, uncompensated condition.

### $\beta_1$ and $\beta_2$

To insure good stabilization of the heat functions, not only must the magnitudes of  $\alpha_1$  and  $\alpha_2$  be minimized, but the stabilization means must also exhibit definite time constants. The requirement on time constants necessitates new design considerations of oscillator tubes whereby the flow of heat from the "hot bodies" inside the tube to the stabilization elements is expedited.

### STABILIZED LOCAL OSCILLATOR

As an illustration of the application of the observed results and analysis, the circuit shown in Figure 1 has been modified<sup>5</sup> as shown in Figure 7. The modifications pertain to

- (1) Compensation for  $\alpha_1$  and  $\alpha_2$  by means of two temperature-sensitive capacitors,  $C_1$  and  $C_2$ ;
- (2) Compensation of  $C_3$  for heat flow from other parts of the receiver to the associated circuit elements of the local oscillator;

<sup>5</sup> W. Y. Pan and D. J. Carlson, "Analytic Approaches to Local Oscillator Stabilization," *Trans. I.R.E. PGBTR*, No. 3, p. 57, October, 1956.

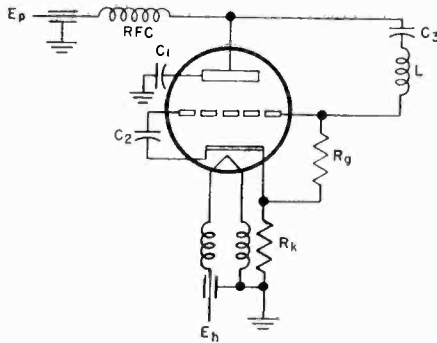


Fig. 7—Stabilized oscillator circuit.

- (3) Adjustment of optimum oscillation strength with proper feedback network, grid-limiting resistance,  $R_g$ , and plate voltage;
- (4) Reduction of the effect of cathode interface resistance.

The comparative frequency characteristics of the original and the modified local oscillators shown in Figures 1 and 7 are illustrated by the dotted and solid curves, respectively, in Figure 8. The line voltage was held constant during the first ten minutes. At  $t = 10$ ,  $E_L$  was raised instantly by 15 per cent for a period of ten more minutes, at which time the line voltage was returned to normal.

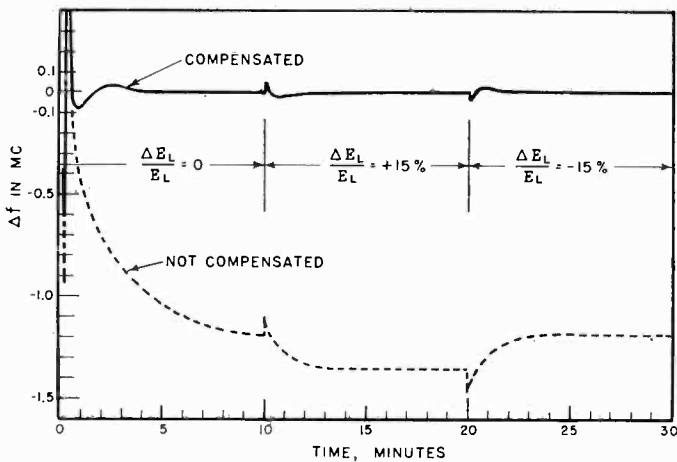


Fig. 8—Voltage and warm-up temperature sensitivities, compensated and uncompensated conditions.

# DETERMINATION OF LEAD-WIRE INDUCTANCES IN MINIATURE TUBES\*

BY

W. A. HARRIS AND R. N. PETERSON

RCA Electron Tube Division,  
Harrison, N. J.

*Summary*—This paper describes measurements of internal inductances and resonant frequencies in miniature tubes operating in the UHF television band. Measurement techniques are described, and the equivalent circuits of several miniature tubes are presented. The significance of the measurements with respect to tube and circuit design is discussed. The feedback elements, or elements common to input and output circuits, are found to be of particular importance.

## INTRODUCTION

MINIATURE TUBES are used successfully as amplifiers at frequencies up to about 500 megacycles and as oscillators at frequencies up to about 1000 megacycles. Above these frequencies, their usefulness is limited due to the effects of internal lead wires, bases, and sockets. Minimization of these effects by changes in tube design or by the use of corrective circuits requires precise evaluation of the individual inductances and capacitances involved and of their effects at the desired operating frequencies. The values of these individual inductances and capacitances at ultra-high frequencies cannot be determined by direct measurement because most of the terminals needed for such measurements are inside the tube envelopes. They can, however, be determined by measurement of the resulting UHF susceptances and subsequent calculations based on appropriate circuit theory.

This paper describes procedures for measurement of tube and socket susceptances at ultra-high frequencies and for evaluation of the contributing inductances and capacitances. It also discusses the effects of lead-wire inductance on tube performance and describes measures which can be taken to minimize these effects so as to increase the maximum usable frequencies of miniature types.

## SHORT-CIRCUIT PARAMETERS

The short-circuit admittances of a disc-seal triode measured at

---

\* Manuscript received July 20, 1959.

grounded-grid operating conditions are given approximately by the following equations:

$$Y_{11} = g_m \left( 1 + \frac{1}{\mu} \right) + j\omega C_{11} \quad (1)$$

$$Y_{21} = g_m \left( 1 + \frac{1}{\mu} \right) \exp \{ -j\omega\tau_{21} \} \quad (2)$$

$$Y_{12} = \frac{Y_{11}}{1 + \mu} \quad (3)$$

$$Y_{22} = j\omega C_{22} + \frac{Y_{21}}{1 + \mu} \quad (4)$$

where

$Y_{11}$  is the short-circuit input admittance,

$g_m$  is the mutual conductance,

$\mu$  is the amplification factor,

$C_{11}$  is the total short-circuit input capacitance measured under operating conditions,

$\omega$  is the angular frequency measured in radians per second,

$Y_{21}$  is the short-circuit forward transfer admittance,

$\tau_{21}$  is the phase-delay time applicable to  $Y_{21}$ ,

$Y_{12}$  is the short-circuit feedback transfer admittance,

$Y_{22}$  is the short-circuit output admittance, and

$C_{22}$  is the total short-circuit output capacitance measured under operating conditions.

Equations (1) through (4) were empirically derived from measurements on actual tubes of disc-seal construction after small corrections were made for the series inductances and external capacitances occurring even in these types. Figure 1 shows the short-circuit parameters for one tube type as functions of frequency for frequencies up to 1300 megacycles. The curves are well represented by Equations (1) to (4).

The short-circuit input conductance,  $G_{11}$ , and the magnitude of the forward transfer admittance,  $Y_{21}$ , are independent of frequency

through the range of measurement and are approximately equal to the low-frequency transconductance,  $g_m$ . Because the amplification factor,  $\mu$ , for this tube was about 50, the factor  $(1 + 1/\mu)$  in Equations (1) and (2) is not much greater than unity. The short-circuit input susceptance increases in proportion to frequency, corresponding to a capacitance of approximately 1.3 micromicrofarads. The time-delay constant,  $\tau_{21}$ , rotates the phase of  $Y_{21}$  by 90 degrees at 1250 megacycles so that the real part,  $G_{21}$ , is zero at this frequency. The value for  $\tau_{21}$ , therefore, is  $0.2 \times 10^{-9}$  second. Theoretical considerations indicate that this constant should be two-thirds of the total electron transit time from cathode to plate.

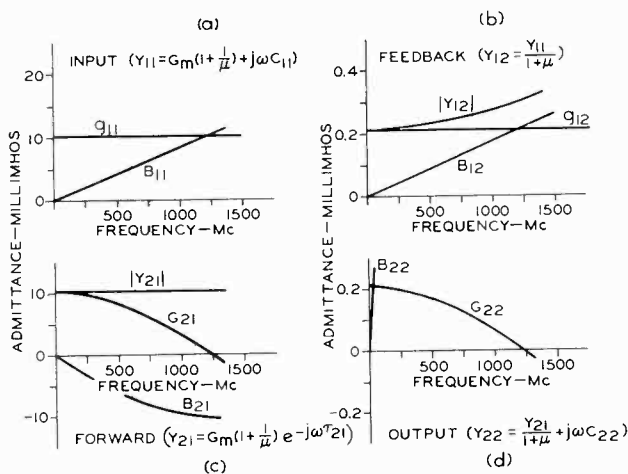


Fig. 1—Short-circuit conductances, susceptances, and admittances of a tube which has no inductance in series with its electrode: (a) input; (b) feedback; (c) forward transfer; (d) output.

The short-circuit output conductance is  $G_{21}/(\mu + 1)$ . This conductance, therefore, decreases to zero at 1250 megacycles and becomes negative at higher frequencies. The major part of the short-circuit output susceptance is due to the plate-to-grid capacitance, which is about 1 micromicrofarad for this tube. The short-circuit feedback admittance is  $Y_{11}/(\mu + 1)$  and can be represented as a conductance of 0.21 millimho plus a capacitance of 0.03 micromicrofarad.

The curves shown in Figure 1 were obtained from measured data after the following corrections were made:

a. The reactance corresponding to an inductance of approximately 2 millimicrohenries was subtracted from the reciprocal of the meas-

ured short-circuit input admittance to determine the conductance value shown in Figure 1 (a).

b. The output conductance measured with the tube cold was subtracted from the total measured short-circuit output conductance to obtain the value shown in Figure 1 (d).

c. The forward transfer admittance determined from gain measurements was corrected for the calculated effect of the inductance in series with the input terminal.

d. The measured short-circuit input capacitance was reduced by an amount estimated to represent the capacitance through the glass and the capacitance between the inactive part of the cathode structure and the grid.

Tubes such as the miniature types, which have element connections made by wire leads passing through a stem, have reactance and susceptance elements in addition to those indicated in Figure 1. Tube sockets also add reactance and susceptance to the system actually available for measurement. The inductance and capacitance values chargeable to the stem and the internal leads can be determined by the following procedure:

- (1) The input and output susceptances of the cold tube are measured at several frequencies within the desired operating range.

- (2) The resulting input and output susceptances for the tube alone are converted mathematically to equivalent input-circuit and output-circuit capacitances.

- (3) Equivalent circuits for the tube as seen at the input and output terminals are set up. In the determination of configurations and values for these equivalent circuits, both the capacitances calculated in step (2) and those obtained by direct measurement at low frequencies are taken into consideration.

- (4) The inductances of the internal and external grid-lead wires are determined by additional measurements and calculations.

- (5) The components of the grid-cathode and grid-plate capacitances contributed by the stem assembly and base are determined by measurements on separate stem and base assemblies. These components are then subtracted from the total capacitance values determined in the preceding steps.

- (6) A final equivalent circuit showing individual values for all inductance and capacitance components of the tube and socket is set up.

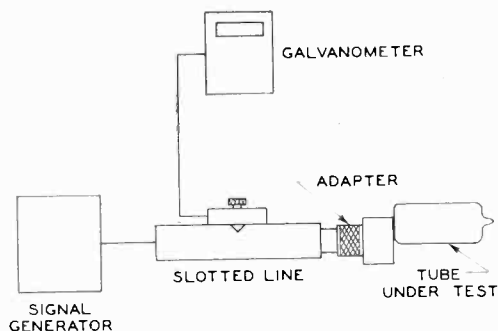


Fig. 2—Equipment used for measurements of input and output susceptance.

#### DETAILED PROCEDURE

The measurements and calculations were made on three miniature triode types: the nine-pin type 6BC4 and the seven-pin types 6AF4 and 6J4-WA. These types were selected because of their wide application in UHF equipment and because their designs are representative of the majority of UHF miniature types. All equivalent circuits, curves, and other data shown are for the grounded-grid circuit configuration.

The input and output susceptance measurements described in step (1) above were made with the aid of a slotted line. A block diagram of the circuit used for these measurements is shown in Figure 2. Special coaxial adapters were designed to provide the shortest possible connections between the tubes and the slotted line. The adapter used for the 6BC4 is shown in Figure 3. The base-pin circle is so positioned that up to three adjacent base pins (for example, the two plate pins or the three heater and cathode pins) may be inserted in the center conductor and all other pins grounded. This design permits the adapter to be treated as a short section of coaxial line having lumped capacitance at its tube end. The short-circuit and open-circuit characteristics of the adapter at several frequencies were determined first. The input and output susceptances of the tube and adapter were then measured at the same frequencies, and the susceptances of the tube alone determined with the aid of a transmission-line chart.

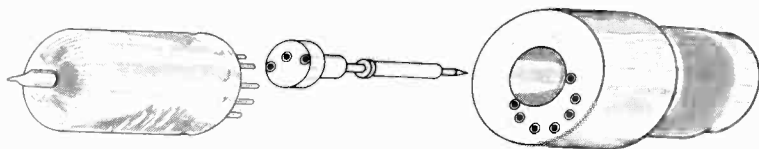


Fig. 3—Coaxial adapter socket used for susceptance measurements on 6BC4.

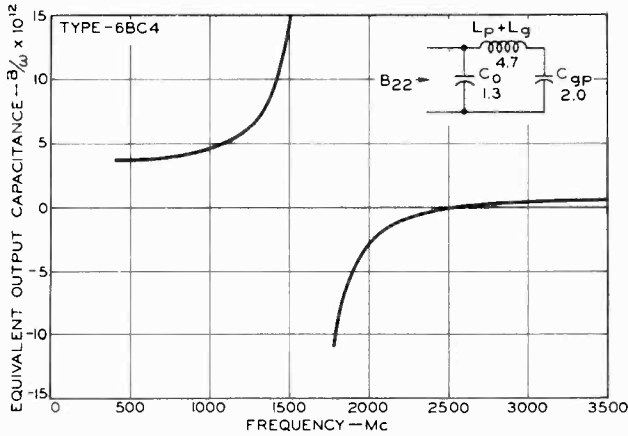


Fig. 4—Curve of equivalent capacitance across the output terminals of the 6BC4 and approximate equivalent circuit derived from curve.

The resulting susceptances were then converted to equivalent capacitances ( $C = B/\omega$ ) as seen at the input and output terminals of the tube for the grounded-grid circuit configuration. Figure 4 shows a plot of the equivalent capacitance across the output terminals of the 6BC4. The approximate equivalent circuit derived from the plotted data is shown as an insert. The zero-frequency asymptote of the curve is the sum of the two capacitances, the pole is the series-resonant frequency of  $L$  and  $C_{gp}$ , and the zero is the shunt resonant frequency of the circuit.

Figure 5 shows the curve for the equivalent capacitance seen at

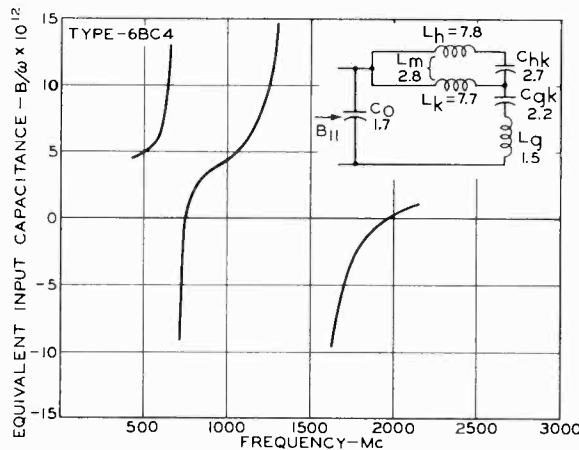


Fig. 5—Curve of equivalent capacitance across the input terminals of the 6BC4 and approximate equivalent circuit derived from curve.

the input terminals of the 6BC4, together with the approximate equivalent circuit. It can be seen that the resonant frequency of the heater-cathode circuit introduces complications, i.e., the curve of equivalent capacitance versus frequency contains two poles and two zeros.

Values for the equivalent circuits in Figures 4 and 5 were determined by taking into consideration the capacitances obtained by direct measurements at low frequencies and those calculated from UHF susceptance measurements. To avoid complication of the equivalent circuit shown in Figure 5, the two heater connections were treated

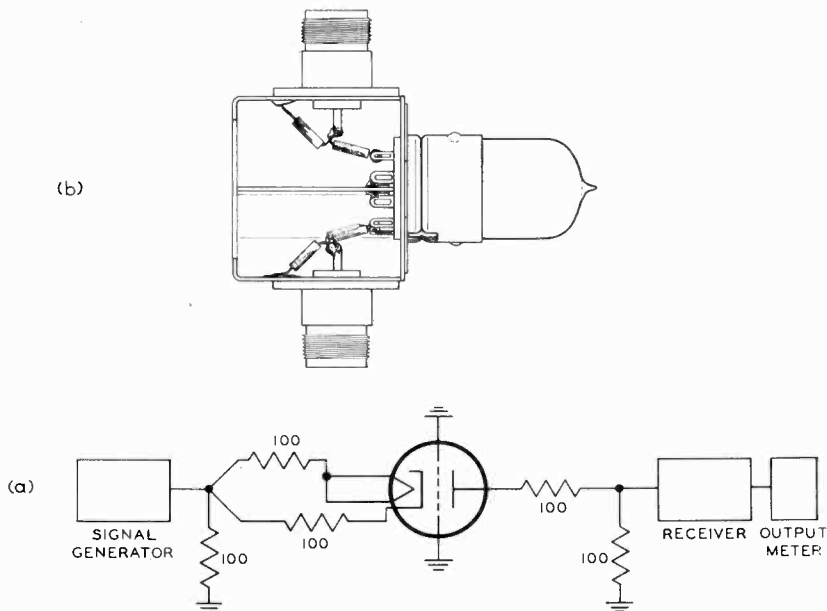


Fig. 6—(a) Circuit arrangement used to determine grid-lead inductance; (b) tube mounting and shielding arrangements.

as a single lead. The mutual inductance between heater and cathode was included in this circuit because it was necessary to take this inductance into consideration in obtaining proper correlation between the measured (low-frequency) and calculated (UHF) capacitance values.

The grid-lead component  $L_g$  of the total inductance  $L$  in Figure 4 was determined by measuring the frequency at which the feedback caused by this component was cancelled out by the feedback through the plate-to-cathode capacitance. The circuit used for this measurement is shown in Figure 6a. The frequency at which the two types of feedback are cancelled is indicated by an almost complete loss of

signal in the receiver. The series and shunt resistors in the input and output circuits were chosen to provide terminal impedances of approximately 50 ohms at all frequencies of interest. Separate resistors were used in the cathode and heater leads to suppress the effects of heater-cathode resonance. It was necessary to install all the components of the tube circuit in shielded units of the type shown in Figure 6b, to fit the partition shield closely to the tube socket, and to return the shunt resistors and grid connections to the chassis proper. The effect of an increase in inductance on the frequency for minimum response was checked by raising the tube slightly in its socket so as to increase the grid-circuit inductance. As expected, this change substantially increased the receiver output, which was then brought to a minimum again by tuning the generator and receiver to a slightly lower frequency.

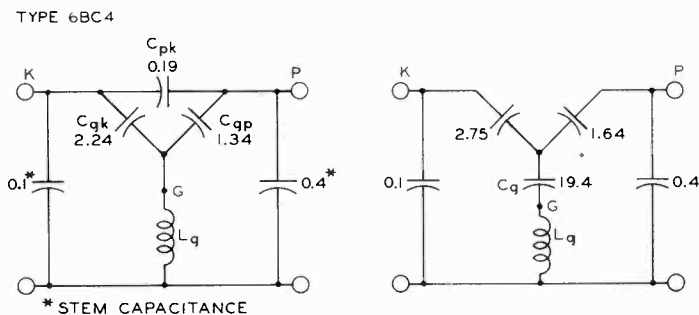


Fig. 7— $\Delta$ - $Y$  transformation for calculation of grid-lead inductance.

The effects of the internal grid-lead wires were separated from those of the base pins and socket by additional measurements made with all grid pins grounded by a formed strip of copper foil mounted on top of the socket. As expected, the frequency at which the two feedback effects cancelled increased under these conditions.

#### EVALUATION OF RESULTS

The method used to evaluate the results of these measurements is shown in Figure 7. The stem and base components of the grid-cathode capacitance  $C_{gk}$  and grid-plate capacitance  $C_{gp}$  were determined by measurements made on separate stem and base assemblies and subtracted from the calculated values for  $C_{gk}$  and  $C_{gp}$ . The resulting delta-network values were then converted to equivalent  $Y$ -network values by means of the transformation

$$C_g = C_{gk} + C_{gp} + \frac{C_{gk} C_{gp}}{C_{pk}} \tag{5}$$

The frequency for minimum response was then the series-resonant frequency of the grid-lead inductance,  $L_g$ , and the common-branch capacitance  $C_g$ . The value of  $L_g$  at this frequency was determined from the relationship

$$\omega^2 L_g C_g = 1. \tag{6}$$

Because  $C_g$  in the equivalent  $Y$  network varies inversely with the plate-cathode capacitance  $C_{pk}$ , an increase in  $C_{pk}$  increases the frequency for minimum response. This increase in frequency is not, however, an indication of greater tube merit; it is significant only

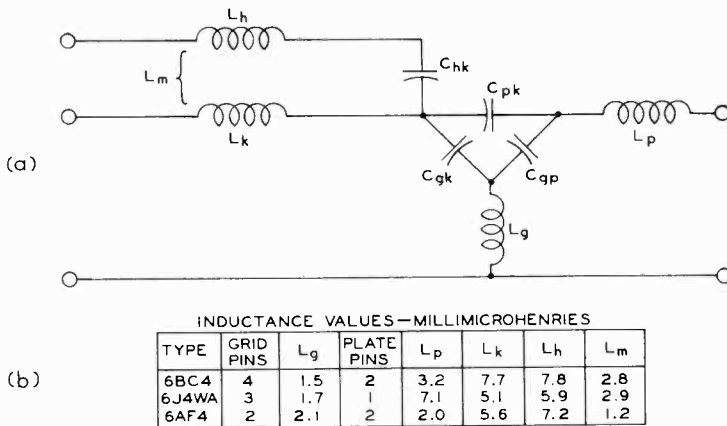


Fig. 8—(a) Equivalent circuit of a miniature triode; (b) calculated values of lead inductances for the 6BC4, 6J4-WA, and 6AF4.

in calculation of  $L_g$ . It should also be noted that grid-lead inductance values obtained by this method include the mutual inductance between the plate and cathode lead wires. This mutual inductance is, however, properly considered as part of the magnetic coupling between the input and output of the tube.

Figure 8 shows the calculated lead-wire inductances for the 6AF4, 6BC4, and 6J4-WA. These three types have similar internal electrode structures but different connections between electrodes and base pins. The 6AF4, which is designed for UHF oscillator service, has two grid leads and two plate leads; the 6J4-WA, which was designed for grounded-grid amplifier service, has three grid leads and one plate

lead; and the 6BC4, which is a nine-pin type also designed for grounded-grid amplifier service, has four grid leads and two plate leads. All three types have only a single cathode lead. The inductance values listed in Figure 8 do not include the inductances of the portions of the tube pins below the surface of the glass base nor the socket inductances.

The effects of the tube lead-wire inductances and capacitances were evaluated by analysis of equivalent circuits using these inductances and capacitances as parameters. Figure 9 shows such an equivalent circuit for the 6BC4. The box containing the short-circuit admittance symbols represents the active portion of the tube, i.e., the portions of the electrode structure which are directly in the electron stream. The capacitances immediately outside the box are those contributed by the portions of the electrode structure outside the electron stream and by the adjacent interlead capacitances. The capacitances shown between the heater and cathode terminals and between the tube terminals and ground are those of the tube socket. The lead inductance values are greater than those shown in Figure 8 because the inductances of the socket connections are included.

The interelectrode spacings, the amplification factor, and the low-frequency transconductance of the 6BC4 are very close to the corresponding quantities for the disc-seal tube represented by the curves of Figure 1. Consequently, the short-circuit admittances derived from Figure 1 are assumed to apply to the internal structure of type 6BC4. The values are:

$$Y_{11} = 10.2 \times 10^{-3} + j\omega 1.32 \times 10^{-12} \quad (7)$$

$$Y_{12} = 0.21 \times 10^{-3} + j\omega 0.028 \times 10^{-12} \quad (8)$$

$$Y_{21} = 10.2 \times 10^{-3} \exp \{-j\omega 0.2 \times 10^{-9}\} \quad (9)$$

$$Y_{22} = 0.21 \times 10^{-3} \cos \{\omega 0.2 \times 10^{-9}\} + j\omega 1.12 \times 10^{-12}. \quad (10)$$

A straightforward procedure for analysis of this circuit is:

(a) Add the shunt susceptances represented by capacitances  $C_a$ ,  $C_b$ , and  $C_c$  to the measured short-circuit admittances and derive the corresponding open-circuit impedances for a number of frequencies within the desired operating range.

(b) Add to these open-circuit impedances the reactances of the series elements  $L_h$ ,  $C_{hk}$ ,  $L_k$ , and  $L_p$ , and convert the resulting values back to short-circuit admittances.

(c) Add to these short-circuit admittances the susceptances represented by the terminal capacitances.

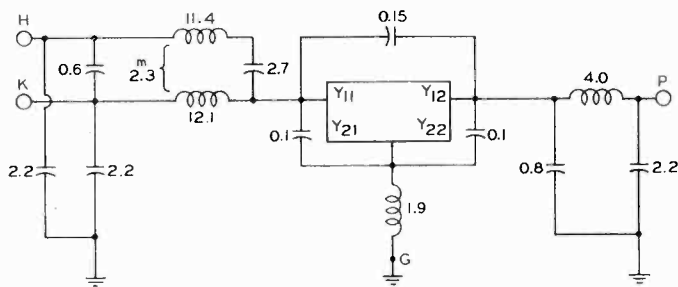
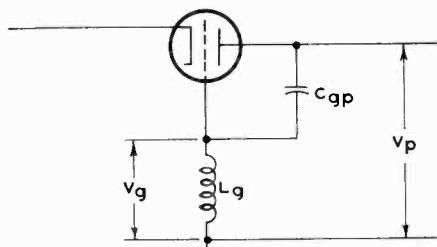


Fig. 9—Equivalent circuit used to determine effects of tube and socket parameters on tube performance.

This method is extremely laborious, and yields values for only five or six frequencies per day, even when only a small number of errors are made. Perhaps it could be used as the basis for a computer program. A much more rapid treatment, involving some approximations but better illustrating the effects of individual inductance and capacitance elements, is shown in Figure 10. This treatment is based on the fact that the grid-lead inductance  $L_g$  causes the feedback admittance to increase with frequency and reduces the short-circuit output conductance. It can be seen in Figure 10 that the feedback current flowing through the grid-plate capacitance and grid-lead inductance produces a voltage at the grid ( $V_g$ ) opposite in sign to the voltage at the plate ( $V_p$ ).  $V_g$  reduces the effective amplification factor of the tube to a value  $\mu'$  such that

$$\frac{1}{\mu'} \approx \frac{1}{\mu} - \omega^2 L_g C_{gp} \tag{11}$$



$$V_g \approx -\omega^2 L_g C_{gp} V_p$$

$$1/\mu' \approx 1/\mu - \omega^2 L_g C_{gp}$$

Fig. 10—Equivalent circuit illustrating effect of grid-lead inductance on amplification factor.

and, therefore, causes corresponding changes in feedback admittance ( $Y_{12}$ ) and output conductance ( $G_{22}$ ). The new values of  $Y_{12}$  and  $G_{22}$  can be computed by substitution of  $\mu'$  for  $\mu$  in the basic equations previously given for these parameters. Figure 11 shows a simplified equivalent circuit for the 6BC4 based on the use of this method, and curves showing the corresponding values for feedback admittance  $Y_{12}'$  and output conductance  $G_{22}'$ . Corresponding values for effective input conductance  $G_{11}'$  and forward transfer admittance  $Y_{21}'$  are:

$$G_{11}' = 10.2 \times 10^{-3} \quad (12)$$

$$Y_{21}' = 10.2 \times 10^{-3} \exp \{-j\omega 0.2 \times 10^{-9}\}. \quad (13)$$

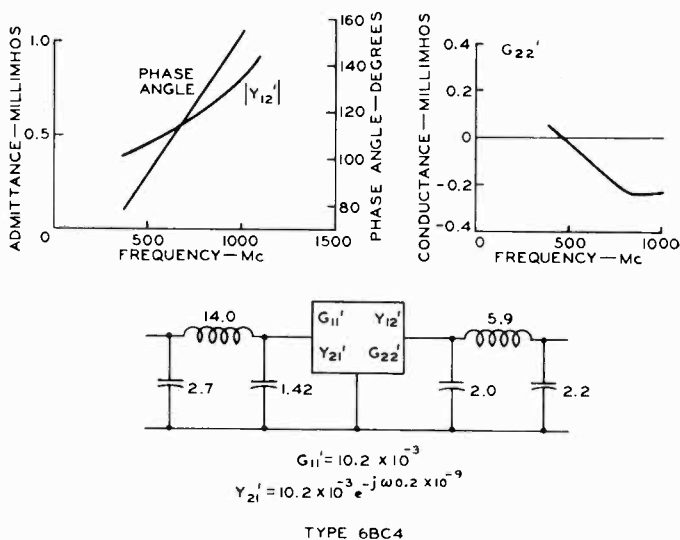


Fig. 11—Equivalent circuit and curves showing effect of change in  $\mu$  on  $Y_{12}$ , phase angle, and  $G_{22}$ .

The analysis has not been carried further because the elements shown outside the box in Figure 11 can usually be treated as part of the external circuit.

Among the important effects evident in Figure 11 are the increase in the magnitude of the feedback admittance  $Y_{12}$  with frequency and the negative values of short-circuit output conductance  $G_{22}$ . For stable amplifier operation, the total output conductance including load conductance must be positive and of at least the same order of magnitude as the feedback admittance. Gain, however, is approximately the ratio of forward transfer admittance to load conductance, so that the higher

the load conductance, the lower the gain. Furthermore, the fact that the feedback admittance is high and the internal output conductance negative suggests that the circuit will oscillate if the load circuit is improperly tuned or the load coupling is altered. These conclusions are verified by the observed behavior of miniature tubes at ultra-high frequencies.

#### CORRECTIVE MEASURES

The frequency at which output conductance  $G_{22}$  becomes negative and the equivalent amplification factor  $\mu'$  changes sign can be increased by insertion of capacitance in series with the connections to the grid terminals of the tube. The use of such capacitance, however, reduces the amplification factor and increases the feedback admittance at low frequencies.

Feedback may be completely neutralized over narrow frequency bands by the use of shunt inductance or capacitance between the plate and cathode terminals of the tube, and of series inductance or capacitance between the grid terminals of the tube and ground. These external elements, when properly chosen, can alter the phase of the feedback currents due to the internal lead-wire inductances sufficiently to permit complete balance. When these measures are used, it is possible to obtain performance from miniature tubes that closely approaches that of disc-seal tubes having similar internal characteristics. Full equivalence, however, cannot be obtained because of inherent resistance losses in tube lead wires, socket connections, and the added circuit elements.

#### CONCLUSIONS

Although lead-wire inductances have been derived in this study only for the 6AF4, 6BC4, and 6J4-WA, the results obtained make it possible to draw some general conclusions concerning the inductance values to be expected in other tubes. For example, the inductance values given in Table I can be used to determine corresponding values for tubes having electrode structures similar to those of the three types investigated, and to estimate values for types having slightly longer internal lead wires or different basing. In the application of the data given to tube design, it should be borne in mind that since the inductance of a conductor varies inversely with the logarithm of its diameter, the improvement obtainable by an increase in lead-wire diameter is often discouragingly small.

The form of the curve shown in Figure 5 suggests that when the 6BC4 is used as an amplifier in the UHF television broadcast band,

the heater leads should not be bypassed to the cathode at the socket but should instead be provided with chokes which will resonate with the heater-cathode capacitance at a frequency below the low end of the band. Bifilar-wound chokes having an inductance of 60 to 100 millimicrohenries are recommended; such chokes can easily be wound so as to be free from self-resonances in the UHF television band. These considerations also apply to the 6AF4 when it is used as an oscillator in the UHF television band, and to the 6J4-WA when it is used as an amplifier at frequencies above 300 megacycles per second. The tube heater circuit was omitted from the simplified diagram shown

Table I—Typical Lead-Wire and Socket Inductances and Capacitances for Miniature Tubes

INDUCTANCE — <i>Millimicrohenries</i>	
Heater .....	6.0-8.0
Cathode .....	5.0-8.0
Mutual (H-K) .....	1.0-3.0
Plate:	
One Lead .....	6.0
Two Leads .....	2.0-3.0
Grid:	
One Lead .....	3.3
Two Leads .....	2.1
Three Leads .....	1.7
Four Leads .....	1.5
Socket—Per Lead .....	1.6
Wiring—Per mm. ....	0.5-0.7
CAPACITANCE — <i>Micromicrofarads</i>	
Tube Stem:	
Adjacent Leads .....	0.1
Socket:	
Adjacent Leads .....	0.5-1.0
Leads to Ground .....	1.0-1.5

in Figure 11 because it was assumed that such chokes are used to place the heater and cathode at the same r-f potential.

General conclusions which can be drawn from this study are that the internal lead-wire inductances of miniature tubes can be accurately determined, and that a knowledge of these inductances is extremely helpful in predicting and explaining the performance of such tubes at ultra-high frequencies. This study also indicates that, with proper circuit design, lead-wire inductances and feedback need not be insurmountable obstacles to the use of miniature tubes at ultra-high frequencies.

# SPECTRUM-SELECTION AUTOMATIC FREQUENCY CONTROL OF ULTRA-SHORT-PULSE SIGNALLING SYSTEMS\*

BY

HARRY KIHN AND R. J. KLENSCH

RCA Laboratories,  
Princeton, N. J.

*Summary*—A system is described which maintains a constant frequency difference between a carrier frequency modulated by ultra short pulses of 10 millimicrosecond duration and a local electrically tuned oscillator. The pulse spectrum distribution is an order of magnitude greater than for existing systems but the circuitry is simple and easily aligned and uses commercially available miniature tubes.

## INTRODUCTION

THE PROBLEM of holding constant the frequency difference between a pulsed carrier source such as a magnetron and a local oscillator (klystron or equivalent) has been extensively dealt with in the literature of radar systems. Additionally, other uses of frequency control in color television (burst synchronization), FM receivers, and single-sideband suppressed-carrier systems have been discussed and widely used. All of these applications involve the precise location of the unmodulated carrier, or more exactly the frequency average of all the sidebands of the spectrum of the modulated or pulsed carrier whose duration is always greater than 0.2 microsecond. The method generally used, therefore, is the conventional amplification of the heterodyned pulse sample in a narrow-band i-f amplifier generally less than 10 megacycles wide, and utilization of a Foster-Seeley discriminator, a Weiss discriminator, or ratio detector to provide frequency-duration information. This can then be used to control an electrically tunable oscillator such as a klystron or oscillator-reactance tube to hold the i-f constant. In the case of radar applications where the bandwidth of the automatic-frequency-control (a-f-c) amplifier is small compared to the thermal drifts of the klystron and magnetrons used, lock-on frequency seeking sweeps must be provided. This generally consists of a voltage sawtooth sweep of the klystron reflector or thermal tuned grids depending on the means of tuning used. If, however, extremely short pulses are used to modulate the carrier as, for

\* Manuscript received April 8, 1959.

example, a 0.01 microsecond cosine-shaped pulse which has frequency components up to 100 megacycles on each side of the carrier frequency, bandwidths of 150 megacycles would be required in a conventional a-f-c system.

Ultra-short-pulse operation, because of the large peak-to-average-power ratio, tends to saturate the mixer crystal considerably before the average power is sufficient to control an electrically tunable oscillator. Furthermore, the i-f amplifier must have a large dynamic range if ultra-short pulses are used to produce an average rather than cyclical frequency correction. Since the crystal mixer output is quite low, gains of 40 decibels or more are required at large gain-bandwidth factors. Only travelling-wave tubes or ultra-high  $G_m$  triodes in special wide-band circuitry could be used in a conventional a-f-c system, and these result in a complex and costly structure. Furthermore, with a wide-band system, video components resulting from the heterodyning process are not sufficiently attenuated to prevent their unbalancing the discriminator on the low-frequency side of the i-f carrier. This tends to produce a discriminator output even in the absence of true i-f signals. These shortcomings of the use of conventional a-f-c techniques for ultra-short-pulse systems led to the development of the spectrum-selection automatic frequency control which is the subject of this paper.

#### THEORY OF SPECTRUM SELECTION AUTOMATIC FREQUENCY CONTROL

If the pulse-amplitude-modulated carrier maintains its spectral distribution constant and symmetrical about the carrier frequency, a novel characteristic of this spectrum may be used for the frequency control. Figure 1 shows the spectrum locus  $G(f)$  of a 0.01-microsecond pulse which approximates a cosine distribution. The spectral components of a cosine pulse of peak amplitude  $A$  and duty cycle  $t_0/T$  where  $F = 1/T =$  repetition rate, is given by the relationship

$$a_n = \frac{4}{\pi} \frac{t_0}{T} \frac{A}{1 - \left(\frac{2nt_0}{T}\right)^2} \cos \pi n \frac{t_0}{T}.$$

A second curve is shown in dashed lines in Figure 1; this curve represents the product of spectrum  $G(f)$  and the spectrum slope  $dG(f)/df$  plotted as a function of frequency. It is evident that the maxima of the latter curve occurs at two frequencies, one approximately 30 megacycles above and the other 30 megacycles below the i-f center frequency (170 megacycles). It is at these frequencies that the

spectrum is changing most rapidly; hence, selecting a band of frequencies (10 megacycles) symmetrically disposed about these maxima and comparing the upper band against the band below the carrier frequency will allow the location of the spectrum average (i-f center frequency) with maximum precision. This results from the fact that slight changes of the center frequency, such as might be produced by local oscillator drift, produces most rapid change in differential voltage

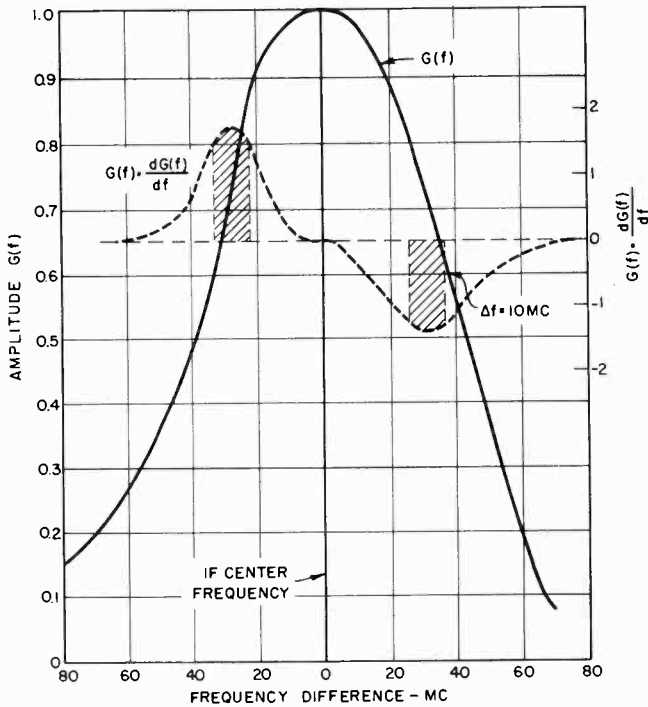


Fig. 1—Spectrum distribution of a 0.01-microsecond pulse (solid line).

for a given selected bandwidth. It is obvious that a narrow-band spectrum comparison in the vicinity of the i-f center frequency (zero frequency difference) will be least effective in indicating a shift in the center frequency.

The process of optimum spectrum segment selection involves consideration of two factors. These are the width of the segments of the  $G(f)dG(f)/df$  characteristic selected, and the other is the attainable gain per stage, which depends on the bandwidth selected. The gain per stage is given by the relation

$$G = \frac{1}{2\pi C} \frac{G_m}{\Delta f},$$

where  $G_m$  is the tube transconductance and  $C$  the total shunt capacitance. If a very wide segment is selected ( $\Delta f$  large), the gain per stage approaches unity; hence the cumulative gain of  $N$  stages of a sequential amplifier increases very slowly and the resulting bandpass of the amplifier shrinks rapidly. The greater number of stages required for this reduced gain per stage would eventually lead to an impractical amplifier even with staggered tuning. However, reducing the width of the spectrum sample ( $\Delta f$ ) decreases the pulse amplitude approximately inversely with bandwidth even though the gain per stage increases. Determination of the optimum bandwidth requires consideration of the shape of the  $G(f)dG(f)/df$  versus  $f$  curve as well as the capabilities of the 6AK5 tubes used in the a-f-c amplifier. This includes both the figure of merit  $G_m/2\pi C$  and the dynamic grid-voltage-swung characteristic just short of driving into grid current. The optimum bandwidth was evaluated as approximately 10 megacycles. Theoretically, for an amplifier with unlimited gain capabilities and with a rectangular pass band with linear phase shift, the pulse at the output of the amplifier when driven by a short rectangular pulse, would be independent of the bandwidth. This can be shown as follows:

$$E_{\text{pulse}} = K_1 \Delta f \quad \text{for } \Delta f \ll \frac{1}{t_0},$$

$$\text{Amplifier gain} = G = \frac{K_2}{\Delta f},$$

$$E_{\text{output}} = E_{\text{pulse}} \times G = K_1 \Delta f \times \frac{K_2}{\Delta f} = K.$$

The selected upper and lower sideband segments are amplified in a novel dual-frequency amplifier, described subsequently, and the resulting stretched pulses are compared in a discriminator. This uses gated balanced plate detection followed by integration and enhancement of the differential component in a balanced differential amplifier described later.

#### RADAR SYSTEM

Figure 2 is a block diagram of a radar system which might advantageously use spectrum selection a-f-c. It is quite conventional except for the short pulse used to drive the magnetron. The a-f-c mixer may

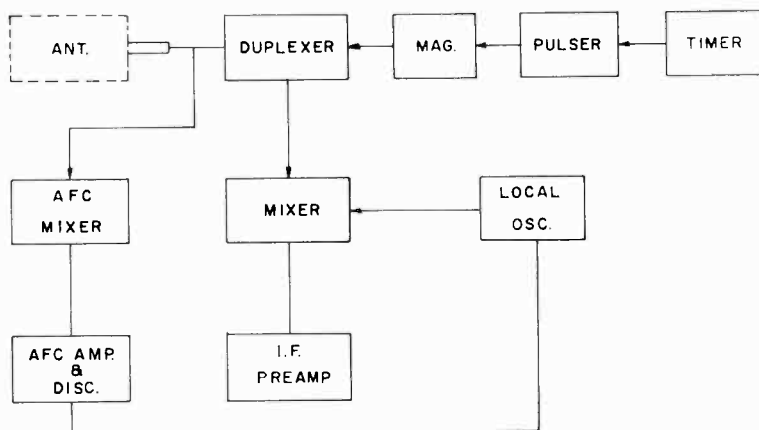


Fig. 2—Radar system.

be either a single-ended or a balanced type, using a magic-T type configuration. The balanced type has the advantage of at least twice the output of i-f voltage with great reduction in the video components. The only disadvantage is the requirement of a balanced-to-single-ended transformer in the input of the amplifier. Such a transformer has been designed using a ferrite core to attain the large coupling factor required for wide bandwidth. Extremely short leads were mandatory to allow resonance at 170 megacycles and adequate coupling of the low-impedance microwave crystals to provide single-damped, double-tuned circuitry. Since there is extensive discussion in the literature of radar systems incorporating a-f-c of the local oscillator klystron, further discussion is confined to the elements of the spectrum-selection a-f-c system shown in Figure 3.

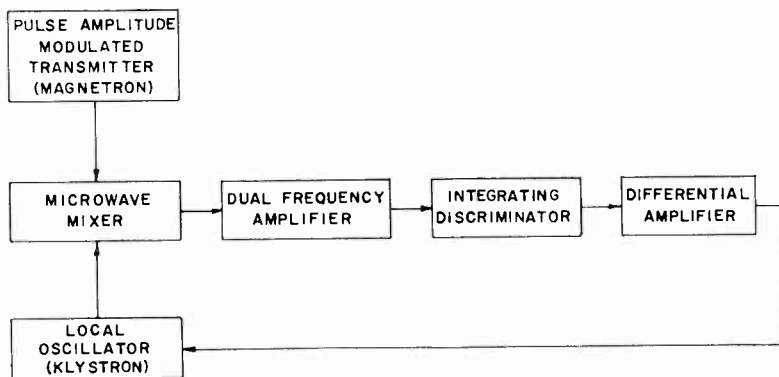


Fig. 3—Spectrum-selection automatic frequency control.

Here the output of the microwave mixer feeds the six-stage dual-frequency amplifier. The stretched-pulse output of the amplifier proceeds to a gated, integrating, double-triode discriminator which compares the two pulses resulting from the upper and lower spectrum bands and produces a d-c voltage whose amplitude and deviation from a steady-state value depend on the departure of the input pulse spectrum from the desired operating conditions. Since the control voltage required for the klystron must approximate a steady-state voltage, or at worst a slowly varying one, the integration in the plate circuit of the 12AX7 discriminator accomplishes this, despite the small duty cycle, which may be less than  $10^{-4}$ . Gating is introduced to minimize the effect of thermal drift in the discriminator triodes. The duty cycle is extremely short, despite the pulse stretching to approximately 0.1 microsecond which occurs in the amplifier. The time of active information utilization is so small as to be seriously affected by minute but continuous drift in contact potential due to fluctuation in heater voltage.

Intrinsically, the active-to-inactive time ratio for the a-f-c system is approximately  $1.5 \times 10^{-3}$ . Provision is therefore made to gate the discriminator with the broad pulse used to excite the thyratron which drives the magnetron pulser. The latter pulse is approximately 0.3 microsecond wide; hence the active-to-inactive time ratio is increased to  $330 \times 10^{-3}$ , resulting in a marked improvement in stability.

Referring again to Figure 3, the integrating discriminator is followed by a double-triode differential amplifier. This improves the ratio of the desired frequency-drift-signal component to the undesired amplitude-variation component, and provides at least 100 volts of correcting voltage to the klystron local oscillator. As mentioned previously, this correcting voltage may be utilized in any of the well known reactance-tube, voltage-sensitive-capacitor, or other electronic frequency-control means.

#### DUAL-FREQUENCY AMPLIFIER

The advantages of using a dual-frequency narrow-band amplifier instead of a very-wide-band amplifier for ultra-short-pulse a-f-c systems have been described. Means used in the past have included separate upper-sideband and lower-sideband amplifiers with complex a-f-c feedback means provided to maintain their relative gain constant with voltage drift and tube aging. It was theorized that if both channels were driven by the same tube, any change in tube gain would affect both channels simultaneously. This would produce a slight change in sensitivity but no differential output (error signal) between channels.

Separate parallel-tuned circuits connected in series produce asymmetrical band-pass and between-band rejection characteristics, and therefore were only briefly considered. The technique which seemed to have greatest promise was the use of sequential stages of over-coupled double-tuned circuits of proper coupling ( $K$ ) and damping ( $Q$ ) to produce the desired band separation and bandwidth. Such a circuit is shown in Figure 4. In this figure, a transformer-coupled

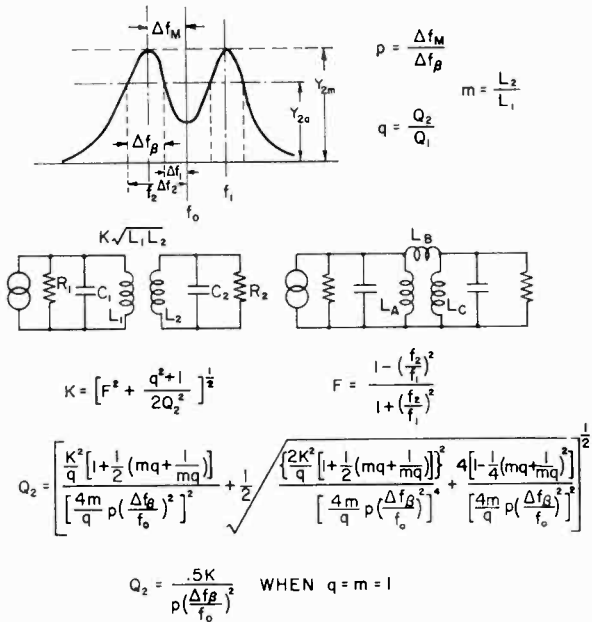


Fig. 4—Design parameters of dual-frequency amplifier.

double-tuned circuit is shown at the left and its equivalent  $\pi$  network at the right. The latter was used in the physical embodiment of this system because of the ease of alignment. The figure also shows an overcoupled bandpass characteristic showing the important parameters required in the design of a dual-channel amplifier driven by a single amplifier tube. The known parameters are  $p$  and  $m$  as illustrated in Figure 4.

#### REQUIRED PARAMETERS

The quantities  $q$ ,  $K$ , and  $Q_2$  are shown in Figure 4. If we make the simplifying assumption that  $q = m = 1$ , then the expression for

$Q_2$  reduces to

$$Q_2 = \frac{0.5K}{p \left( \frac{\Delta f_B}{f_0} \right)^2}$$

This serves as a start for the design since the input and output circuit capacitances may be almost alike and, as shown in Figure 5, there is an advantage in using approximately equal  $Q$ 's as far as peak-to-valley response is concerned.

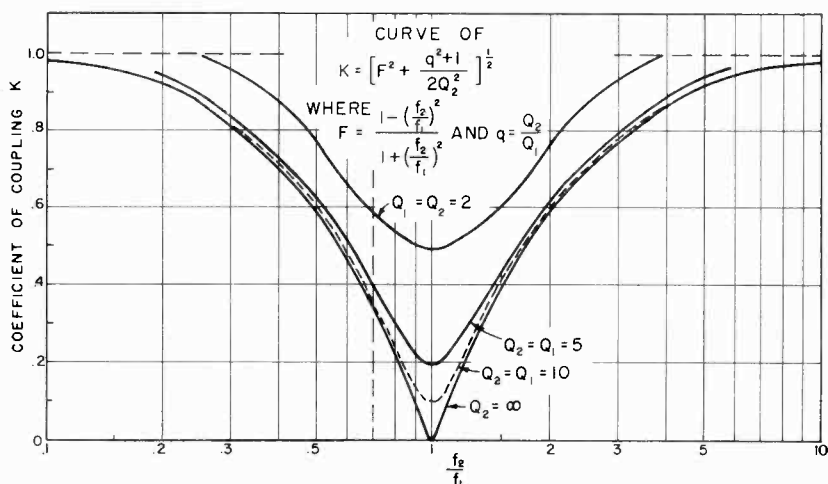


Fig. 5—Variation of the coupling coefficient as a function of the ratio of the center frequency of the upper and lower channels.

Figure 5 shows curves of the coefficient of coupling,  $K$ , versus the ratio of upper- and lower-channel center frequencies,  $f_2/f_1$ . These curves include values from  $Q = 2$  to  $Q = \infty$ , but under the assumption that primary and secondary  $Q$ 's are identical. This has been done for simplicity and because identical  $Q$ 's produce the best peak-to-valley ratio in a coupled circuit. The actual curves of  $K$  for  $Q$  ratios different from 1 do not depart materially from the curves shown in Figure 5, particularly for  $Q$ 's greater than 5. It is evident that for  $Q$ 's greater than this value, the required  $K$  is essentially independent of  $Q$ . For example at  $f_2/f_1 = 200/140 = 1.42$ ,  $K_{Q=\infty} = .38$  and  $K_{Q=5} = .44$ . These relationships for  $Q$  and  $K$  are derived in Appendix I.

The actual  $Q$  ratio used was less than 1 so as to simplify the alignment procedure. When primary and secondary  $Q$ 's are different, a

symmetrical response can be more easily attained because the cause of dissymmetry of peaks can be more easily detected if it is known beforehand whether the damping resides in the primary or secondary. Such a difference in  $Q$  was achieved by loading the secondary with a physical resistor in addition to the input loading of the 6AK5 tubes, because the input loading of the 6AK5 increases with frequency according to the relation

$$G_{\text{input}} = \omega^2 G_m (L_c C_{gk} + KT^2),$$

where  $L_c$  = cathode lead inductance,

$C_{gk}$  = grid cathode capacitance,

$KT^2$  = transit time loading.

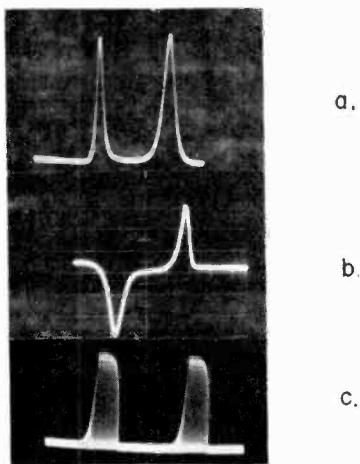
This reduced the high-frequency peak output despite the fixed resistive input circuit loading. By partially bypassing the fixed cathode resistor with a small variable capacitor, equalization of the low- and high-frequency peaks was attained. Some stagger tuning was utilized between stages to attain an over-all 10-megacycle bandwidth in each channel. Appendix I gives the relationships for the circuit parameters of the double-tuned transformer circuit.

Figure 6a shows an oscillogram of the amplitude-versus-frequency response of the dual-channel amplifier. The two pass bands are equal in width although they appear to be unequal because of the nonlinear horizontal scan of the oscilloscope. Point-by-point measurement indicates equal bandwidths of 10 megacycles at the 3-decibel-down points. The over-all amplifier circuit is shown at the left of Figure 7. Here  $V_1$  through  $V_6$  are 6AK5 pentodes. The  $\pi$  section interstages are seen to be single loaded to attain optimum gain-bandwidth and to simplify alignment. The dual-channel amplifier gain is approximately 45 decibels measured with a 450-ohm source which approximates the a-f-c crystal impedance.

#### *Gated Discriminator*

The gated-discriminator schematic circuit is shown in Figure 7. It consists of a dual-frequency transformer wound on a long ferrite rod to allow coupling of the primary circuit which is tuned to 170 megacycles to two secondaries, one tuned to 140 megacycles and the other to 200 megacycles. A 12AX7 double triode operates as a plate detector with an integrating circuit as a plate load. The amplitude-frequency characteristic is shown in the oscillogram of Figure 6b measured at the plate, with the integrating circuit removed. Balance

is obtained by adjustment of the relative grid bias of the two sections of the 12AX7. As described previously, pulse gating is applied to the cathode circuit to improve the signal-to-channel drift ratio. A pair of crystal diodes,  $CR_1$  and  $CR_2$  shape the gating pulse for optimum



- a. DUAL FREQUENCY  
AMPLIFIER RESPONSE.
- b. DISCRIMINATOR OUTPUT  
RESPONSE—NO INTEGRATION.
- c. DISCRIMINATOR OUTPUT  
WITH ADDITION OF GATING  
PULSE FOR STEADY STATE  
INPUT.

Fig. 6—Oscillograms of waveforms.

gating. The effectiveness of gating is shown in Figure 6c. An interesting phenomenon was observed at the low quiescent plate currents used in the discriminator 12AX7. It was noted that for some 12AX7's the grid voltage lost control of the plate current for currents of the order of 50 microamperes or less. This was found to be caused by stray electrons from the base of the cathode passing from cathode to anode around the bottom of the grid. If the heater temperature were reduced so that the emission velocity was too low to allow the electrons to curve around the bottom of the grid, the tube could be cut off. A redesign of the 12AX7 to completely envelop the cathode by the grid should eliminate this trouble. A heater voltage of five volts was used on the 12AX7 heater with excellent results.

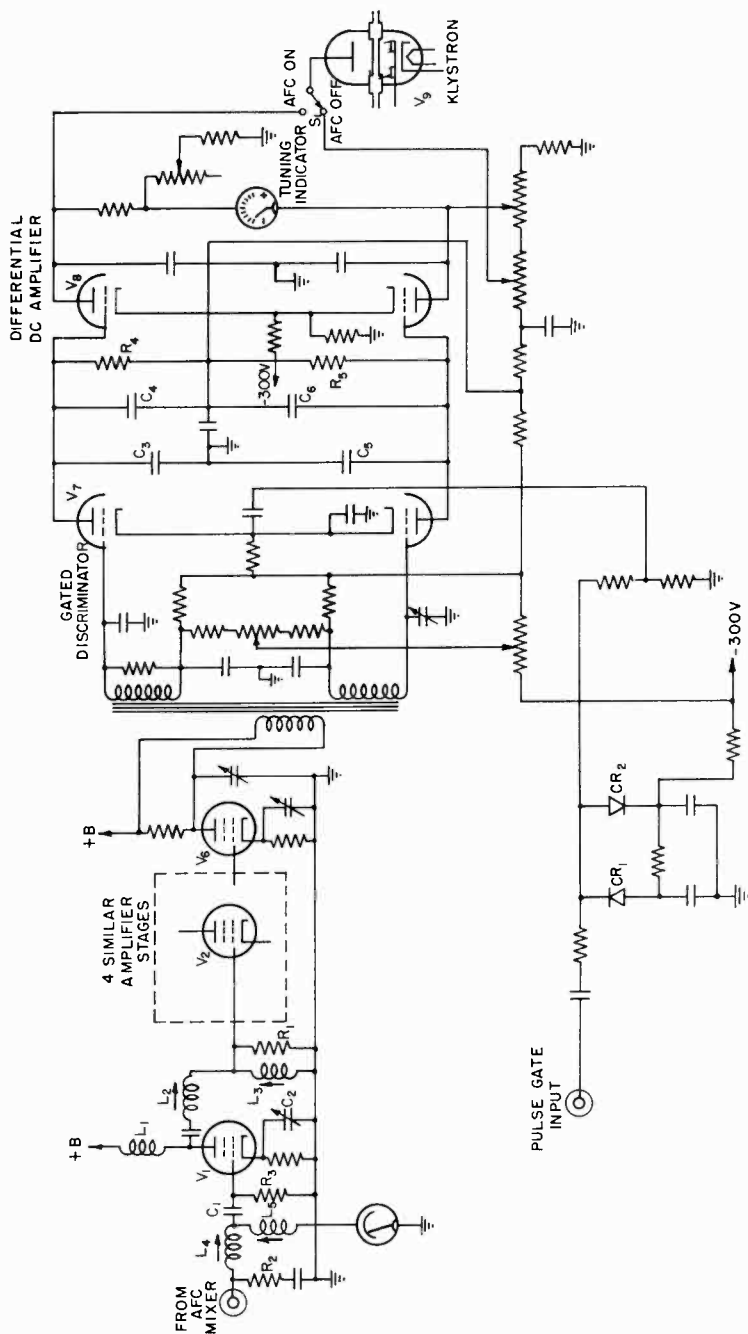


Fig. 7—Spectrum-selection automatic-frequency-control circuit.

### Differential Amplifier

The discriminator described in the previous section feeds a differential d-c amplifier to attain greater sensitivity for true frequency drift signals while reducing the effect of amplitude changes in the input signals at the correct frequency. The schematic circuit is shown at the right of Figure 7 in which  $V_8$  is a 12AX7; a microammeter which measures the amplitude and direction of current flow is used as a fine-tuning indicator when the servo loop is opened by switch  $S_1$ .

Figure 8 shows the equivalent circuit of the differential amplifier; Appendix II gives the pertinent relationships for gain and balance

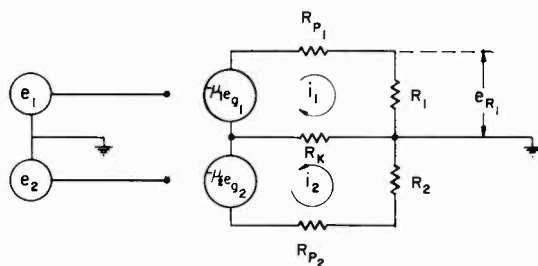


Fig. 8—Equivalent circuit of differential amplifier.

ratio which is the ratio of out-of-phase gain over the in-phase gain. The balance ratio is a measure of output voltage caused by a change in frequency divided by the output voltage caused by a change in amplitude.

The output voltage  $e'_{R_1}$  and the balance ratio  $\beta$  for the equivalent circuit of Figure 8 are derived in Appendix II.

For identical sections of the 12AX7,  $\mu_1 = \mu_2$  and  $R_{p_1} = R_{p_2}$ . Then

$$\beta = 1 + \frac{2R_k(\mu+1)}{R_p + R_2}$$

This is seen to be a maximum when  $R_2 = 0$ ;

$$\beta_{\max} = 1 + \frac{2R_k(\mu+1)}{R_p} \approx 2G_m R_k$$

This relationship is shown in Figure 9 which is a plot of  $\beta$  versus  $R_2$ . For the parameters used in the experimental system,

$$\beta_{\max} = 400,$$

out-of-phase (desired) gain = 200,

in-phase (undesired) gain = 1/2.

Actual measured values of  $\beta$  were in the neighborhood of 100 primarily because the two halves of the 12AX7 triodes were not well enough matched and only selected tubes would allow match over a wide range

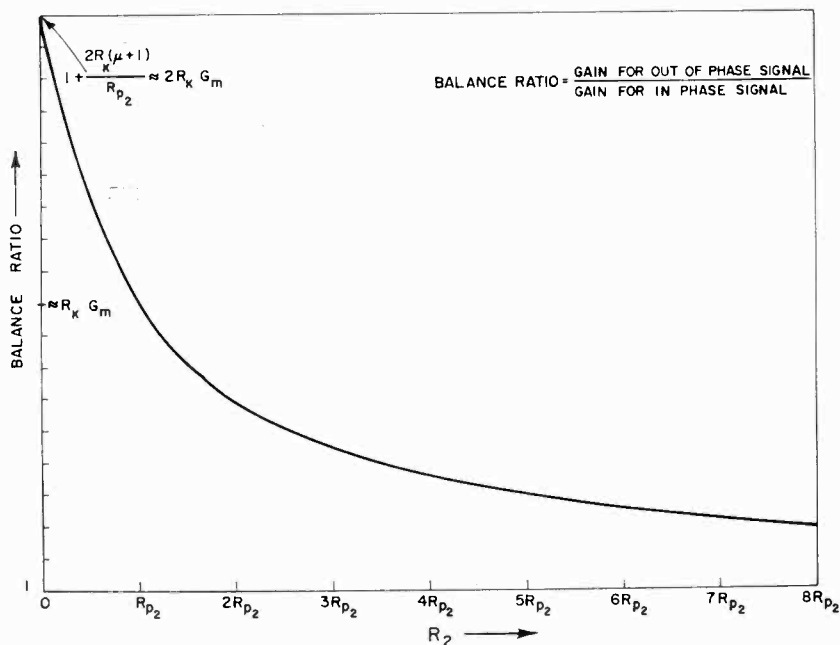


Fig. 9—Curve of balance ratio versus  $R_2$ .

of operating conditions. It would indeed be desirable to have low-current, high- $\mu$  dual triodes which are controlled in  $R_p$ ,  $\mu$ , and transfer characteristic over the entire dynamic range of grid voltages. Since, however, there is also in-phase degeneration in the discriminator section of the system due to the common cathode resistor, the combined effect provides adequate "limiting" against amplitude variation of input signals which in an a-f-c system are quite constant.

Figure 10 is a photograph of the experimental chassis. The six-stage dual-channel amplifier is at the right-hand side of the chassis and illustrates the extensive use of feedthrough capacitor filtering, heater chokes, the  $\pi$  interstage inductors, and cathode circuit compensation. This is followed by the balanced discriminator with its ferrite-

cored transformer, and finally the differential amplifier section. The 90-ohm cable shown on the top view of the chassis brings gating pulses to the discriminator-tube cathode from the pulser as described previously.

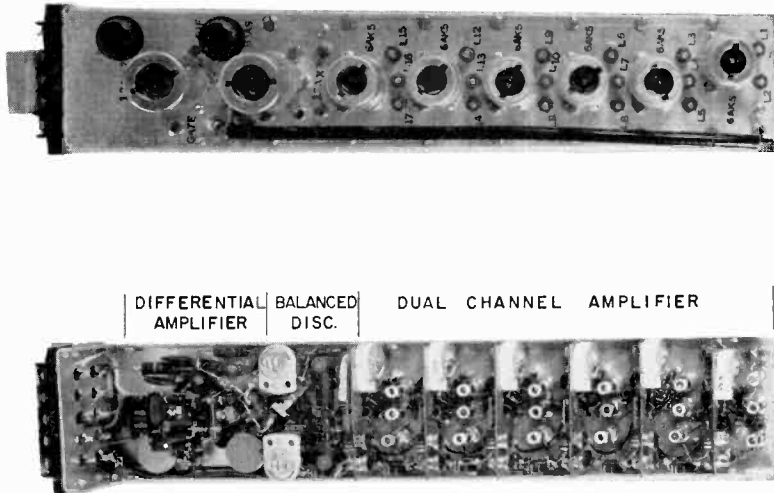


Fig. 10—Experimental spectrum-selection automatic-frequency-control chassis.

### CONCLUSION

This paper describes an experimental automatic-frequency-control system useful for correction of frequency drift in ultra-short-pulse amplitude systems which have sidebands up to 100 megacycles on each side of the carrier. This has been designated as a spectrum-selection automatic-frequency-control system because of the use of selected sidebands of the pulse-amplitude-modulated waveform to determine the position of the carrier within the spectrum. The system includes a novel six-stage dual-channel amplifier whose pass bands are 10 megacycles wide and so spaced above and below the 170-megacycle intermediate frequency as to optimize the rate of change of spectrum energy with change in frequency. This occurs at 140 megacycles and 200 megacycles for the 0.01-microsecond cosine-shaped pulse used in the system. Because of the low gain per stage, standard techniques using the miniature 6AK5 pentodes would provide insufficient gain to make the system operative. In addition, a pulse-gated balanced discriminator and differential amplifier have been developed which insure adequate gain and drift stability and provide 100 volts of correction

voltage suitable for servoing a microwave klystron. This amplifier may be driven from a single-ended or balanced crystal mixer or utilized without mixing in a pulsed 170-megacycle carrier system. The measured amplifier gain for a steady-state signal is 45 decibels in each channel. The servo gain is approximately 14, for a 0.01-microsecond cosine-shaped pulse-modulated carrier using a single-ended crystal mixer with a 10-decibel conversion loss and feeding the spectrum selection a-f-c into a microwave klystron. For a balanced mixer under similar conditions, the servo gain is well over 40. With the servo loop opened, the a-f-c served advantageously as a klystron tuning indicator. Although this paper deals with the use of the system for control of a microwave klystron, it may also advantageously be applied to other ultra-short-pulse modulated systems where carrier-frequency control may be necessary.

#### APPENDIX I—DUAL-CHANNEL AMPLIFIER DERIVATIONS

Let  $N = Y_{2a}/Y_{2m}$  be the ratio of the response at any frequency  $f_a$ , to the response at  $f_m$ , the frequency of peak response (see Figure 4). The value of  $N$  can be derived from  $Y$  as given by Aiken;<sup>1</sup>

$$N = \frac{Y_{2a}}{Y_{2m}} = \frac{2S}{\sqrt{(1+S^2)^2 - 2v^2 \left( S^2 - \frac{b}{2} \right) + v^4}} \cdot \frac{2S}{\sqrt{(1+S^2)^2 - \left( S^2 - \frac{b}{2} \right)^2}}$$

where

$$v = \sqrt{Q_1 Q_2} \left[ \frac{f}{f_0} - \frac{f_0}{f} \right] \equiv \frac{2\Delta f}{f_0} \sqrt{Q_1 Q_2}$$

$$S = K \sqrt{Q_1 Q_2}$$

$$b = \frac{Q_2}{Q_1} + \frac{Q_1}{Q_2}$$

and  $K$  is the coefficient of coupling.

<sup>1</sup>C. B. Aiken, "Two Mesh Tuned Coupled Circuit Filters," *Proc. I.R.E.*, Vol. 25, p. 230, February, 1937.

Solving for  $v^2$ ,

$$v^2 = (S^2 - b/2) \left\{ 1 \pm \sqrt{\left[ \frac{1 - N^2}{N^2} \right] \left[ \frac{(1 + S^2)^2}{(S^2 - b/2)^2} - 1 \right]} \right\} \quad (1)$$

The value of  $N^2$  of interest is the 3-decibel-down response where

$$N^2 = 1/2 \text{ and } \frac{1 - N^2}{N^2} = 1.$$

$$v_1^2 = (S^2 - b/2) \left\{ 1 + \sqrt{\left[ \frac{1 + S^2}{S^2 - b/2} \right]^2 - 1} \right\} \quad (2)$$

$$v_2^2 = (S^2 - b/2) \left\{ 1 - \sqrt{\left[ \frac{1 + S^2}{S^2 - b/2} \right]^2 - 1} \right\}. \quad (3)$$

Since  $v_1^2 - v_2^2 = 2(v_1 - v_2) \frac{(v_1 + v_2)}{2}$  and  $(v_1 + v_2)/2 = v_m$ , the value of  $v$  at the peak response assuming arithmetic symmetry,

$$v_1 - v_2 = \frac{1}{v_m} \sqrt{(1 + 2S^2 - b/2)(1 + b/2)} \quad (4)$$

$$v_1 - v_2 = \frac{2}{f_0} \sqrt{Q_1 Q_2} [\Delta f_1 - \Delta f_2], \quad (5)$$

where  $\Delta f_1 - \Delta f_2 =$  actual bandwidth,  $f_0 =$  frequency of i-f (valley). From the above relationships, the values  $Q_1$  and  $Q_2$  which give the required bandwidth are found. Since, however, the primary and secondary  $L$ 's and  $C$ 's are not equal, we must substitute

$$V_1 = v_1 \sqrt{m}, \quad V_2 = v_2 \sqrt{m}, \quad \text{and } Q_2 = qQ_1.$$

Then 
$$B = \frac{mQ_2}{Q_1} + \frac{Q_1}{mQ_2} = mq + \frac{1}{mq}, \quad S = \frac{KQ_2}{\sqrt{q}}.$$

$$V_1 - V_2 = 2 \frac{\sqrt{m}}{f_0} \sqrt{Q_1 Q_2} \underbrace{[\Delta f_1 - \Delta f_2]}_{\Delta f_B} = 2 \frac{\sqrt{m} \Delta f_B Q_2}{f_0 \sqrt{q}} \quad (6)$$

$$V_1 - V_2 = \frac{1}{V_m} \sqrt{(1 + 2S^2 - B/2)(1 + B/2)} \quad (7)$$

$$V_m = \frac{2Q_2 \sqrt{m} \Delta f_m}{f_0 \sqrt{q}}, \quad (8)$$

where  $m$ ,  $q$ , and  $\Delta f_\beta$  are defined in Figure 4.

Combining Equations (6) and (7),

$$\frac{4Q_2^2 m \Delta f_\beta \Delta f_m}{f_0^2 q} = \sqrt{\left[ 1 + 2 \frac{K^2 Q_2^2}{q} - 1/2 \left( mq + \frac{1}{mq} \right) \right] \left[ 1 + \frac{1}{2} \left( mq + \frac{1}{mq} \right) \right]}, \quad (9)$$

Solving for  $Q_2$  and letting  $p = \frac{\Delta f_m}{\Delta f_\beta}$ ,

$$Q_2 = \frac{\left[ \frac{K^2}{q} \left[ 1 + \frac{1}{2} \left( mq + \frac{1}{mq} \right) \right] \right]}{\left[ \frac{4m}{q} p \left( \frac{\Delta f_\beta}{f_0} \right)^2 \right]^2} + \frac{1}{2} \sqrt{\frac{\left[ \frac{2K^2}{q} \left\{ 1 + \frac{1}{2} \left( mq + \frac{1}{mq} \right) \right\} \right]^2}{\left[ \frac{4m}{q} p \left( \frac{\Delta f_\beta}{f_0} \right)^2 \right]^2} + \frac{4 \left[ 1 - \frac{1}{4} \left( mq + \frac{1}{mq} \right)^2 \right]}{\left[ \frac{4m}{q} p \left( \frac{\Delta f_\beta}{f_0} \right)^2 \right]^2}} \right)^{1/2} \quad (10)$$

When  $q = m = 1$ .

$$Q_2 = \frac{.5K}{p \left( \frac{\Delta f_\beta}{f_0} \right)^2}. \quad (11)$$

For values of  $m$  and  $q$  between  $1/2$  and 1, the second term under the radical is insignificant and

$$Q_2 \approx \frac{K \sqrt{2/q \left[ 1 + \frac{1}{2} \left( mq + \frac{1}{mq} \right) \right]}}{4 \frac{m}{q} p \left( \frac{\Delta f_\beta}{f_0} \right)^2}$$

For a single stage, 
$$\frac{\Delta f_\beta}{f_0} = \frac{15 \text{ mc}}{170 \text{ mc}} = .088, \quad (12)$$

$$K = .4,$$

and 
$$p = \frac{\Delta f_m}{\Delta f_\beta} = \frac{30 \text{ mc}}{15 \text{ mc}} = 2;$$

the following values were calculated:

$$Q_2 = Q_1 = 13 \text{ for } m = q = 1$$

$$Q_2 = Q_1 = 27 \text{ for } m = 1/2, q = 1$$

$$Q_2 = 23, Q_1 = 46 \text{ for } m = q = 1/2$$

$$Q_2 = 9.5, Q_1 = 19 \text{ for } m = 1, q = 1/2.$$

#### APPENDIX II—DERIVATION OF DIFFERENTIAL-AMPLIFIER PARAMETERS

Referring to Figure 8,

$$e_{g1} = e_1 - (i_1 + i_2)R_k,$$

$$e_{g2} = e_2 - (i_1 + i_2)R_k,$$

$$\mu_1 e_{g1} = i_1 [R_{p1} + R_1 + R_k] + i_2 R_k$$

$$\mu_1 [e_1 - R_k(i_1 + i_2)] = i_1 [R_{p1} + R_1 + R_k] + (i_2 R_k) \quad (13)$$

$$\mu_2 [e_2 - R_k(i_1 + i_2)] = i_2 [R_{p2} + R_2 + R_k] + (i_1 R_k) \quad (14)$$

From Equations (13) and (14) it can be shown that

$$E_{R_1} \equiv i_1 R_1 = \{ \mu_1 e_1 R_1 [R_{p2} + R_2 + R_k(\mu_2 + 1)] - \mu_2 e_2 R_k R_1 [\mu_1 + 1] \} \{ [R_{p1} + R_1 + R_k(\mu_1 + 1)] [R_{p2} + R_2 + R_k(\mu_2 + 1)] - R_k^2(\mu_1 + 1)(\mu_2 + 1) \}^{-1}$$

The output voltage for a frequency drift  $\Delta f$  is denoted by  $E_{R_1}'$  (i.e.,  $e_1 = -e_2$ ), and the output voltage for an amplitude change  $\Delta e$  is denoted by  $E_{R_1}''$  (i.e.,  $e_1 = e_2$ ).

The balance ratio is given by

$$\beta = \frac{e_{R_1'}}{e_{R_1''}} = \frac{\mu_1 e_1 [R_{p_2} + R_2 + R_k (\mu_2 + 1)] R_1 + \mu_2 e_1 R_k R_1 (\mu_1 + 1)}{\mu_1 e_1 [R_{p_2} + R_2 + R_k (\mu_2 + 1)] R_1 - \mu_2 e_1 R_k R_1 (\mu_1 + 1)} \quad (15)$$

Assume

$$\mu_1 = \mu_2,$$

$$R_{p_1} = R_{p_2}.$$

$$\beta = \frac{2R_k (\mu + 1)}{R_{p_2} + R_2}, \quad (16)$$

and for  $R_2 = 0$ ,

$$\beta = 2G_m R_k. \quad (17)$$

Equation (16) indicates that for optimum balance ratio  $R_2 = 0$  and  $R_k$  must be large.

The out-of-phase gain,  $G'$ , may be derived for  $R_2 = 0$ ;

$$G' = \frac{e_{R_1'}}{e_1} = \frac{\mu R_1 \left[ 1 + 2 \frac{R_k}{R_p} (\mu + 1) \right]}{(\mu + 1) R_k \left[ 2 + \frac{R_1}{R_p} \right] + R_p + R_1}.$$

The in-phase gain,  $G''$ , may be similarly derived;

$$G'' = \frac{e_{R_1''}}{e_1} = \frac{\mu R_1}{(\mu + 1) R_k \left[ 2 + \frac{R_1}{R_p} \right] + R_p + R_1}.$$

If  $R_1 \gg R_p$ ,  $R_k \cong R_p$ , and  $\mu \gg 1$ ,  $G' \approx 2\mu$  and  $G'' = R_p/R_k$ . For the parameter values used in the experimental system as shown,

$$R_p = 60,000 \text{ ohms} \quad \mu = 100$$

$$R_1 = 1.8 \text{ megohms} \quad G' = 200$$

$$R_k = 150,000 \text{ ohms} \quad G'' = \frac{1}{2}$$

$$R_2 = 0 \quad \beta = 400$$

## RCA TECHNICAL PAPERS†

Second Quarter, 1959

Any request for copies of papers listed herein should be addressed to the publication to which credited.

"Design and Build an Anechoic Chamber," R. F. Kolar, <i>Electronic Industries</i> (April) .....	1959
"Distribution of Cations in Spinels," A. Miller, <i>Jour. Appl. Phys.</i> (April) .....	1959
"Electronics Guides Your Car," V. K. Zvorykin and L. E. Flory, <i>Radio-Electronics</i> (April) .....	1959
"An Improved Vidicon Focusing-Deflecting Unit," J. Castleberry and B. H. Vine, <i>Jour. S.M.P.T.E.</i> (April) .....	1959
"Investigation of the Electrochemical Characteristics of Organic Compounds—III Nitroalkanes," R. Glicksman and C. K. Morehouse, <i>Jour. Electrochem. Soc.</i> (April) .....	1959
"New Electronic Equipment for Small Boats Introduced by RCA," C. E. Keenan, <i>Wire and Radio Communications</i> (April) .....	1959
"On the Origin of Low Moments in Chromium-Containing Spinels," P. K. Baltzer and P. J. Wojtowicz, <i>Jour. Appl. Phys.</i> (April) .....	1959
"Professional Groups—and PG Chapters," E. M. McElwee, <i>IRE Northern New Jersey Newsletter</i> (April) .....	1959
"Random Number Generator Using Subharmonic Oscillators," F. Sterzer, <i>Rev. Sci. Instr.</i> (April) .....	1959
"Some Crystallographic and Magnetic Properties of Square-Loop Materials in Ferrite Systems Containing Copper," A. P. Greifer and W. J. Croft, <i>Jour. Appl. Phys.</i> (April) .....	1959
"Theoretical Model for Cubic-to-Tetragonal Phase Transformations in Transition Metal Spinels," P. J. Wojtowicz, <i>Jour. Appl. Phys.</i> (April) .....	1959
"The Use of Miniature Tubes in Class C Circuits," A. Dzik, <i>Trans. I.R.E. PGVC</i> (April) .....	1959
"An Analog Computer for Finding an Optimum Route Through a Communication Network," H. Rapaport and P. Abramson, <i>Trans. I.R.E. PGCS</i> (May) .....	1959
"Analysis of SSB Power Amplifiers," F. Assadourian, <i>Trans. I.R.E. PGCS</i> (May) .....	1959
"The Electron Microscope," F. J. Herrmann, <i>I.R.E. Student Quarterly</i> (May) .....	1959
"Graphical Solution for High-Frequency Electrostatic Deflection," M. H. Greenblatt, <i>Amer. Jour. Phys.</i> (May) .....	1959
"Hold Range and Pulse Interference Immunity of Triggered Deflection Oscillators for Television Receivers," E. Luedicke, <i>Trans. I.R.E. PGBTR</i> (May) .....	1959
"Long Distance V.H.F. Reception," J. E. le B. Terry, <i>Wireless World</i> (May) (Letter to the Editor) .....	1959
"Lowry Air Force Base Uses Stereo TV System for Training Technicians," P. A. Greenmeyer, <i>Signal</i> (May) .....	1959
"Micromodules Make Their Bow," J. W. Knoll and H. J. Laiming, <i>Astronautics</i> (May) .....	1959
"A New Technique for Measuring Transistor Switching Times," R. R. Johnson, R. D. Lohman, and R. R. Painter, <i>Semiconductor Products</i> (May) .....	1959

† Report all corrections or additions to *RCA Review*, RCA Laboratories, Princeton, N. J.

- "Performance Analysis of a Data Link System," A. B. Glenn, *Trans. I.R.E. PGCS* (May) ..... 1959
- "The Performance of Zinc, Magnesium, and Aluminum Primary Cell Anodes—A Review," R. Glicksman, *Jour. Electrochem. Soc.* (May) ..... 1959
- "Reduced Delayed Neutron Group Representations," R. E. Skinner and Co-author, *Nuclear Science and Engineering* (May) ..... 1959
- "The Transformation of Electronic Communications," E. W. Engstrom, *Elec. Eng.* (May) ..... 1959
- "Simplification of Viewer Brightness and Contrast Controls on Color TV Receivers," L. L. Burns, R. W. Ahrons, and L. B. Johnston, *Trans. I.R.E. PGBTR* (May) ..... 1959
- "The Usefulness of Transconductance as a Transistor Parameter," J. F. Cashen and A. Harel, *Proc. I.R.E.* (May) (Letter to the Editor) ..... 1959
- "Role of Single Phonon Emission in Low-Field Breakdown of Semiconductors at Low Temperatures," M. A. Lampert, F. Herman, and M. C. Steele, *Phys. Rev. Letters* (May 1) ..... 1959
- "Transistors Simplify Control of Target Drone," G. B. Herzog, *Electronics* (May 1) ..... 1959
- "Transistor Dual Conversion for Marker-Beacon Receivers," R. G. Erdmann, *Electronics* (May 8) ..... 1959
- "Two-Element Matching Network Nomograph," H. B. Yin, *Electronic Design* (May 13) ..... 1959
- "Synthesizing Timbre for Electronic Musical Tones," W. S. Pike and C. N. Hoyler, *Electronics* (May 29) ..... 1959
- "Analysis of a Four-Terminal Parametric Amplifier," K. K. N. Chang, *RCA Review* (June) ..... 1959
- "Automatic Light Control for Color and Monochrome Vidicon Film Cameras," W. L. Hurford, W. J. Neely, and A. Reisz, *Broadcast News* (June) ..... 1959
- "Bibliography of Digital Magnetic Circuits and Materials," W. L. Morgan, *Trans. I.R.E. PGEC* (June) ..... 1959
- "Design Plan for Forced-Air Cooling," T. C. Reeves, *Electrical Manufacturing* (June) ..... 1959
- "Drift Velocity Saturation in p-Type Germanium," R. D. Larrabee, *Jour. Appl. Phys.* (June) ..... 1959
- "The Effect of Several Variables on Phosphor-Dot Size in Color Picture Tubes," N. R. Goldstein, *RCA Review* (June) ..... 1959
- "Evaluation of a Modulated Air-Flow Loudspeaker," A. L. Witchey and Co-authors, *Jour. Acous. Soc. Amer.* (June) ..... 1959
- "Experimental Results With the Panel X-Ray Amplifier," B. Kazan and Co-author, *Radiology* (June) ..... 1959
- "5-Band Mobile Transmitter," G. D. Hanchett, *RCA Ham Tips* (June) ..... 1959
- "On the Growth of Gallium Arsenide Crystals from the Melt," S. G. Ellis, *Jour. Appl. Phys.* (June) (Letter to the Editor) ..... 1959
- "Integrated Devices Using Direct-Coupled Unipolar Transistor Logic," J. T. Wallmark and S. M. Marcus, *Trans. I.R.E. PGEC* (June) ..... 1959
- "Introduction to Junction Transistors, Part III," R. N. Hurst, *Broadcast News* (June) ..... 1959
- "Making a Multiplant Supplier Rating System Produce," P. J. Goldin, *Trans. I.R.E. PGRQC* (June) ..... 1959
- "Microwave Propagation over Rough Surfaces," M. P. Bachynski, *RCA Review* (June) ..... 1959
- "The Need for Revision of Transistor Terminology and Notation," B. E. Keiser, *Proc. I.R.E.* (June) (Letter to the Editor) ..... 1959
- "Polarity of Gallium Arsenide Single Crystals," J. G. White and W. C. Roth, *Jour. Appl. Phys.* (June) (Letter to the Editor) ..... 1959
- "Pretesting of 8-Hop, 243-Mile Microwave System Demonstrates Capabilities of TVM-1A Equipment," J. S. Bullock, V. S. Mattison, and J. H. Roe, *Broadcast News* (June) ..... 1959

- "Principles of Operation of the Ampliphase Transmitter," A. M. Miller and J. Novik, *Broadcast News* (June) . . . . . 1959
- "The Propagation of Perturbations along Magnetically Focused Electron Beams," F. Paschke, *RCA Review* (June) . . . . . 1959
- "Proposed Impedance Requirements for Television Antenna Systems," D. W. Peterson, *Broadcast News* (June) . . . . . 1959
- "Pulse Amplification Using Impact Ionization in Germanium," M. C. Steele, L. Pensak, and R. D. Gold, *Proc. I.R.E.* (June) . . . . . 1959
- "Pulsed Measurement of the Variation of Thermal Conductivity of Germanium with Temperature," J. I. Pankove, *Rev. Sci. Instr.* (June) (Notes) . . . . . 1959
- "Quality-Control Determinations of the Screen Persistence of Color Picture Tubes," J. M. Forman and G. P. Kirkpatrick, *RCA Review* (June) . . . . . 1959
- "Reduction of Co-Channel Interference by Precise Frequency Control of Television Picture Carriers," W. L. Behrend, *RCA Review* (June) . . . . . 1959
- "Semiconductor Diodes in Parametric Subharmonic Oscillators," J. Hilibrand and W. R. Beam, *RCA Review* (June) . . . . . 1959
- "Stabilization of Transistor Gain over Wide Temperature Ranges," R. A. Schmeltzer, *RCA Review* (June) . . . . . 1959
- "Surface-Immune Transistor Structure," H. Nelson, *RCA Review* (June) . . . . . 1959
- "Thermionic Emitters," L. S. Nergaard, *RCA Review* (June) . . . . . 1959
- "Plasma Pinch Effects in Indium Antimonide," M. Glicksman and M. C. Steele, *Phys. Rev. Letters* (June 1) . . . . . 1959
- "Designing High-Quality A-F Transistor Amplifiers," R. Minton, *Electronics* (June 12) . . . . . 1959
- "Voltage Tunable Millimeter-Wave Oscillators," D. J. Blattner and F. Sterzer, *Electronics* (June 19) . . . . . 1959
- "Semiconductor Devices for Microminiaturization," J. T. Wallmark and S. M. Marcus, *Electronics* (June 26) . . . . . 1959
- "The Development of Automatic Machinery for Making Electron-Tube Stems," M. M. Bell, *I.R.E. Convention Record, Part 6, Component Parts, Industrial Electronics, Production Techniques, Reliability and Quality Control, Ultrasonics Engineering* . . . . . 1959
- "Fast Microwave Logic Circuits," D. J. Blattner and F. Sterzer, *I.R.E. Convention Record, Part 4, Automatic Control, Electronic Computers, Information Theory* . . . . . 1959
- "A Five-Transistor Automobile Receiver Employing Drift Transistors," R. A. Santilli and C. F. Wheatley, *I.R.E. Convention Record, Part 7, Audio, Broadcast and Television Receivers, Broadcasting* . . . . . 1959
- "FM Carrier Techniques in the RCA Color Video Tape Recorder," R. D. Thompson, *I.R.E. Convention Record, Part 7, Audio, Broadcast and Television Receivers, Broadcasting* . . . . . 1959
- "Improvement in Detection, Gain-Control, and Audio-Driven Circuits of Transistorized Broadcast-Band Receivers," D. Thorne and R. V. Fournier, *I.R.E. Convention Record, Part 7, Audio, Broadcast and Television Receivers, Broadcasting* . . . . . 1959
- "Industrial Electronics — The Growing Servant of Mankind," T. A. Smith, *I.R.E. Convention Record, Part 6, Component Parts, Industrial Electronics, Production Techniques, Reliability and Quality Control, Ultrasonics Engineering* . . . . . 1959
- "A Minimum Distortion Tapered-Transmission-Line Transformer for Pulse Application," H. Amemija, *I.R.E. Convention Record, Part 2, Circuit Theory* . . . . . 1959
- "A New Approach to Low Distortion in a Transistor Power Amplifier," H. J. Paz, *I.R.E. Convention Record, Part 7, Audio, Broadcast and Television Receivers, Broadcasting* . . . . . 1959
- "Noise Figure of Receiver Systems Using Parametric Amplifiers," J. Sie and S. Weisbaum, *I.R.E. Convention Record, Part 3, Electron Devices, Microwave Theory and Techniques* . . . . . 1959

- "The 'Null Method' of Azimuth Alignment in Multitrack Magnetic Tape Recording," A. G. Evans, *I.R.E. Convention Record, Part 7, Audio, Broadcast and Television Receivers, Broadcasting* . . . 1959
- "An Orbit Program for Engineering Use," B. H. Bloom and H. R. Smith, *I.R.E. Convention Record, Part 5, Aeronautical and Navigational Electronics, Military Electronics, Space Electronics and Telemetry* . . . . . 1959
- "Recent Advances in Medical Electronics," V. K. Zworykin, *I.R.E. Convention Record, Part 9, Human Factors in Electronics, Instrumentation, Medical Electronics, Nuclear Science* . . . . . 1959
- "A Simple and Flexible Method of Fabricating Diffused N-P-N Silicon Power Transistors," L. D. Armstrong and H. D. Harmon, *I.R.E. Convention Record, Part 3, Electron Devices, Microwave Theory and Techniques* . . . . . 1959
- "Sputnik II as Observed by C-Band Radar," D. K. Barton, *I.R.E. Convention Record, Part 5, Aeronautical and Navigational Electronics, Military Electronics, Space Electronics and Telemetry* . . . . . 1959
- "Transistorized Video Switching," C. R. Monroe, J. W. Wentworth, and A. C. Luther, Jr., *I.R.E. Convention Record, Part 7, Audio, Broadcast and Television Receivers, Broadcasting* . . . . . 1959

## AUTHORS



DONALD J. BLATTNER received the BS degree in Electrical Engineering in 1946 and the M.A. degree in Physics in 1949 from Columbia University. He was a teaching assistant and lecturer in physics at Columbia while doing research in the solid-state laboratory from 1949 to 1953. Joining RCA Laboratories in 1953, he engaged in fundamental research on origins of noise in beam-type electron tubes, and in the design, construction, and testing of experimental traveling-wave tubes. In 1955 he transferred to the Electron Tube Division, where he developed millimeter-wave oscillators, electrostatically focused traveling-wave tubes, microwave techniques for high-speed computers, and solid-state parametric amplifiers. Mr. Blattner rejoined RCA Laboratories in 1959 to work on problems in telecommunication systems. He is a member of Sigma Xi and a Senior Member of the Institute of Radio Engineers.

GEORGE H. BROWN received the B.S. degree at the University of Wisconsin in 1930, the degree of M.S. in 1931, the Ph.D. degree in 1933, and the professional degree of Electrical Engineering in 1942. From 1930 until 1933 he was a Research Fellow in the Electrical Engineering Department at the University of Wisconsin; from 1933 until 1942 he was in the Research Division of the RCA Manufacturing Company at Camden, N. J.; from 1942 until 1952 he was a research engineer at the RCA Laboratories, Princeton, N. J.; from 1952 until 1957 he was Director of the Systems Research Laboratory, RCA Laboratories; from January 1957 until June 1957 he was Chief Engineer, Commercial Electronic Products, Radio Corporation of America, Camden, N. J.; from June 1957 until March 1959 he was Chief Engineer, Industrial Electronic Products, Radio Corporation of America, Camden. In March 1959, he was appointed Vice President, Engineering, Radio Corporation of America. Dr. Brown is a member of Sigma Xi, the New York Academy of Sciences, the Franklin Institute, and the Society of Motion Picture and Television Engineers and a Fellow of the Institute of Radio Engineers, the American Association for the Advancement of Science, and the American Institute of Electrical Engineers.



C. LOUIS CUCCIA received the B.S. degree in Electrical Engineering in 1941 and M.S. degree in 1942, both from the University of Michigan. From 1941 to 1942, he was also employed as a research engineer for the Fisher Body Division of General Motors. He joined the technical staff of the RCA Laboratories in 1942 and worked on microwave-tube research and development until 1954. From 1954 to 1957, he was assigned to the color television activity of the laboratories specializing in evaluation of new ideas, patenting of new developments, and liaison between the various activities involved in color television receiver production. Early in 1957, he joined the Microwave Design Activity of the Electron Tube Division as Engineering Leader in charge of traveling-wave-tube and backward-wave oscillator design and development. Since January 1959, he has been engaged in planning and analyzing advanced systems utilizing microwave products.



SIDNEY GRAY received the B.S. degree in Meteorology from New York University in 1946, and the Ph.D. degree in Physics from Rutgers University in 1951. In 1951, he was employed by the Atomic Energy Commission, and joined the technical staff at RCA Laboratories later in the same year. As a member of the camera tube group, he participated in the development of the tricolor Vidicon and is presently engaged in the study of high-resolution television pickup tubes. Dr. Gray is a member of Sigma Xi and of the American Physical Society.

WILLIAM A. HARRIS received the B.S. degree in Electrical Engineering from Rose Polytechnic Institute, Terra Haute, Indiana, in 1927. He was employed by the General Electric Company from 1927 to 1929, and transferred to the RCA Victor Division at Camden, N. J. in 1930. He joined the Electron Tube Division in Harrison, N. J. in 1931. Since 1948 he has been a member of the Receiving Tube Advanced Development activity. Mr. Harris is a Fellow of the Institute of Radio Engineers.



GEORGE H. HEILMEIER received the B.S. degree in Electrical Engineering from the University of Pennsylvania in 1958. Upon graduation he joined the R.C.A. Laboratories as a member of the technical staff in the microwave section of the Electronics Research Laboratory. He is presently doing graduate work at Princeton University. Mr. Heilmeyer is a member of Tau Beta Pi, Sigma Xi, Eta Kappa Nu, the Institute of Radio Engineers, and the American Institute of Electrical Engineers.

W. C. JOHNSON attended St. Peter's College in New Jersey and is presently working toward his B.S. degree at the Newark Technical College of Engineering. He worked for the Peerless Construction Co. in 1950, and Western Electric in 1951 before joining the microwave development group of the RCA Electron Tube Division, Harrison, N.J.

HARRY KIHN (see *RCA Review*, Vol. XX, No. 1, March 1959, p. 186.)



RICHARD J. KLENSCH received the B.S. degree in Electrical Engineering from the University of Illinois in 1951 and is currently working toward his M.S. degree at Princeton University. He was employed by Motorola, Inc., and then joined RCA Laboratories in 1952 where he engaged in millimeter-wave high-resolution radar research. From 1954 to 1956 he was a radar instructor while serving in the U. S. Army. In 1956 he returned to RCA Laboratories where he has been engaged in microwave scanning antenna research and more recently in the field of micro-miniature multiplexing systems. Currently he is doing research in infrared detection systems. Mr. Klensch is an associate member of the Institute of Radio Engineers and is a member of the Professional Group on Antennas, Professional Group on Instrumentation, and Professional Group on Telemetry and Space Electronics.

T. MURAKAMI received the B.S. degree in E.E. from Swarthmore College in 1944, and the M.S. degree from the Moore School of Electrical Engineering, University of Pennsylvania in 1947. From 1944 to 1946 he was an assistant and research associate in the Department of Electrical Engineering at Swarthmore College. Since 1946 he has been with the Advanced Development Section of the RCA Victor Television Division, Camden, N. J., working on radio frequency circuit development. Mr. Murakami is a Senior Member of the Institute of Radio Engineers and a member of Sigma Xi.



WEN YUAN PAN received the E. E. degree in 1939 and Ph.D. in 1940 from Stanford University. He was engaged as a research associate at the Radio Research Laboratory at Harvard University during World War II. Since 1945 he has been with RCA Victor Home Instruments and is now Manager in charge of Signal Processing in Advanced Development Engineering. Dr. Pan served in an advisory capacity to the China Defense and Supplies in 1941, the International Civil Aviation Conference in 1944, and the United Nations Telecommunications Committee in 1946. He is an honorary member of the Veteran Wireless Operators' Association, a member of Sigma Xi, A.O.E., A.A.A.S., A.M.E., and Senior Member of the Institute of Radio Engineers.

RICHARD N. PETERSON received the B.S. degree in Electrical Engineering from Purdue University in 1950 and the M.S. degree from Newark College of Engineering in 1956. He joined the RCA Electron Tube Division at Harrison, N. J. in 1950 as a member of the Receiving-Tube Applications Laboratory. He is presently Manager of Industrial Receiving Tube Applications. Mr. Peterson is a member of Tau Beta Pi, Eta Kappa Nu, and a Senior Member of the Institute of Radio Engineers.





PAUL RAPPAPORT studied chemistry at Temple University, Philadelphia, Pa. before entering the U. S. Navy as an electronic technician in 1944. As a civilian in 1946 he worked nine months at the Naval Air Experimental Station in Philadelphia in the capacity of Physicist. He received the B.S. and M.S. degrees in solid state physics in 1948 and 1949 at Carnegie Institute of Technology where he was a graduate teaching assistant from 1948 to 1949. He joined RCA Laboratories in 1949, where he has worked in the fields of secondary electron emission, direct conversion of radiation into electricity, and radiation damage in semiconductors. He has recently been appointed to a research advisory committee on power plant systems for the National Aeronautics and Space Agency and to a non-propulsive power sources committee for the American Rocket Society. Mr. Rappaport is a member of the American Physical Society, Pi Mu Epsilon, and Sigma Xi.

RICHARD W. SONNENFELDT received the B.S. degree in Electrical Engineering in 1949 at Johns Hopkins University. From 1941-43 and 1946-49 he designed control circuits and systems for the Charles Electric Company of Baltimore. In 1949 he joined RCA, where he was engaged in advanced development work on monochrome and color television receivers. He is now with Advanced Development, Industrial Electronic Products. Mr. Sonnenfeldt is a member of Tau Beta Pi, Omicron Delta Kappa, and a Senior Member of the Institute of Radio Engineers.



FRANK E. VACCARO received the B.S. degree in Electrical Engineering from the University of Tennessee in 1949, and the M.S. degree in Electrical Engineering from Stevens Institute of Technology in 1953. He joined RCA as a Specialized Engineering Trainee in 1950, and was assigned to the Microwave Tube Design activity of the Electron Tube Division in Harrison, New Jersey upon completion of the training program. He worked on the design and testing of magnetrons and traveling-wave tubes from 1951 to 1953, and on the advanced development of wide-range cavity-tunable magnetrons from 1953 to 1956. In 1956 he was made Engineering Leader of the Power Electronics unit of the Microwave Advanced Development activity, working on electrostatically focused traveling-wave tubes (Estiatrons). Since May of this year, he has been Manager of the Microwave Advanced Development activity of the Electron Tube Division located at Princeton. Mr. Vaccaro is a member of Tau Beta Pi, Eta Kappa Nu, and the Institute of Radio Engineers.

PAUL K. WEIMER received the B.A. degree from Manchester College in 1936, the M.A. degree in Physics from the University of Kansas in 1938, and the Ph.D. degree in Physics from Ohio State University in 1942. During 1936 and 1937 he was a graduate assistant in physics at the University of Kansas. From 1937 to 1939, he taught physics and mathematics at Tabor College, Hillsboro, Kansas. Since 1942 he has been engaged in television research at RCA Laboratories Division at Princeton, N. J. During the academic year 1959/1960, he is studying at the University of Paris under an RCA Laboratories Fellowship. Dr. Weimer is a Fellow of the Institute of Radio Engineers, and a Member of the American Physical Society and Sigma Xi.





